Conduction-radiation coupling at the nanoscale

Marta Reina

université
PARIS-SACLAY

Conduction-radiation coupling at the nanoscale

Couplage conduction-rayonnement à nano-échelle

Thèse de doctorat de l'Université Paris-Saclay

École doctorale n° 575, Electrical, Optical, Bio: Physics and Engineering (EOBE)
Spécialité de doctorat: Physique
Unité de recherche: Université Paris-Saclay, Institut d'Optique Graduate School, CNRS, Laboratoire Charles Fabry, 91127, Palaiseau, France.
Référent: : Institut d'Optique

Thèse présentée et soutenue à Paris-Saclay, le 12 octobre 2021, par

Marta REÌNA

Composition du jury

Olivier Bourgeois Directeur de Rercherche CNRS, Institut Néel (CNRS-Université Grenoble Alpes)	Rapporteur
Karl Joulain Professeur des Universités, ENSIP, Université de Poitiers	Rapporteur
Yann Chalopin Chargé de Recherche CNRS, EM2C, CentraleSupelec, Université Paris Saclay	Examinateur
Samy Merabia Directeur de Recherche CNRS, ILM,Université Claude Bernard Lyon I	Président du jury

Direction de la thèse

Philippe Ben-Abdallah Directeur de Rercherche CNRS, Laboratoire Charles Fabry (Institut d'Optique, Université Paris-Saclay)	Directeur de thèse
Riccardo Messina Chargé de Rercherche CNRS, Laboratoire Charles Fabry (Institut d'Optique, Université Paris-Saclay)	Co-encadrant

Thèse de doctorat

NNT: 2021UPAST098

Deus sive natura.

Index

Acknowledgements

Palaiseau, October 21st, 2021

I would like to start this thesis by thanking all the people that in many different ways helped me to achieve this goal.

I wish, first of all, to thank my supervisors, Philippe and Riccardo. They offered me, in spite of the problems arising from the pandemic emergency, a constant support, stimulating at the same time the development of my own research skills.

I want to thank all the people at LCF, Léo, Anton, Ilan, Cheng, Meiping, Anne, Élise, Aurélian, BenJ and Jean-Jacques, with whom I shared many lunches, coffees and nice moments. A special mention goes to Hector, who helped me to solve my administrative problems, to learn French and to laugh in each day we spent together. I know now he loves corgis too, even if he is not ready to admit that.

I want to thank my friends in Paris, or maybe I should say "my family in Paris". Me, Valerio, Nadia, Margherita and Federico shared everything during these years, from happiness to tears.
A special space must be reserved to my old and new friends in Italy, Antonello, Elidian, Ruggero, Giorgia, Giulia, Gaia, Eleonora, Michelangelo, Stefania, Gabriele, Roberto, Chiara, Irene, Angela and Serafina, who never stopped supporting me and sharing their lives with me, despite the distance and the pandemic.

The largest place should be devoted to my family, especially to my father. I was always in their thoughts and I was always their priority even if life these years was particularly difficult and often bitter. I think it is impossible to let you know through these words how much you all mean to me.

Last but not the least, Valerio, who shared and lived with me each second of this adventure. I can affirm without any doubt that I would not be even close to the finish line without him by my side.

Résumé en français
Couplage conduction-rayonnement à nano-échelle

L'étude du transfert radiatif de chaleur entre deux corps à des températures différentes est un problème très ancien en physique. Il a été d'abord étudié à grande distance de séparation où l'échange d'énergie résulte exclusivement des photons propagatifs et où le transfert est bien décrit au moyen de la loi de Stefan-Boltzmann (indépendante de la distance de séparation entre les corps). Cette loi établit une limite supérieure théorique pour le flux échangé entre deux corps, appelée limite du corps noir et correspond à l'échange de chaleur entre deux absorbeurs parfaits. Dans ce cas, la puissance par unité de surface émise par un corps à température T vaut $\varphi_{BB} = \sigma T^4$ où σ est la constante de Stefan-Boltzmann. Néanmoins, le flux émis par un corps réel est toujours inférieur et vaut $\varphi = \epsilon\sigma T^4$ où ϵ est son émissivité ($\epsilon < 1$). En conséquence, le flux échangé entre deux corps à températures T_1 et T_2 ne peut excéder $\varphi_{1\to2} = \sigma(T_1^4 - T_2^4)$.

En revanche, pour des distances inférieures à la longueur d'onde thermique ($\sim$10 μm à température ambiante), c'est-à-dire en champ proche, la situation change radicalement. Une description mathématique détaillée reliant le rayonnement thermique aux fluctuations aléatoires des courants à l'intérieur d'un corps a été faite dans les années 70 par Polder et van Hove (PvH) [1]. Cette description est basée sur la théorie de Rytov de l'électrodynamique fluctuationnelle [2] et a conduit à la prédiction d'une augmentation spectaculaire du flux radiatif de chaleur en champ proche bien au delà de la limite de Stefan-Boltzmann. À ces distances de séparation un nouveau canal participe au transfert de chaleur. Ce canal est associé aux photons non propagatifs qui peuvent transférer de l'énergie par effet tunnel à travers le gap de séparation. Ces photons évanescents deviennent les principaux acteurs du transfert de chaleur à distances sub-longueur d'onde et le flux de chaleur peut dépasser le flux observé en régime de champ lointain de plusieurs ordres de grandeur [3]. Ceci est particulièrement vrai entre des matériaux supportant des modes résonants de surface dans l'infrarouge, tels que les phonons-polaritons que l'on observe à la surface des matériaux polaires ou encore entre des matériaux anisotropes supportant un continuum de modes hyperboliques [4]. Lorsque la distance

d entre deux solides (diélectriques polaires) diminue, le flux de chaleur échangé diverge comme d^{-2} [3]. Les prédictions théoriques de l'électrodynamique fluctuationnelle ont été confirmées expérimentalement jusqu'à des distances de séparation de quelques nanomètres [5–38].

De nombreuses applications ont exploité l'augmentation du flux de chaleur en champ proche. La première est sans doute la conversion d'énergie thermophotovoltaïque de champ proche [6, 30] qui permet de convertir une partie importante de l'énergie électromagnétique confinée au voisinage de corps chauds. Une seconde application importante est la gestion thermique à nanoéchelle [39–43]. Enfin le traitement de l'information à l'aide de flux de chaleur échangés en champ proche est une application qui a vu récemment le jour. Dans cette perspective, de nombreux systèmes ont été proposés, tels que des mémoires thermiques [44, 45], des portes logiques [46], et des diodes thermiques [44, 47]. Certains ont d'ores et déjà été fabriqués et caractérisés expérimentalement [31, 48]. Ces travaux pionniers ont ouvert la voie à une nouvelle technologie baptisée *thermotronique* [42] par analogie directe avec l'électronique.

Un aspect fondamental qui a été peu étudié jusqu'à présent est le couplage entre le transfert de chaleur conductif et radiatif à échelle nanométrique et sub-nanométrique. C'est précisement l'objet d'une partie de ce travail de thèse. Jusqu'à présent dans presque tous les travaux théoriques sur les échanges radiatifs, la température à l'intérieur des solides en interaction était supposée uniforme. Alors que dans la plupart des situations cette hypothèse est réaliste, elle devient discutable en régime de champ proche extrême, aux distances de séparation où la transition vers la conduction a lieu. Dans cette thèse, nous nous interrogeons précisément sur la validité de cette hypothèse et analysons ainsi les limites de la théorie PvH [49]. Outre ce problème, nous étudions ici le comportement thermomécanique d'un oscillateur couplé en champ proche avec un substrat et nous montrons le potentiel de ce type de système pour le traitement de l'information ou la conception de mémoires thermiques.

Oscillateur thermomécanique bistable

Dans la première partie de ce travail de thèse nous avons étudié la dynamique d'un oscillateur thermomécanique bilame composé de matériaux à transition de phase et démontré son comportement thermomécanique multistable et son potentiel pour le traitement de l'information [50]. Le système étudié (Fig. 1) est composé d'un bilame dont la couche supérieure est en VO_2 et la couche inférieure en verre. Le bilame échange sur une partie de sa surface inférieure de la chaleur en champ proche avec un substrat en verre et il est libre de rayonner en champ lointain avec le milieu environnant (bain thermique). Le long du bilame les flux radiatif et conductif sont couplés par l'intermédiaire des propriétés physiques des matériaux. La variation locale du coefficient de dilatation thermique avec le champ de température induit localement une contrainte mécanique dans le bilame qui conduit à sa déflexion. Il en résulte une modification du flux de

chaleur qu'il échange avec son environnement. Dans ce travail nous avons analysé en détail le comportement dynamique de ce système thermomécanique.

Nous avons tout d'abord mis en évidence la présence de deux profils d'équilibre à la fois pour le déplacement et la température le long du bilame (Fig. 2), démontrant ainsi la bistabilité de l'oscillateur thermomécanique. En étudiant les conditions d'existence de cette bistabilité en fonction des différents paramètres géométriques, nous avons identifié les paramètres optimaux pour observer des solutions d'équilibre significativement différentes. Nous avons finalement exploité ce comportement particulier pour concevoir une mémoire thermique et une porte logique de type NOT.

Nous avons également mis en évidence le comportement hystérétique du système (Fig. 3). Ainsi nous avons montré qu'en modulant en fonction du temps la température T_s du substrat la température du système suit différentes trajectoires, comme l'illustre le portrait de phase représenté sur la Fig. 3(a). En particulier, nous avons montré que selon la rapidité de modulation de la tempéraure T_s, le système peut ou non passer d'un état d'équilibre à l'autre (voir Fig. 3). En définissant des états "0" et "1" à partir de valeurs seuils de la température de l'extrémité libre du bilame, nous avons montré que ce comportement peut être exploité pour concevoir des mémoires thermiques et des portes logiques élémentaires à une entrée.

Bien que préliminaire, ce travail ouvre la voie à l'étude plus générale du comportement thermomécanique d'oscillateurs couplés pilotés par des interactions en champ proche. De nombreux problèmes restent à explorer. Tout d'abord, la préparation thermique des oscillateurs, qui joue un rôle fondamental dans l'évolution dynamique du système, devrait être étudiée plus en détail. De plus, l'étude du couplage d'au moins deux oscillateurs devrait permettre de concevoir des portes logiques à deux entrées et

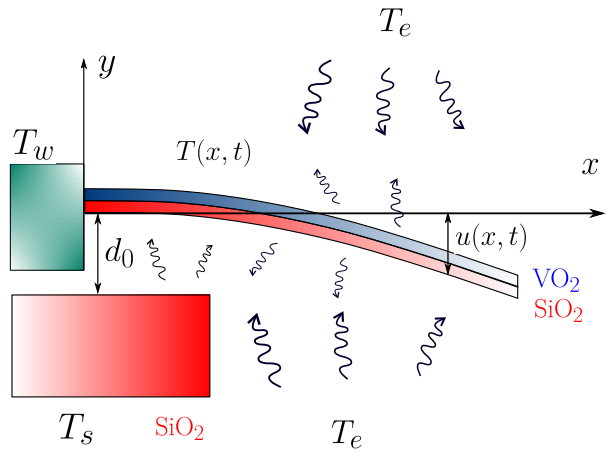

Figure 1: Représentation schématique d'un oscillateur termomécanique bilame composé d'une couche de silice et d'une couche de matériau à transition de phase (VO_2). Le bilame est encastré à gauche dans un mur à température T_w, alors que son extrémité de droite est laissée libre d'osciller. Il échange de la chaleur en champ lointain avec l'environnement à température T_e et en champ proche avec un substrat à température T_s. Son déplacement vertical le long de l'axe x est représenté par $u(x,t)$, et son profil de température par $T(x,t)$.

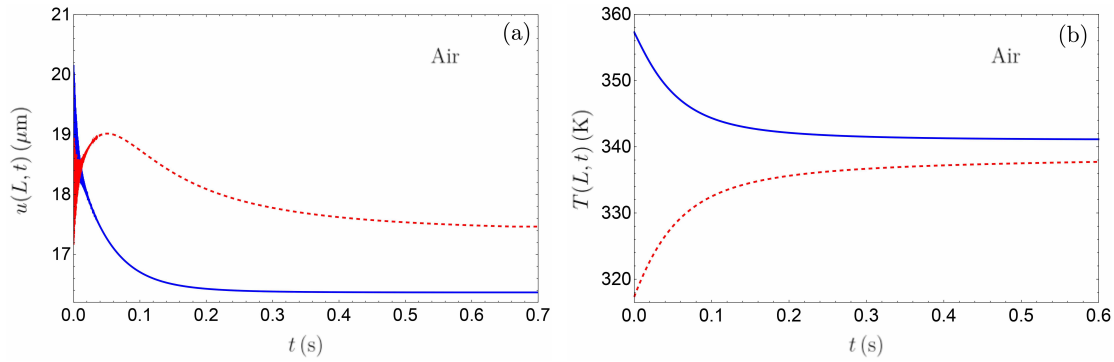

Figure 2: Évolution du déplacement **(a)** et de la température **(b)** en function du temps de l'extrémité libre de la poutre placée dans le vide ou dans l'air. La courbe rouge pointillée et la courbe bleue pleine représentent les solutions à partir de deux profils différents à l'instant $t = 0$.

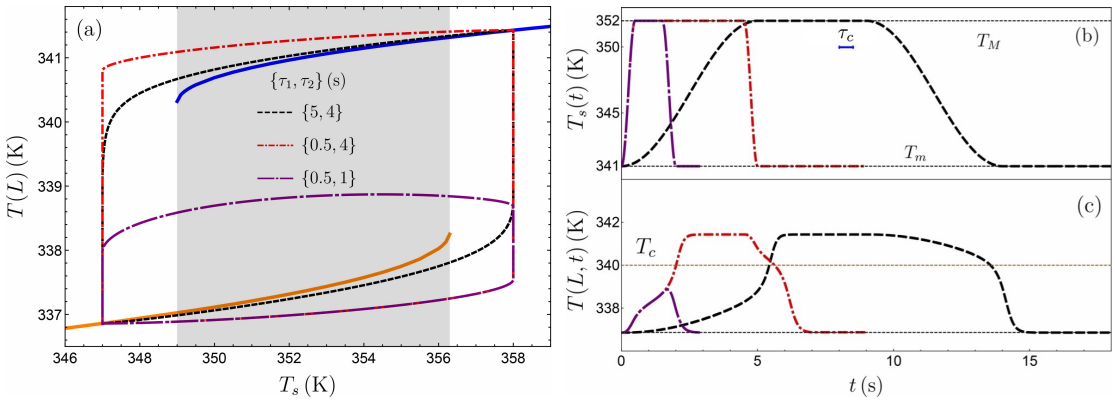

Figure 3: **(a)** Portrait de phase de la température $T(L,t)$ de l'extrémité libre de la poutre en fonction de la température du substrat $T_s(t)$. Les trois courbes correspondent aux différents profils de $T_s(t)$. Les courbes bleue et orange correspondent aux solutions stationnaires pour $T(L)$ associées à chaque valeur de T_s. **(b)** Évolution temporelle imposée pour la température du substrat T_s. L'intervalle en bleu indique la durée du temps de décroissance τ_c. **(c)** Évolution temporelle de $T(L)$ en fonction du temps [même convention qu'en **(a)**]. La courbe pointillée horizontale en marron représente la température critique T_c du VO_2.

également d'envisager un traitement plus élaboré de l'information.

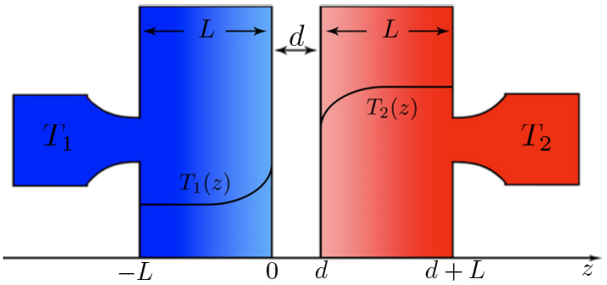

Figure 4: Schéma du système étudié. Deux films solides d'épaisseur L sont en contact sur leur surface extérieure avec un thermostat et sont libre d'échanger de la chaleur au niveau de leur surface interne à travers un gap (vide) d'épaisseur d. À l'intérieur des films la chaleur se propage par conduction et un profil de température généralement variable s'établit.

Couplage conduction-rayonnement entre deux solides en champ proche

Dans la deuxième partie de la thèse nous nous sommes intéréssés à un problème plus fondamental, celui de la validité de la théorie standard de Polder et Van Hove (PvH) pour décrire les échanges radiatifs entre les solides en régime de champ proche extrême, c'est-à-dire dans la zone de transition entre le regime radiatif et le régime conductif. Dans la théorie de PvH la température au sein des solides en interaction est supposée uniforme. Autrement dit les solides sont supposés parfaitement conducteurs. Nous avons ici relaxé cette contrainte et décrit l'évolution des profils de température à travers le mécanisme de couplage entre la conduction et le transfert de chaleur à travers le gap de séparation. Nous avons étudié le transfert entre deux films solides séparés par un gap (vide) de l'ordre du nanomètre d'épaisseur (Fig. 4) proche du contact entre les solides [51].

Dans la théorie que nous avons introduite dans ce travail, le transport de chaleur au sein de chaque solide est décrit à l'aide de l'équation de transport de Boltzmann (BTE) pour les phonons, de sorte que tous les régimes de transport, du régime balistique

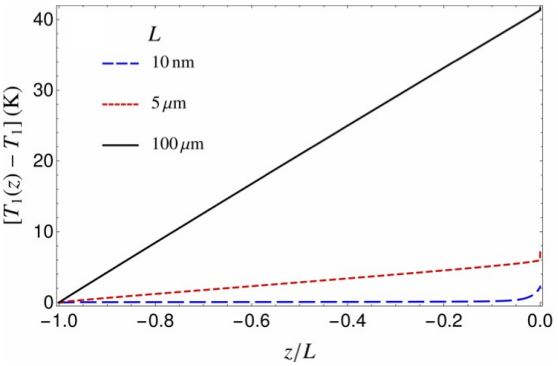

Figure 5: Profil de température en régime stationnaire dans un film de SiC en interaction avec un autre film de SiC de même épaisseur à travers un gap (vide) de 1 nm. Les profils correspondent au champ de température dans le film de gauche en contact avec un thermostat à température $T_1 = 300\,\mathrm{K}$, le film de droite étant en contact avec un thermostat à $T_2 = 400\,\mathrm{K}$.

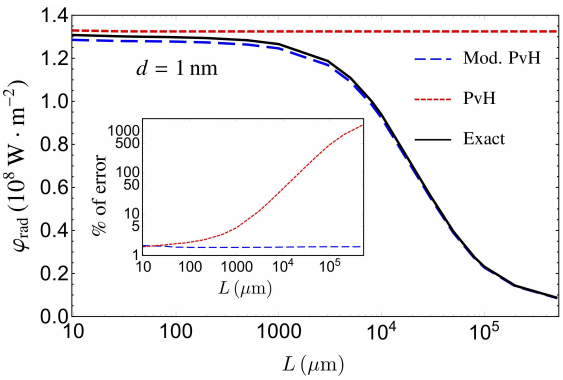

Figure 6: Flux de chaleur radiatif entre deux couches de SiC en fonction de leur épaisseur lorsque la distance de séparation vaut $d = 1\,\text{nm}$. Nous montrons ici le résultat exact (courbe noire), la prédiction de PvH (courbe rouge pointillée) et le PvH modifié (courbe bleue pointillée, obtenue à l'aide des température d'équilibre à l'interface entre les deux solides). Inset: valeur absolue de l'erreur par rapport aux approches PvH et PvH modifié. Les températures des thermostats sont $T_L = 300\,\text{K}$ et $T_R = 400\,\text{K}$.

(solides plus petits que le libre parcours moyen des phonons) au régime diffusif (solides épais par rapport au libre parcours moyen des phonons), peuvent être pris en compte dans le mécanisme de couplage conduction-rayonnement.

En calculant les profils de température (Fig. 5) au sein de chaque corps et les flux radiatifs échangés correspondant entre les deux dans le régime de champ proche extrême, nous avons pu établir qu'une variation locale de température peut exister au sein de films polaires en régime quasi-diffusif ou diffusif, autrement dit lorsque les films sont suffisamment épais. En revanche aucune déviation par rapport aux prédictions de la théorie de PvH n'est perceptible dans les films minces où le régime de transport des phonons tend vers le régime ballistique.

Nous avons montré que l'erreur relative entre le flux de chaleur calculé à l'aide de la théorie PvH et le flux exact peut atteindre des valeurs de l'ordre de 1000% dans le cas de couches de matériaux polaires de 500 μm à 1 nm de distance (Fig. 6). Nous avons également démontré que le transfert de chaleur en champ proche entre deux solides est essentiellement un phénomène surfacique. Ce résultat devrait permettre une description simplifiée des échanges de chaleur en champ proche.

L'étude expérimentale du couplage entre la conduction et le rayonnement de champ proche est à l'évidence une étape nécessaire. Néanmoins elle nécessite d'étendre nos travaux théoriques préliminaires à des géométries plus complexes et plus conformes aux dispositifs expérimentaux actuels. En particulier l'étude du couplage dans une configuration sphère-plan permettrait de prendre en compte ce mécanisme dans l'interprétations des résultats expérimentaux des dispositifs basés sur l'utilisation de sondes microscopiques. Une réinterprétation de certains résultats expérimentaux actuels pourrait également être faite pour prendre en compte le couplage conduction-rayonnement. Enfin, le rôle joué par la réponse optique non-locale des matériaux sur le mécanisme de couplage devra aussi être exploré.

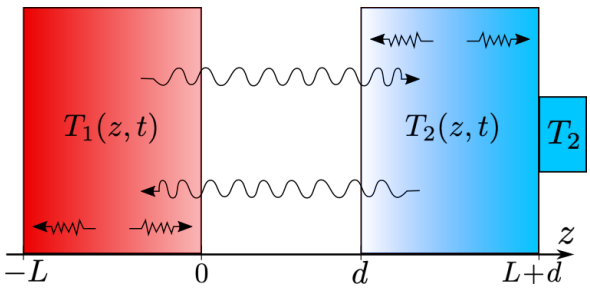

Figure 7: Schéma du système utilisé pour l'étude de la relaxation thermique. Le film de droite (froid) est en contact avec un thermostat à température T_2 tandis que le film de gauche (chaud) n'est pas thermostaté. Les deux films relaxent vers la température du réservoir en échangeant de la chaleur par rayonnement de champ proche ou par tunneling d'électron à travers un gap (vide) d'épaisseur nano ou sub-nanométrique.

Dynamique de relaxation en présence de couplage conduction-rayonnement

Enfin, nous avons étudié le problème de l'évolution dynamique (relaxation thermique) d'un système de deux films couplés à travers un gap d'épaisseur nano ou sub-nanométrique. La configuration géométrique étudiée est illustrée sur la Fig. 7. Tout d'abord, nous avons considéré le cas des matériaux polaires (SiC et SiO_2), séparées par un intervalle de vide de l'ordre du nanomètre. À cette distance les deux films relaxent vers l'état d'équilibre à travers le flux de champ proche. Dans un second temps nous avons étudié la relaxation thermique de films métalliques (Au) séparés par un gap d'épaisseur sub-nanométrique. A cette distance de séparation c'est le transfert de chaleur par tunneling d'électron qui domine devant le transfert radiatif [52].

La comparaison de nos résultats numériques avec les prédictions issues de la théorie de PvH ont permis de mettre en évidence un fort ralentissement de la relaxation qui est directement imputable au couplage entre la conduction et le transfert de chaleur à

Figure 8: Comparaison entre l'évolution temporelle de la température moyenne dans la couche de gauche et celle en présence d'un échange purement radiatif dans le cas de deux matériaux polaires en interaction (PvH). La courbe noire (rouge) représente le cas du SiO_2 (SiC) avec couplage, la courbe noire (rouge) pointillée les prédictions issues de la théorie PvH. Les paramètres sont $T_2 = 300\,\mathrm{K}$, $\Delta T = 100\,\mathrm{K}$ et $d = 1\,\mathrm{nm}$.

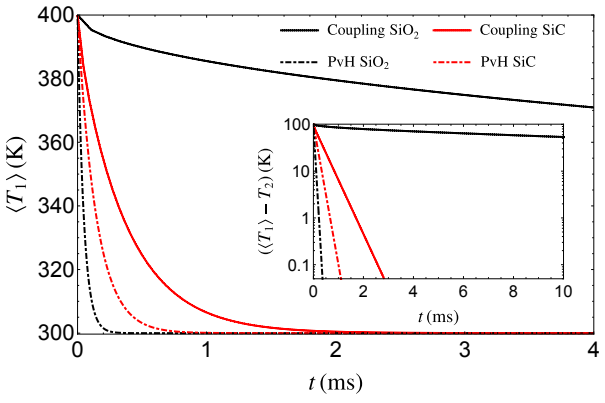

travers le gap de séparation entre les deux solides (Fig. 8). Le temps de relaxation associé atteint des valeurs jusqu'à trois ordres de grandeur plus grandes par rapport à son homologue sans couplage. Nous avons montré que pour que ce ralentissement soit significatif il est nécessaire que la conductance d'échange à travers le gap soit au moins comparable à la conductance d'échange par conduction à travers le film.

Une étape supplémentaire dans l'étude du couplage conduction-rayonnement pourrait être d'étendre cette analyse au cas des matériaux dans lesquels la réponse optique locale des matériaux n'est plus satisfaite, et d'étudier comment les effets non locaux affectent le processus de refroidissement. Enfin, un traitement ab-initio complet des échanges thermiques pourrait être utilisé pour prendre en compte tous les mécanismes de couplage à l'échelle nanométrique et subnanométrique, notamment le tunneling des phonons acoustiques entre des matériaux polaires ou des semiconducteurs.

Introduction

The study of radiative heat transfer between two bodies at different temperatures is a very old problem in physics. It has been firstly faced at long separation distance, where energy exchange results exclusively from propagative photons and it is well described by means of the Stefan-Boltzmann law (independent from the distance between the bodies). This law stipulated a theoretical upper limit for the flux exchanged between two bodies known as blackbody limit. This limit can be reached only in the purely theoretical case of an ideal surface that absorbs all incident heat radiation. In this limiting case, the power per unit surface emitted by the body at temperature T corresponds to $\varphi_{BB} = \sigma T^4$ where σ is the Stefan-Boltzmann constant. Nevertheless, the flux emitted by a real body is always smaller and reads $\varphi = \epsilon\sigma T^4$ where ϵ is its emissivity ($\epsilon < 1$). As a consequence also the flux exchange between two bodies at temperatures T_1 and T_2 has an upper limit given by $\varphi_{1\to2} = \sigma(T_1^4 - T_2^4)$.

On the other hand, at distances smaller than the thermal wavelength ($\sim$10 μm at ambient temperature), i.e. in the near-field regime, the situation radically changes. A detailed mathematical description relating thermal radiation to the random fluctuations of charges inside the body was carried out in the 70's with the work of Polder and van Hove (PvH) [1], based on Rytov's theory of fluctuational electrodynamics [2]. This led to the prediction of a dramatic enhancement of radiative heat flux in the near field with respect to the Stefan-Boltzmann limit. Indeed, the near-field heat exchange can overcome the blackbody theoretical limit by several orders of magnitude since at this scale a new channel participates to the heat transfer. This channel is associated with non-propagative photons which can transfer energy by tunneling through the vacuum gap. These evanescent photons become the main contributors to the heat transfer at subwavelength distances and the heat flux can become significantly larger than the flux observed in far-field regime [3]. This is particularly true between materials supporting resonant surface modes in the infrared, such as phonon-polaritons for polar materials (i.e. modes due to the coupling between partial-charges oscillations and the electromagnetic field) or between anisotropic materials supporting a continuum of hyperbolic modes [4]. Upon reducing the gap size d the heat flux exchanged between polar dielectrics diverges as d^{-2} [3]. The theoretical prediction of the fluctuational electrodynamics have been confirmed experimentally down to the nanometer range of distances [5–38].

Many applications exploited the near-field enhancement of heat flux. The first one is the near-field thermophotovoltaic energy conversion [6,30]. Another is the manipulation of heat flux at nanoscale in the field of thermal management [39–43] and to process information through thermally-driven devices, using then photons instead of phonons as carriers to overcome the inherent problems associated with the relatively small propagation speed of acoustic phonons. To this aim, many systems exploiting the features of radiative heat transfer in the near-field regime have been proposed, such as thermal memories [44,45], logic gates [46], and thermal diodes [44,47] also recently experimentally realized [31,48]. These pioneer works paved the way to a technology also called *thermotronics* [42]. In the design of all the mentioned devices a key role is played by the presence of phase-change materials having strong thermal-dependent optical properties around critical temperatures. So far, the study of near-field heat transfer in two- and many-body systems has been limited to purely radiative exchanges.

A fundamental aspect which has been scarcely investigated is the coupling between conductive and radiative heat transfer at nanoscale. In fact, in almost all theoretical works on radiative heat transfer, the temperature within each interacting body is assumed uniform. While in most situations this assumption is realistic, it becomes questionable in extreme near-field regime at separation distances where the transition to the conduction takes places. In this thesis we question in particular the validity of this assumption and therefore wonder about the limitations of the PvH theory [49]. The coupling between conduction and radiation is the main topic of this thesis. In particular, the work described in this manuscript concerns different scenarios in which this coupling could be relevant, both from a fundamental and an applicative point of view. More specifically, we first investigate a themomechanical system driven by near-field heat exchanges which could be exploited for the design of innovative information-processing devices or for the conception of thermal memories. In the next part of this work we focus on the more fundamental problem of the near-field heat exchange between two planar slabs close to the contact (extreme near-field regime) and show that some deviation with respect to predictions of the classical theory could be relevant to interpret some experimental results.

In Chap. 1 we introduce the theoretical framework needed to describe the radiative heat exchange between two bodies. We remind the existence conditions for an interface to support resonant surface-waves and we describe the main features of radiative heat transfer between two slabs for polar materials, metals and phase-change materials.

In Chap. 2 we study the thermomechanical behavior of a phase-change bimaterial cantilever driven by near-field heat exchanges in order to exploit its features to make thermal information treatment. We first show that these systems can be bistable, i.e. they admit two equilibrium solutions. In this case we consider the problem of the coupling between the conduction within the beam, the near-field radiative heat exchange between the substrate and the cantilever and finally its mechanical oscillation due to the mismatch

between the thermal expansion coefficients of the two layers. We find out that at least two equilibrium profiles both for the displacement and the temperature of the beam exist and we finally exploit this behavior to create a thermal hysteresis and then to design a thermal memory and a thermal NOT logic gate.

In Chap. 3 we question the validity of the standard Polder and Van Hove theory in extreme near-field regime. To this aim, we release the usual assumption of perfectly conducting solid and we model the realistic conduction-radiation coupling in the particular case of polar materials. Our goal is to quantify the deviation between the predictions from the standard PvH theory and our approach which takes into account the conduction radiation coupling. In our model the heat transport within the solid is described by means of the Boltzmann Transport Equation (BTE) for phonons so that all regimes of conduction can be taken into account from the ballistic to the diffusive one. The conduction-radiation coupling is accounted for in the energy-balance equation, where radiative power is locally dissipated through each solid. Studying the temperature profiles within each slab and the corresponding radiative heat flux between the two in extreme near-field regime we show that a non uniform temperature profile within the slabs can appear in the quasi-diffusive or diffusive heat-transport regime, implying a strong difference between the heat flux calculated through the PvH theory and the one obtained through our new theoretical framework.

In Chap. 4 we face the problem of the dynamical evolution (thermal relaxation) of two slabs close to the contact when one of these slabs is in contact with a thermostat. We successfully investigate the relaxation of polar slabs at nanometric distances and the relaxation of metals at subnanometric distances. In the first case, the heat transfer through the gap is mediated by photon tunneling, as investigated in Chap. 3, while in the second case it is due to electron tunneling. By comparing our results in the presence of coupling to the ones obtained through the simplified theoretical framework ignoring conduction we demonstrate that the coupling leads to a strong slowdown in the temporal evolution of the temperature profiles, the relaxation time reaching values several orders of magnitude larger than in the scenario without coupling. We conclude this manuscript by summarizing the main results and by giving some prospects for future research.

Chapter 1

Fluctuational electrodynamics and radiative heat transfer between two solids

Thermal radiation can be associated with any object at non-zero absolute temperature. An electromagnetic radiative emission occurs in its surrounding due to the thermally-driven random motions of electric charges inside the body. Efforts to understand this phenomenon and the associated heat exchange between two macroscopic bodies at large separation distance (far-field regime) culminated with the pioneer work of Max Planck about the blackbody radiation at the beginning of the 20th century. Further steps to understand the radiative heat transfer in the Near-Field regime (i.e. that is for separation distances smaller that the thermal wavelength $\lambda_{\text{th}} = \hbar c/k_B T$) were done with quantum-mechanical derivation of the Fluctuation-Dissipation Theorem (FDT) and, more importantly, with Rytov's fluctuational electrodynamics theory introduced in 1953. This approach allowed for the first time a detailed mathematical description relating thermal radiation to its microscopic origin, i.e. the random fluctuations of charges inside the body. At this scale, the contribution of evanescent waves to the heat transfer becomes dominant compared to the one of the propagative waves. An important step forward was done in 1971 by Polder and van Hove to describe heat transfer at subwavelength distance between two planar solids. Their approach was based on Rytov's work, but the idea of Polder and van Hove was to use the FDT to relate fluctuating currents, random source in the Maxwell equations, to the temperature.

In the last years, many works have been carried out, showing important deviations from the blackbody law, in particular when considering materials supporting resonant surface waves. More specifically, the possibility to get superplanckian heat exchanges, i.e. exchanges which can go beyond the blackbody limit, has been demonstrated with polar materials in interaction. Very recently, it has been predicted that a continuum of evanescent modes such as hyperbolic modes is also sufficient to observe a superplanck-

ian transfer.

In this chapter we introduce the main theoretical concepts that will be used in this thesis to investigate the different systems consider in this work.

1.1 Poynting vector

We consider a non-magnetic body at $T > 0$ K, with permittivity $\epsilon(\omega)$. As anticipated in the introduction, because of thermal fluctuations, the charges inside the body fluctuate giving rise to electric currents [2]. The statistical average of these fluctuating currents is zero, i.e. $\langle \mathbf{j} \rangle = 0$, but the their correlations are not zero. The Poynting vector $\mathbf{\Pi}(\mathbf{r}, \omega)$, which is a quadratic quantity, is then not zero either. The general expression of it in terms of the electric $\mathbf{E}(\mathbf{r}, \omega)$ and magnetic $\mathbf{H}(\mathbf{r}, \omega)$ fields is the following

$$\mathbf{\Pi}(\mathbf{r}, \omega) = \mathbf{E}(\mathbf{r}, \omega) \times \mathbf{H}(\mathbf{r}, \omega), \tag{1.1}$$

in which with $\mathbf{r}$ we denote the position vector and with ω the angular frequency. In order to write the explicit dependence of the ensemble average of the Poynting vector on the fluctuating currents, we write the well-known expressions of the electric and magnetic fields in terms of the Green's tensors

$$\mathbf{E}(\mathbf{r}, \omega) = i\mu_0\omega \int_V d^3\mathbf{r}' \vec{G}^{EE}(\mathbf{r}, r', \omega)\mathbf{j}(\mathbf{r}', \omega), \tag{1.2}$$

$$\mathbf{H}(\mathbf{r}, \omega) = \int_V d^3\mathbf{r}' \vec{G}^{HE}(\mathbf{r}, r', \omega)\mathbf{j}(\mathbf{r}', \omega), \tag{1.3}$$

where i is the imaginary unit and we denote with V the volume of the body, with μ_0 the vacuum permeability, and where G^{EE} and G^{HE} denote the electric and magnetic Green's tensors. Due to the linearity of Maxwell's equations the response to any local excitation for a given geometric configuration is given by the Green's tensors. When an ensemble average is taken on the Poynting vector, it is easy to see that an ensemble average is taken on the spatial correlation function of the thermal current fluctuations, as we can show using expressions (1.1) and (1.2)-(1.3) that the Poynting vector depends on the random current correlation function, i.e.

$$\langle \mathbf{\Pi}(\mathbf{r}, \omega) \rangle \propto \langle \mathbf{j}(\mathbf{r}, \omega)\mathbf{j}^*(\mathbf{r}', \omega') \rangle. \tag{1.4}$$

in which the symbol * indicates the complex conjugate.

The correlations of the fluctuating currents can be obtained through the Fluctuation-Dissipation Theorem, linking the correlation between random temperature-driven electrical currents to the temperature and the dielectric properties of the medium. In order to use the FDT to obtain the statistical properties of the fluctuating currents, we start

supposing that the dielectric constant $\epsilon(\omega)$ is a local quantity, and we also suppose that the material is in Local Thermodynamic Equilibrium, which means that an equilibrium temperature T can be defined at each moment and for each point of the system. By considering two currents inside the body $\mathbf{j}(\mathbf{r},\omega)$ and $\mathbf{j}(\mathbf{r}',\omega')$ at the points $\mathbf{r}$ and $\mathbf{r}'$, with angular frequency ω and ω', we obtain, using the FDT, the following expression

$$\langle j_k(\mathbf{r},\omega) j_l^*(\mathbf{r}',\omega')\rangle = 2\frac{\omega\epsilon_0}{\pi}\mathrm{Im}[\epsilon(\omega)]\Theta(\omega,T)\delta_{kl}\delta(\mathbf{r}-\mathbf{r}')\delta(\omega-\omega'), \tag{1.5}$$

where $k,l = x,y,z$ represent the different components in Cartesian coordinates, $\hbar$ is the reduced Planck's constant, k_B is the Boltzmann's constant, ϵ_0 is the vacuum dielectric constant,

$$\Theta(\omega,T) = \frac{\hbar\omega}{\exp(\hbar\omega/k_BT)-1}, \tag{1.6}$$

is the average energy of a harmonic oscillator, δ_{kl} is the Kronecker's symbol and δ is the Dirac distribution. The presence of the Dirac distribution $\delta(\mathbf{r}-\mathbf{r}')$ is the consequence of the optical locality, while $\delta(\omega-\omega')$ is the results of the fact that we focus only on stationary processes.

Notice that that the fluctuational-electrodynamics theory is conceptually really similar to the famous Langevin theory to describe the Brownian motion of particles inside a fluid under the colliding events between the particles and the fluid molecules. In the fluctuational-electrodynamics theory the fluctuating currents play analogous role of fluid molecules and Maxwell's equations replace Langevin's equation. This electromagnetic problem that is apparently easy is actually really challenging and can be solved analytically only in some particular situations. In the following we consider this problem of radiative heat transfer in simple geometric configurations which can be partially solved analytically.

1.2 Radiative heat transfer between two planar interfaces

For our scopes, we are going to consider the case of two semi-infinite planar bodies separated by a vacuum gap d. This calculation has been performed for the first time by Polder and van Hove and has become one of the most used geometries for Near-Field Radiative Heat Transfer (NFRHT) [1]. We consider a system in which the space is divided basically in three parts (see Fig.1.1): the first body, characterized by a dielectric constant $\epsilon_1(\omega)$, fills the semi-infinite space $-\infty < z < 0$; the second one, with dielectric constant $\epsilon_2(\omega)$ occupies the part $d < z < +\infty$, whereas, in the middle of the two bodies, i.e. $0 < z < d$ there is a vacuum gap. Moreover, we suppose that the two bodies have uniform non-zero temperatures T_1 and T_2 respectively, implying the local equilibrium temperature in the two materials. Since the two bodies have $T > 0$, they exchange

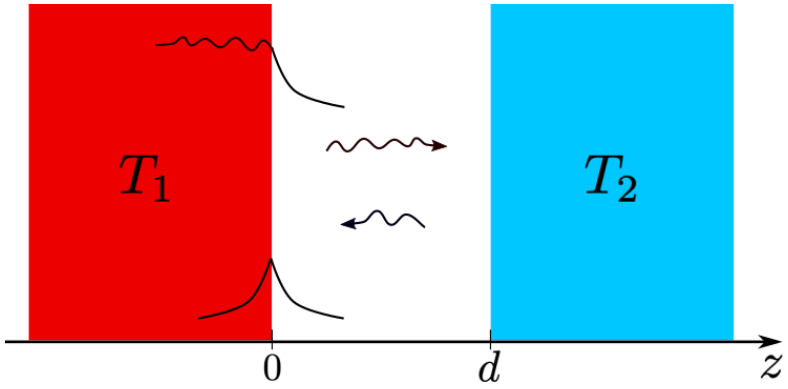

Figure 1.1: Geometry of the system. Two semi-infinite parallel slabs at temperatures $T_1 > T_2$. When $d > \lambda_{\text{th}}$, the thermal wavelength, heat is exchanged with propagating photons (sinusoidal arrows). On the other hand, when $d < \lambda_{\text{th}}$ the transfer is also mediated by evanescent and frustrated photons.

energy radiatively. From now on we label as $\varphi_{i\to j}$ the energy flux from the body i to the body j. The vacuum, of course, does not radiate or absorb any energy. We can then obtain the net flux exchanged between the two bodies as follows [38, 53]

$$\Phi_{1,2} = \varphi_{1\to 2} - \varphi_{2\to 1}. \tag{1.7}$$

Also in this case, the fluctuating currents are the base of the radiative phenomenon. In fact, thanks to these currents, the first body emits an electromagnetic field everywhere in the environment and, in particular, also inside the second body, in which it is absorbed. This energy is the contribution of the first body to the energy exchange between the two. In order to obtain this quantity, we start by evaluation the average value of the Poynting vector. For the case of a planar system, the Green's function are known and they can be easily expressed analytically [54]. The final result for the first body has the following form

$$\begin{aligned}\langle \Pi_z(d^+,\omega)\rangle = \pi L^0_\omega(T_1)\Bigg[&\int_0^{k_0} \frac{K\,dK}{k_0^2}\sum_{\alpha=s,p}\frac{(1-|r^\alpha_{31}|)^2(1-|r^\alpha_{31}|)^2}{|1-r^\alpha_{31}r^\alpha_{32}e^{2ik_z d}|^2}\\ &+\int_{k_0}^{+\infty}\frac{K\,dK}{k_0^2}\sum_{\alpha=s,p}\frac{4\mathrm{Im}(r^\alpha_{31})\mathrm{Im}(r^\alpha_{32})}{|1-r^\alpha_{31}r^\alpha_{32}e^{-2k''_z d}|^2}e^{-2k''_z d}\Bigg],\end{aligned} \tag{1.8}$$

where $L^0_\omega(T_1)$ is the blackbody radiance at temperature T_1 and angular frequency ω, $k_0 = \omega/c$ with c the speed of light, r^α_{ij} are the Fresnel reflection coefficients for the interface between the part i and the part j of the system and $k_z = \sqrt{k_0^2 - K^2}$ is the z-component of the wavevector in vacuum. We can obtain the value of the Poynting vector

$\langle \Pi(0^-, \omega) \rangle$ following the same steps, and getting a similar expression with $L^0_\omega(T_2)$ instead of $L^0_\omega(T_1)$. It follows that he net flux exchanged between the two bodies reads

$$\Phi(T_1, T_2, d) = \int_0^\infty \frac{d\omega}{4\pi^2} [\Theta(\omega, T_1) - \Theta(\omega, T_2)] \int_0^\infty dK\, K \sum_{\alpha=s,p} \mathcal{T}^\alpha(\omega, K, d), \quad (1.9)$$

where $\mathcal{T}^\alpha(\omega, K, d)$ is the transmission probability of an electromagnetic mode (α, ω, K) of polarization α, angular frequency ω and parallel wave vector K and which takes values in the interval $[0, 1]$. Its expression in terms of the Fresnel coefficients is

$$\mathcal{T}^\alpha(\omega, K, d) = \begin{cases} \dfrac{(1 - |r^\alpha_{31}|^2)(1 - |r^\alpha_{32}|^2)}{|D^\alpha|^2}, & \text{if } K < k_0 \\ \dfrac{4\mathrm{Im}(r^\alpha_{31})\mathrm{Im}(r^\alpha_{32}) \exp(-2\mathrm{Im}(k_z)d)}{|D^\alpha|^2}, & \text{if } K > k_0 \end{cases} \quad (1.10)$$

where $k_{z_i} = \sqrt{\epsilon_i(\omega) k_0^2 - K^2}$ is the component of the wave vector perpendicular to the plane in the medium i, $D^\alpha = 1 - r^\alpha_{31} r^\alpha_{32} e^{2ik_z d}$ is the Fabry-Perot denominator and r^α_{ij} are the Fresnel reflection coefficients at the interfaces between the medium i and the medium j for the polarization states $\alpha = (s, p)$, given by

$$r^\alpha_{ij}(\omega, k) = \begin{cases} \dfrac{k_{z_i} - k_{z_j}}{k_{z_i} + k_{z_j}}, & \alpha = s \\ \dfrac{\epsilon_j k_{z_i} - \epsilon_i k_{z_j}}{\epsilon_j k_{z_i} + \epsilon_i k_{z_j}} & \alpha = p \end{cases}. \quad (1.11)$$

Basically, in Eq.(1.9) we expressed the radiative heat flux as a sum of the energy carried by all modes of the electromagnetic field, in the Planck windows defined by the difference between the average energies of the Planck harmonic oscillator with the temperature of the two bodies T_1 and T_2 and multiplied by the energy transmission coefficient $\mathcal{T}^\alpha$ which depends on the optical proprieties of the two bodies. This expression has a strong correspondence with the Landauer-Büttiker formula used in solid-state physics for the electron transport in mesoscopic systems. In the last years, it has become a standard way to describe the radiative heat transfer [38, 55–57].

It is really important to notice that from the expression of the transmission coefficients in Eq.(1.10) two contributions immediately emerge. The first one, given by the K-integration in the interval $[0, k_0]$, is due to propagative waves, while the second one is the contribution of evanescent waves. The difference between these two types of waves is based on the way they propagate from the substrate across the vacuum gap. In fact, when $K < k_0$ waves are propagative, which means that they propagate in vacuum without attenuation. On the other hand, when $K > k_0$ waves are evanescent which means

they decrease exponentially through the gap. Mathematically, this behavior can be easily demonstrated from the expression of the perpendicular component of wavevector in vacuum $k_z = \sqrt{k_0^2 - K^2}$, since for $K > k_0$, k_z is a pure imaginary number so that the exponential factor $e^{2ik_z d}$ becomes $e^{-2k_z'' d}$. A detailed study of the transmission coefficient shows that it is negligible for the evanescent waves ($K > k_0$) when d is larger than the thermal wavelength, and it is always between 0 and 1. Moreover, when the slab support surface waves the value of the transmission coefficient is almost negligible everywhere except for these resonant modes where it is close to 1, as we will show in Sec. 1.2. As we are going to show in the following, at distances much larger than the thermal wavelength λ_{th}, the classical radiative heat-transfer laws can be recovered. Moreover, as we will see at smaller distance, due to the contribution of evanescent waves that can be dominant with respect to the propagative waves, the radiative heat flux can overcome the blackbody limit by several orders of magnitude. Generally speaking, even if the expression (1.9) describes the simple case of two semi-infinite parallel planes it can be easily extended to the case of finite or even multilayer slabs by replacing the Fresnel coefficient r_{ij}^{α} with R_i^{α}, which is the full reflection coefficient of the system.

Radiative thermal conductance

In order to study the radiative heat transfer between two solids, it is convenient to introduce a quantity known as the linear thermal conductance, which is a heat current per unit temperature difference. Its definition in terms of the zero limit of the temperature difference ΔT between the two bodies is [38]

$$\begin{aligned} h^R(T,d) &= \lim_{\Delta T \to 0} \left| \frac{\Phi(T+\Delta T, T, d)}{\Delta T} \right| = \\ &= \int_0^\infty \frac{d\omega}{4\pi^2} \frac{\partial \Theta(\omega, T)}{\partial T} \int_0^\infty dK\, K \sum_{\alpha=s,p} \mathcal{T}^{\alpha}(\omega, K, d) \equiv \int_0^\infty d\omega\, h_\omega^R(T,d), \end{aligned} \tag{1.12}$$

where we have also introduced the spectral heat transfer coefficient h_ω^R. In this way, we can calculate the net energy heat flux $\Delta\Phi$ per unit surface exchanged by the two bodies, separated by a distance d, as follows

$$\Delta\Phi = h^R(T,d)\Delta T. \tag{1.13}$$

Also the spectral heat transfer coefficient can be separated in two different contributions for the propagative and evanescent waves

$$h_\omega^{R,\text{prop}}(d,T) = h_\omega^0(T) \int_0^{k_0} \frac{K\, dK}{k_0^2} \sum_{\alpha=s,p} \mathcal{T}^{\alpha}(\omega, K, d), \tag{1.14}$$

$$h_{\omega}^{R,\text{evan}}(d,T) = h_{\omega}^{0}(T)\int_{k_0}^{+\infty}\frac{K\,dK}{k_0^2}\sum_{\alpha=s,p}\mathcal{T}^{\alpha}(\omega,K,d), \tag{1.15}$$

where $h_{\omega}^{0}(T) \equiv \pi\partial L_{\omega}^{0}/\partial T$. It has been shown that the heat transfer can be almost monochromatic around the resonant surface wave frequency. This evidence strongly suggests that the additional evanescent heat transfer comes from the excitation of the surface resonant modes, waves that propagate along the interface and decay exponentially on both sides of the interface. In the next paragraph we are going to explain the role of this kind of waves in the near-field radiative heat exchange.

Upper bound in far-field regime: the blackbody limit

In the far-field regime only the propagative waves play a role in radiative heat transfer. The maximum value that the heat flux can reach can be obtained considering the limiting case of a transmission coefficient $\mathcal{T}^{\alpha} = 1$ for $K < k_0$, which represents the situation of a perfectly absorbing media, i.e. a blackbody. With semi-infinite bodies, this case corresponds to the situation in which the Fresnel reflection coefficients r_{31}^{α} and r_{32}^{α} are zero. In this case, the total net flux takes the form [56, 58]

$$\Phi_{BB}(T_1,T_2) = \int_0^{\infty} d\omega\,[\Theta(\omega,T_1) - \Theta(\omega,T_2)]\frac{\omega^2}{4c^2\pi^2} = \sigma(T_1^4 - T_2^4), \tag{1.16}$$

which is the well-known Stefan-Boltzmann's law (here $\sigma = 2\pi^5 k_B^4/15h^3c^2 = 5.67\cdot 10^{-8}\,\mathrm{W\cdot m^{-2}\cdot K^{-4}}$ is the the Stefan-Boltzmann constant). By linearizing expression (1.16) around T_1, we obtain for a small temperature difference $\Delta T = T_1 - T_2$

$$\Phi_{BB} = 4\sigma T_1^3 \Delta T, \tag{1.17}$$

where we can identify the radiative thermal conductance for the blackbody case at temperature T

$$h_{BB}^{R}(T) = 4\sigma T^3. \tag{1.18}$$

Contribution of resonant surface waves

When a body supports a surface wave a huge energy density [53,59] is confined close to its surface. This energy can be partially transferred by tunneling effect to another solid lying close to it. Below we derive the existence conditions for these resonant modes. First of all, a resonant surface wave is a wave that propagates along the interface and that decays exponentially on both sides of the interface. This wave is an electromagnetic mode of the interface and can be excited resonantly. These waves are polarized and can exist only in p (TM) polarization. Let us consider the case of a plane interface separating two linear, homogeneous and isotropic media with different dielectric constants. As in

the previous paragraph and depicted in Fig. 1.1 the semi-infinite medium 1 fills the half-space $[z, +\infty[$, whereas medium 2 the lower half space starting from $z = 0$. Moreover we assume that these media are dispersive and their the optical response is local, which means that their dielectric permittivity and magnetic permeability only depend on the angular frequency ω.

Existence conditions of a surface wave

As said in the previous section, the surface wave is a resonant-wave solution of Maxwell's equation, that propagates along the interface but decays exponentially in the perpendicular directions. Defining $\mathbf{k} = (\mathbf{K}, k_z)$ and $\mathbf{r} = (\mathbf{R}, z)$, we can express its electric field in the two media, as follows [3, 53]as

$$\mathbf{E_1}(\mathbf{r}, \omega) = \begin{pmatrix} E_{1,x} \\ E_{1,y} \\ E_{1,z} \end{pmatrix} \exp\left[i(\mathbf{K} \cdot \mathbf{R} + k_{z_1} z)\right], \tag{1.19}$$

$$\mathbf{E_2}(\mathbf{r}, \omega) = \begin{pmatrix} E_{2,x} \\ E_{2,y} \\ E_{2,z} \end{pmatrix} \exp\left[i(\mathbf{K} \cdot \mathbf{R} + k_{z_2} z)\right]. \tag{1.20}$$

We first focus on the case of s-polarization. In this case the electric field is perpendicular to the plane (y, z), then the electric field reads

$$\mathbf{E}_1(\mathbf{r}, \omega) = E_{x,1}\hat{\mathbf{x}} \exp\left[i(\mathbf{K} \cdot \mathbf{R} + k_{z_1} z)\right], \tag{1.21}$$

$$\mathbf{E}_2(\mathbf{r}, \omega) = E_{x,2}\hat{\mathbf{x}} \exp\left[i(\mathbf{K} \cdot \mathbf{R} + k_{z_2} z)\right]. \tag{1.22}$$

Using Maxwell's equation to obtain the magnetic field and applying the continuity conditions of the corresponding parallel components of the fields across the interface, we get the following linear system to solve

$$E_{x,1} - E_{x,2} = 0, \tag{1.23}$$

$$k_{z_1} E_{x,1} + k_{z_2} E_{x,2} = 0. \tag{1.24}$$

In order to obtain a non trivial solution its determinant must vanish so that

$$k_{z_1} + k_{z_2} = 0. \tag{1.25}$$

Since $\mathrm{Im}(k_{z_i}) > 0$ this relation cannot be satisfied, which means that no surface waves can exist in s-polarization (TE).

We consider now the electric field in $p-$polarization lies on the (y,z)-plane. In this case the fields on both sides of the interface can be written as:

$$\mathbf{E_1}(\mathbf{r},\omega) = \begin{pmatrix} 0 \\ E_{1,y} \\ E_{1,z} \end{pmatrix} \exp\left[i(Kx + k_{z_1} z)\right], \tag{1.26}$$

$$\mathbf{E_2}(\mathbf{r},\omega) = \begin{pmatrix} 0 \\ E_{2,y} \\ E_{2,z} \end{pmatrix} \exp\left[i(Kx + k_{z_2} z)\right]. \tag{1.27}$$

The continuity conditions for the tangential electric field implies

$$E_{y,1} - E_{y,2} = 0, \tag{1.28}$$

so that $E_{y,1} = E_{y,2} = E_{y,0}$. By using $\boldsymbol{\nabla} \cdot \mathbf{E} = 0$, we can deduce the z components of the field

$$E_{z,1} = -\frac{K}{k_{z_1}} E_{y,0}, \tag{1.29}$$

$$E_{z,2} = \frac{K}{k_{z_2}} E_{y,0}. \tag{1.30}$$

Moreover, imposing the continuity for the $z-$component of the field $\mathbf{D}$, we have

$$\epsilon_1 E_{z,1} = \epsilon_2 E_{z,2} \tag{1.31}$$

Combing the relations (1.28)-(1.31) and imposing the determinant to be equal to zero, we get

$$\epsilon_1 k_{z_2} + \epsilon_2 k_{z_1} = 0, \tag{1.32}$$

which can be recast as

$$K = k_0 \sqrt{\frac{\epsilon_1(\omega)\epsilon_2(\omega)}{\epsilon_1(\omega) + \epsilon_2(\omega)}}. \tag{1.33}$$

This relaxation is the dispersion relation of the surface wave. It implies that the frequency of the surface wave is solution of the equation $\epsilon_1(\omega) = -\epsilon_2(\omega)$. In the next to section we are going to show two examples of surface resonances, first for a dielectric polar material (SiC), and then for a metal (gold). In fact, two types of surface waves exist. The first ones are surface phonon-polaritons, which exist in the infrared, at the interface of polar materials such as silica (SiO_2), silicon carbide (SiC), or II-VI and III-V semiconductors. The second are surface plasmons which appear in the visible wavelength and near-UV domain, on metals. Since phonon-polaritons exist in the IR-region, they can be easily excited at ambient temperature.

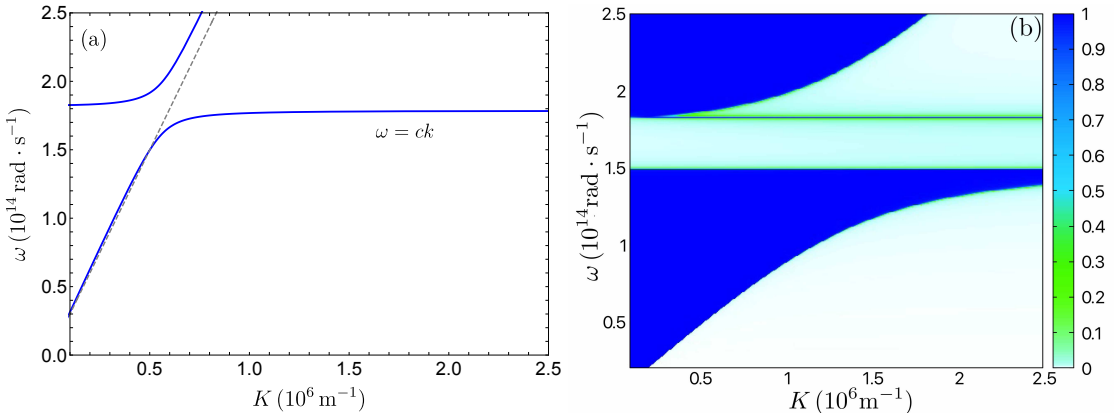

Figure 1.2: (a) Dispersion relation of surface phonon-polariton at the SiC/vacuum interface. **(b)** Transmission coefficient in TM polarization for two SiC slabs separated by a distance $d = 1\,\mathrm{nm}$.

Electrostatic limit

In near-field regime, when $K \gg k_0$ (electrostatic limit) the heat flux (1.8) can be written in a simplified form. In this case, the Fresnel coefficients defined in (1.11) take the simplified form

$$r_{ij}^{\alpha,\mathrm{el}}(\mathbf{K},\omega) \to \begin{cases} 0, & \alpha = s \\ \dfrac{\epsilon_j - \epsilon_i}{\epsilon_j + \epsilon_i}, & \alpha = p \end{cases}, \tag{1.34}$$

since for large K values the perpendicular component k_{z_i} of the wave-vector tends to iK. As explained previously we see from expression (1.34) that at the resonance frequency of the surface wave where $\epsilon_j(\omega) = -\epsilon_i(\omega)$ the reflection coefficient diverges. It is worth noticing from expression (1.15), and performing a straightforward change of variable, i.e. $x = Kd$, that $h_\omega^{R,\mathrm{evan}}(d,T) \propto 1/d^2$ the typical scaling of the near-field radiative heat transfer between polar materials [55, 56, 60].

For the case of a finite system, in which the two slabs have thickness L, the general expression for the reflection coefficient reads

$$R_{ij}^{p} = r_{ij}^{p}(\mathbf{K},\omega)\frac{1 - e^{2ik_{z_i}L}}{1 - [r_p(\mathbf{K},\omega)]^2 e^{2ik_{z_i}L}}. \tag{1.35}$$

In the electrostatic limit we have

$$R_{ij}^{p,\mathrm{el}} \to r_{ij}^{p,\mathrm{el}}(\mathbf{K},\omega)\frac{1 - e^{-2KL}}{1 - [r_{p,\mathrm{el}}(\mathbf{K},\omega)]^2 e^{-2KL}}. \tag{1.36}$$

In order to obtain the surface resonant modes for this system, we need to impose

$$(1 - [r_{ij}^{p,\mathrm{el}}(\mathbf{K},\omega)]^2 e^{-2KL}) = 0, \tag{1.37}$$

which can be decomposed into

$$(1 + r_{ij}^{p,\mathrm{el}}(\mathbf{K}, \omega)e^{-KL})(1 - r_{ij}^{p,\mathrm{el}}(\mathbf{K}, \omega)e^{-KL}) = 0. \tag{1.38}$$

This relation implies that for a finite-size system the surface wave splits into two distinct waves: a symmetric and an anti-symmetric surfaces wave. This is the the so called hybridization mechanism of surface waves.

Polar materials

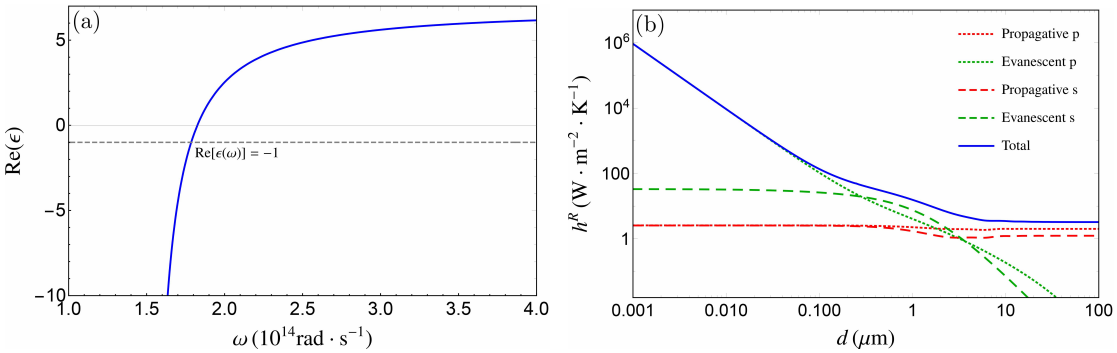

Figure 1.3: **(a)** Real part of the dielectric permittivity of Silicon Carbon sample. The straight dashed gray line represents the condition $\mathrm{Re}[\epsilon(\omega)] = -1$ for which the resonance occurs. The intersection between the two curves shows that the resonance frequency $\omega = 1.786 \cdot 10^{14}$ rad/s is in the infrared. **(b)** Total thermal conductance at 300 K between two semi-infinite slabs of SiC as a function of the separation distance d, and its different wave and polarization contribution.

In the following three sections we are going to consider the cases of two semi-infinite planar bodies made of the same material. We start with the case of a polar dielectric material, silicon carbide that is widely used in the NFRHT; in the following section, the case of a metal that supports surface plasmons in the UV region will be considered, and, finally, the case of a Metal-Insulator Transition (MIT) material, vanadium dioxide.

From now on, we will label all dielectric constants $\epsilon(\omega)$ and will investigate the heat transfer between two SiC samples (i.e. polar material) and two gold sample (i.e. metal) around the ambient temperature ($T = 300$ K). To this end we calculate the thermal radiative conductance $h^R(d)$ and its spectrum. For the case of SiC, the dielectric constant $\epsilon(\omega)$ can be described using the Drude-Lorentz model

$$\epsilon(\omega) = \epsilon_\infty \frac{\omega_L^2 - \omega^2}{\omega_T^2 - \omega^2 + i\Gamma\omega}, \tag{1.39}$$

with $\epsilon_\infty = 6.7$, $\omega_L = 1.8253 \cdot 10^{14}$ rad/s, $\omega_T = 1.4937 \cdot 10^{14}$ rad/s and $\Gamma = 8.9662 \cdot 10^{11}$ rad/s [61]. The dispersion relation for the surface phonon-polariton at the interface

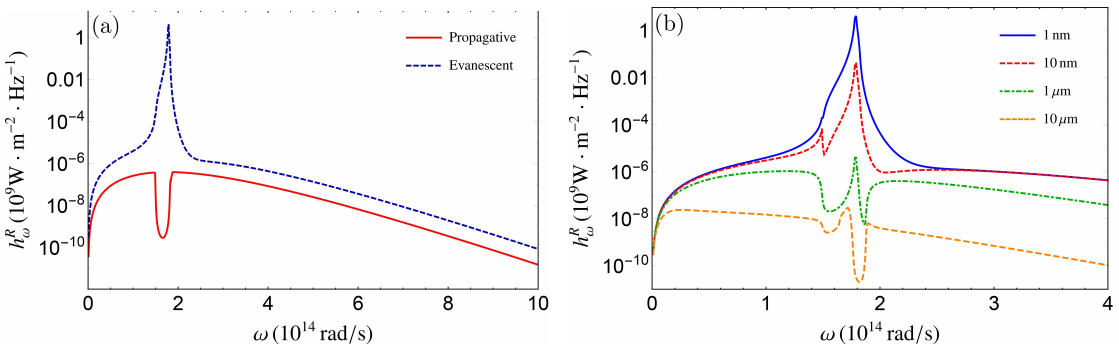

Figure 1.4: **(a)** Thermal conductance spectra at $T = 300\,\mathrm{K}$ for two semi-infinite slabs of SiC separated by a vacuum gap of $1\,\mathrm{nm}$ for propagative (solid, red) and evanescent (blue, dashed) waves. **(b)** Thermal conductance spectra for different separation distances.

SiC/vacuum is shown in Fig. 1.2(a) while in Fig. 1.2(b) is plotted the transmission coefficient for a separation distance $d = 1\,\mathrm{nm}$. The comparison of these two figures reveals that the transmission coefficients takes value close to 1 for the modes (ω, K) satisfying the dispersion relation of the surface wave. Moreover, from expression (1.39) we can deduce the value ω_{max} for which $\mathrm{Re}[\epsilon(\omega_{\mathrm{max}})] = -\epsilon_{\mathrm{vacuum}} = -1$. The value we obtain is $\omega_{\mathrm{max}} = 1.786 \cdot 10^{14}\,\mathrm{rad/s}$, as shown in Fig. 1.3(a), but it is clearly visible also in both curves in Fig. 1.2.

In Fig. 1.3(b) we show the thermal conductance at $300\,\mathrm{K}$ with respect to the separation distance d between the slabs. On this curve we notice an increase of the radiative heat transfer when $d \ll 10\,\mu\mathrm{m}$, the distance where the transition between the far-field regime and the near-field regime takes place. By inspecting the slope of the curve at small distances, we see that the thermal conductance h^R diverges as $1/d^2$ as expected. On the other hand, for distances larger than $10\,\mu\mathrm{m}$ (i.e. far-field regime), the conductance tends to a limiting value independent of the distance.

It is worth noticing that the predominant contribution to the radiative heat transfer at sub-wavelength distances is the one of the evanescent waves with TM (p) polarization. When $d < 0.1\,\mu\mathrm{m}$ the total conductance cannot be distinguished from the conductance due to TM evanescent waves. We can already think that the enhancement observed at short distances is due to the presence of surface polaritons. In order to confirm this hypothesis, we show in Fig. 1.4(a) the spectrum of h^R, for the case $d = 1\,\mathrm{nm}$. We can immediately see the presence of a strong peak around $\omega = 1.786 \cdot 10^{14}\,\mathrm{rad/s}$, a frequency which precisely corresponds to the resonance angular frequency of the surface phonon-polariton. Hence for SiC we can deduce that the enhancement of transfer at short distances is due to the presence of the surface waves. This is confirmed by the conductance spectrum plotted in Fig. 1.4(b) with respect to the separation distance which show the decay of the conductance as the distance becomes larger.

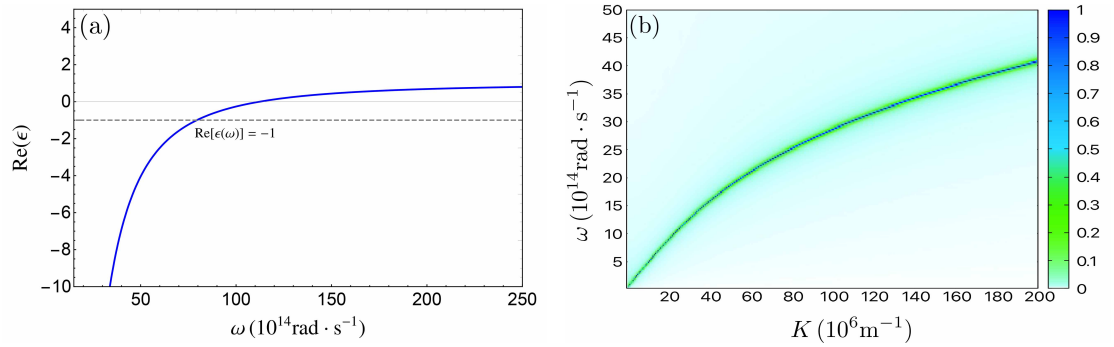

Figure 1.5: Real part of the dielectric permittivity of Gold sample. The straight dashed gray line represents the condition $\mathrm{Re}[\epsilon(\omega)] = -1$ for which the resonance occurs when the sample is surrounded by vacuum. The intersection between the two curves shows that the resonance frequency $\omega = 7.94 \cdot 10^{15}$ rad/s is in the visible. **(b)** Transmission coefficient in polarization TM (p) for two Au sample separated by a distance $d = 1\,\mathrm{nm}$.

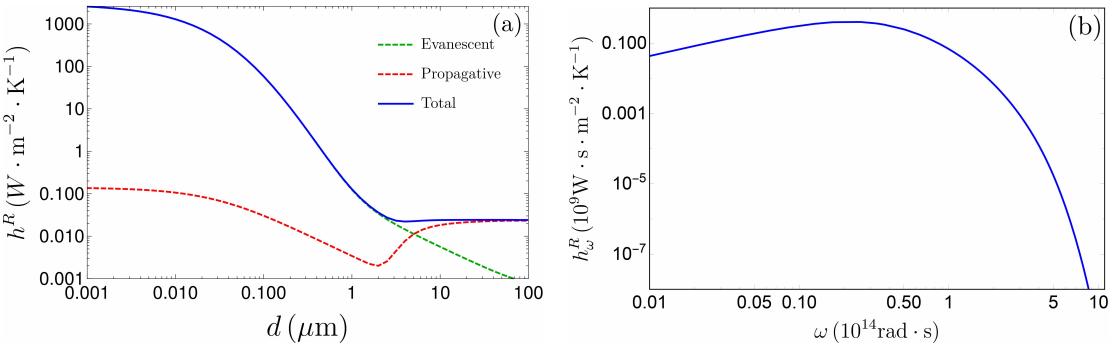

Figure 1.6: **(a)** Thermal conductance at $T = 300\,\mathrm{K}$ for two semi-infinite slabs of Au as a function of the separation distance d, and its different contributions. **(b)** Thermal conductance spectrum for two semi-infinite slab of Au at $T = 300\,\mathrm{K}$ separated by a vacuum gap of 1 nm.

Metals

As we did in the previous paragraph for SiC, we study the NFRHT in the case of two planar semi-infinite metallic bodies, that support surface waves in the UV region. To model their dielectric constant we use the Drude model [62]

$$\epsilon(\omega) = 1 - \frac{\omega_P^2}{\omega^2 + i\Gamma\omega}. \tag{1.40}$$

In the case of gold (Au) samples the model parameters are $\omega_p = 11.23 \cdot 10^{15}$ rad/s and $\Gamma = 4.05 \cdot 10^{13}$ rad/s. In a similar way to SiC discussed above we can deduce the value ω_{max} for the resonance frequency of the surface wave supported by a semi-infinite gold sample. In this case, the value is $\omega_{\mathrm{max}} = \omega_p/\sqrt{2} \simeq 7.94 \cdot 10^{15}$ rad/s. As shown in

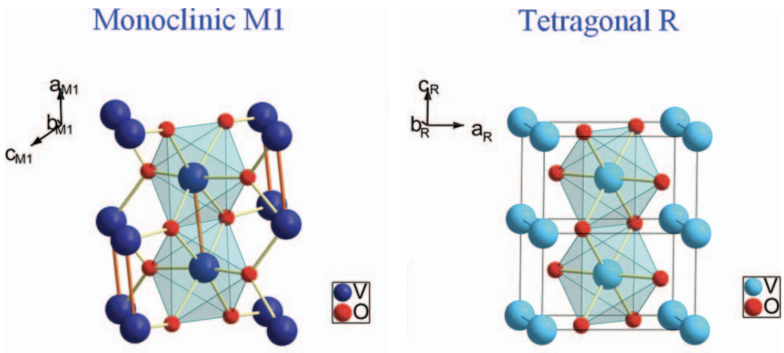

Figure 1.7: Schematic representation of the crystal structures of VO_2 at low temperature (monoclinic M1 phase) and high temperature (tetragonal rutile R phase).

Fig. 1.5(a), this resonance frequency is at the limit of the visible range. In Fig. 1.5(b) the transmission coefficient for a separation distance $d = 1\,\text{nm}$ is represented. In a similar way to the case of SiC, the transmission coefficient in TM polarization takes values close to 1 for the modes (ω, K) satisfying the dispersion relation of the surface wave. In Fig. 1.6(a) we show the thermal radiative conductance and its propagative and evanescent contributions as a function of the distance. We can see on these curves that there is an increase of the radiative heat transfer when $d < 0.3\,\mu\text{m}$. Nevertheless, the increase is one order of magnitude less that the one we observed for the SiC. In Fig. 1.6(b) the thermal conductance spectrum show a behavior which is similar to the blackbody spectrum. The absence of peaks in this spectrum comes from the fact that, unlike SiC, gold does not support surface waves in the Planck window at $T = 300\,\text{K}$, since unlike polar materials the TM modes do not dominate in metal in the electrostatic limit [3].

Phase-change materials: vanadium dioxide

Recently, phase-change materials have been considered in the study of NFRHT [14, 31, 45–47, 63–66]. They offer way to tune the radiative heat transfer, giving the possibility to significantly enhance or reduce the heat flux by changing the temperature around a critical temperature T_c. Vanadium dioxide (VO_2) is one of such materials for many applications in optical, thermal and electrical systems. This material undergoes an insulator-to-metal transition at $T_c = 340\,\text{K}$, really close to ambient temperature, and, more specifically, at lower temperatures, it behaves as an insulator and at higher temperatures as a metal. This transition results from a change in its crystal structure from a monoclinic (M1) structure below T_c to a tetragonal rutile-like structure (R), above the transition temperature (see Fig. 1.7). As a consequence of this change, the optical and electrical responses are deeply affected. The main interest in the use of VO_2 is

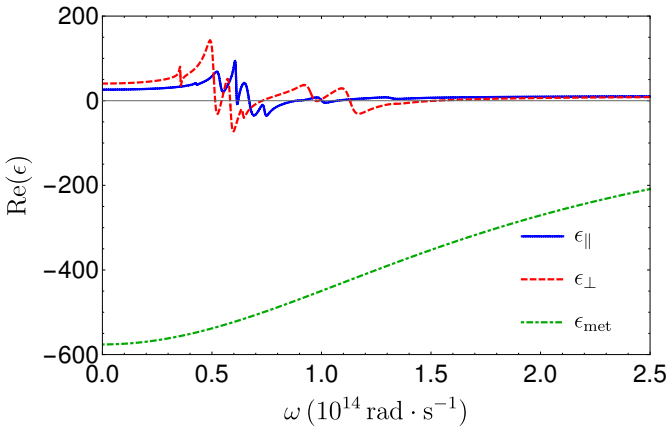

Figure 1.8: Real part of the dielectric permittivity of VO_2. The blue and the red-dashed curves represent the permittivity for the dielectric phase ($T < T_c$). In this phase (monoclinic) the material is anisotropic (uniaxe). The blue curve represents the permittivity parallel to the optical axis while the red curve corresponds to the permittivity orthogonal to this axis. The green-dot dashed curve represents the real part of the dielectric permittivity of VO_2 in the metallic case, $T > T_c$ (rutile phase).

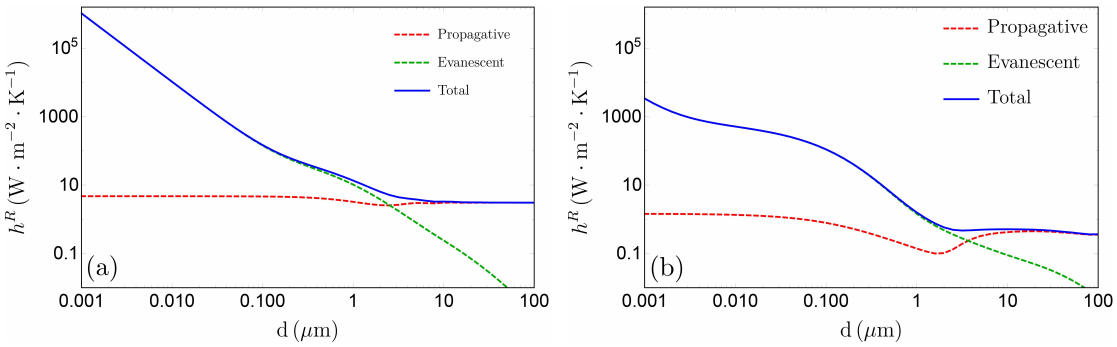

Figure 1.9: **(a)** Thermal conductance at $T = 300\,\mathrm{K}$ for two semi-infinite slabs of VO_2 as a function of the separation distance d, and its different wave contribution in the dielectric phase ($T < T_c$). **(b)** Thermal conductance at $T = 350\,\mathrm{K}$ for two semi-infinite slabs of VO_2 as a function of the separation distance d, and its different contributions in the metallic phase ($T > T_c$).

the possibility to break the symmetry in the heat transfer in a 2-body system when the sign of the temperature gradient is changed. This has allowed the design of radiative thermal diode [31, 47]. Based on this asymmetry, using this material we can modulate by orders of magnitude the radiative heat transfer switching from the metallic to the insulating phase. Using more elaborate systems it is also possible to amplify the heat transfers [65], build volatile thermal memory [45] and make boolean treatment of information [46] using logical circuits with VO_2 based materials. We now describe the

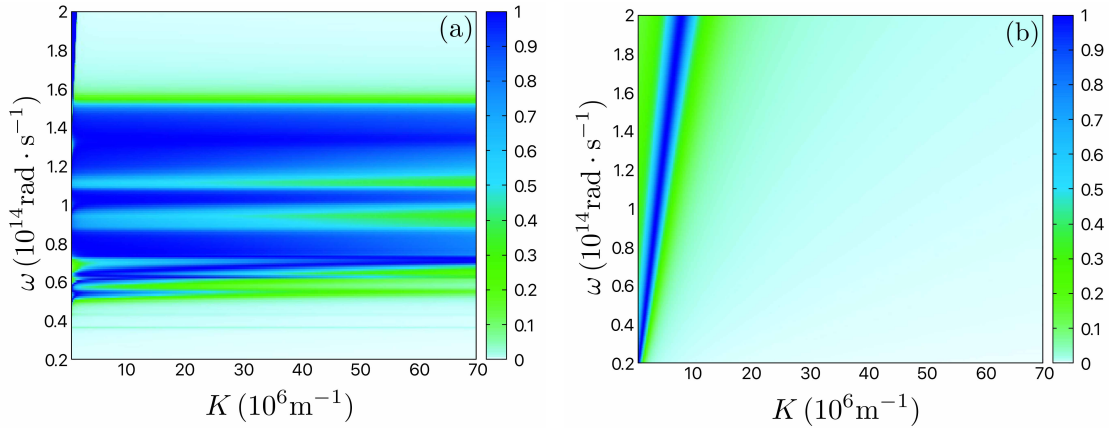

Figure 1.10: (a) Transmission coefficient in TM (p) polarization for VO_2 in the dielectric phase ($T < T_c$), as a function of the frequency and of the parallel wavevector. **(b)** Transmission coefficient in polarization TM (p) for VO_2 in the metallic phase ($T > T_c$), as a function of the frequency and of the parallel wavevector.

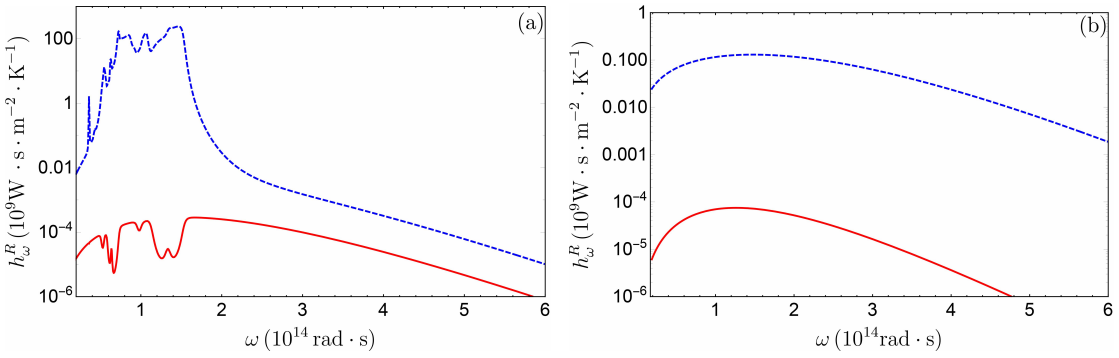

Figure 1.11: (a) Thermal conductance spectrum for two semi-infinite slab of VO_2 in the dielectric phase, at $T = 300\,\mathrm{K}$, separated by a vacuum gap of $1\,\mathrm{nm}$ for the propagative (solid, red) and evanescent (blue, dashed) waves. **(b)** Thermal conductance spectrum for two semi-infinite slabs of VO_2 in the metallic phase, for $T = 350\,\mathrm{K}$, separated by a vacuum gap of $1\,\mathrm{nm}$ for the propagative (solid, red) and evanescent (blue, dashed) waves.

radiative heat exchange between two slabs of VO_2. First of all, when the temperature of VO_2 is below T_c, its permittivity is not that one of an uniaxial anisotropic medium and takes the form

$$\epsilon = \begin{pmatrix} \epsilon_\perp & 0 & 0 \\ 0 & \epsilon_\perp & 0 \\ 0 & 0 & \epsilon_\parallel \end{pmatrix}, \tag{1.41}$$

where $\epsilon_\parallel$ is the permittivity value along the optical axis and $\epsilon_\perp$ is the permittivity in the plane orthogonal to this axis. The values for $\epsilon_\perp$ and $\epsilon_\parallel$ are obtained through optical

data [64, 67], and fitted with the following model

$$\begin{aligned}\epsilon_{\parallel} &= \epsilon_{\infty,\parallel} + \sum_{i=1}^{8} \frac{s_{\parallel,i}}{1-(\omega/\omega_{\parallel,i})^2 - i\, g_{\parallel,i}\, \omega/\omega_{\parallel,i}},\\ \epsilon_{\perp} &= \epsilon_{\infty,\perp} + \sum_{i=1}^{8} \frac{s_{\perp,i}}{1-(\omega/\omega_{\perp,i})^2 - i\, g_{\perp,i}\, \omega/\omega_{\perp,i}},\end{aligned} \tag{1.42}$$

where the fitting parameters are taken from [67]. On the contrary, for the metallic phase, VO_2 is isotropic and its permittivity can be modelized, taking into account the losses, as

$$\epsilon(\omega) = -\epsilon_{\infty}\frac{\omega_p^2}{\omega^2 i\, \omega\, \omega_c} \tag{1.43}$$

in which $\omega_p = 15.0796 \cdot 10^{14}$ rad/s, $\epsilon_{\infty} = 9$, $\omega_c = 1.88496 \cdot 10^{14}$ rad/s and i is the imaginary unit. While for the metallic case the calculation for the RHT remains the same as the one describe previously with gold, in the dielectric phase the expression of k_z depends on the polarization and the Fresnel's coefficients change as follows

$$k_z^s = \sqrt{\epsilon_{\perp} k_0^2 - K^2}, \qquad k_z^p = \sqrt{\epsilon_{\perp} k_0^2 - \frac{\epsilon_{\perp}}{\epsilon_{\parallel}} K^2}, \tag{1.44}$$

$$r_{ij}^s = \frac{k_{z_i}^s - k_{z_j}}{k_{z_i}^s - k_{z_j}}, \qquad r_{ij}^p = \frac{\epsilon_{i,\perp} k_{z_i}^p - \epsilon_j k_{z_j}}{\epsilon_{i,\perp} k_{z_i}^p + \epsilon_j k_{z_j}}, \tag{1.45}$$

where the body i is composed of VO_2, while the body j is a general isotropic material. It is easy to see that in the case $\epsilon_{\perp} = \epsilon_{\parallel}$ we re-obtain the well-known expression for the reflections coefficients and $k_z^s = k_z^p$. In Fig. 1.8 we represent the real part of the dielectric constants $\mathrm{Re}[\epsilon(\omega)]$ for the dielectric and the metallic phase. Since expression (1.9) remains valid in the anisotropic case, the only difference in the calculation of the heat flux is due to the new definition for the perpendicular wavevectors and for the Fresnel's reflection coefficients. In Fig. 1.9 (a) and (b) we show the thermal conductance and the contributions of the propagative and evanescent waves as a function of the separation distance d, for the dielectric and the metallic phase, respectively. Comparing the two figures we can see that the enhancement in the near field is always more pronounced in the dielectric phase with respect to the metallic phase. In the dielectric case a strong enhancement in the radiative heat transfer in the near-field regime is enlighten while for $d > 10\,\mu$m the value is almost independent on the distance d. A shown in Fig. 1.10 (a) the enhancement in the near-field regime is clearly due to the presence of surface waves. These waves correspond to the resonance of Fresnel coefficient r^p defined in (1.45). In Figs. 1.10 (b), we can see that the behavior dramatically changes at the transition. Beyond T_c the surface waves disappear and the transmission coefficient almost vanishes for$K > \omega/c$. The conductances plotted in Fig. 1.11 confirm this change.

1.3 Conclusions

In this chapter we have introduced the theoretical framework for studying the radiative heat transfer, both in the far- and in the near-field regime between two bodies. We started by reminding the link existing between the Poynting vector and the fluctuating currents inside a body with temperature $T > 0\,\mathrm{K}$. We then focused on the heat transfer between two semi-infinite planar bodies composed of the same material and gived the general expressions of heat flux both in far-field and in near-field regime. We then explained their role played by the evanescent and propagative waves on the radiative heat transfer in these two regimes, paying a particular attention to the role of surface waves. Moreover, we recovered the blackbody limit from the fluctuational electrodynamics and highlighted the dependence of the radiative heat flux in the near field regime on d^{-2} for polar materials. We have described through simple examples the main specificities of radiative heat transfer in hear field regime between polar materials and between metals. In particular, we have shown that the presence of surface waves in the Planck window drastically magnifies heat exchanges in near-field regime. Finally, we have briefly discussed the radiative heat exchanges in a system made of metal-insulator phase change material and shown that a drastic change of heat flux can occur around the critical temperature of material.

Chapter 2

Bistable thermomechanical oscillator

Processing information with heat rather than with electric currents to perform logical operations is a challenging problem in modern physics [68]. Several directions have been explored during the last decade to this end. In 2004 Li et al. [69] have demonstrated the possibility to locally break the symmetry for the phonon propagation inside non-linear atomic lattices when the sign of temperature gradient is changed (thermal analog of diodes). Later phononic transistors have been proposed [69] opening so the door to the dynamical control and application of heat flow in solid-state elements and consequently to a possible logical treatment of information carried by thermal phonons [68, 70, 71]. More recently, to overcome the inherent problems associated with the relatively small propagation speed of acoustic phonons, photonics systems have been proposed to achieve similar operations [31, 45, 46, 48, 65] in contactless two- and many-body systems [42, 57, 72, 73]. Finally, heat transport mediated by spin waves has also been considered [74] to rectify heat flux in many-body systems, paving thus the way to handle heat flux in quantum devices and open prospects in the field of thermal computing at cryogenic temperature.

In this chapter we explore the possibility to make information treatment using mechanical systems made with phase-change materials driven by radiative heat flux.These systems have been used as sensors [75–79] since a long time in order to directly measure heat flux by measuring the displacement of cantilevers made with such materials in a temperature range around their critical temperature. Here we introduce a bistable mechanical system made with a bimaterial VO_2-dielectric cantilever in which the simultaneous thermal interaction of the beam in near-field regime [14, 31, 63, 66] with a substrate and in far field [47, 80] with a thermal bath is considered. In the first section of this chapter we discuss how a many-body thermal system can admit more than one equilibrium (steady-state) temperature distribution and how this feature has been and can been exploited in order to process information. In Sec. 2.2 we discuss the equation for the phonons governing the dynamics of a beam, focusing on the case of a cantilever and obtaining its normal modes. In Sec. 2.3 we study more in detail the physics of a bi-

material cantilever, introducing its effective quantities and the bending thermal moment due to the mismatch between the thermal expansion coefficients of its composing layers. Introducing our system consisting of a phase-change bimaterial cantilever, in Sec. 2.4, we numerically solve the coupled differential system composed of the Euler-Bernoulli and energy-balance equations, highlighting a thermomechanical bistable behavior and studying its existence as a function of the thermal and geometrical parameters of the system. In the last section, we finally discuss the potential of these systems to make a thermal memory and to perform basic logical operator.

2.1 Equilibrium temperatures and stability studies

Let us consider a many-body system composed of N objects assumed at uniform temperatures $\{T\} = \{T_1, \dots, T_N\}$ in mutual interaction. We can formally describe the temporal evolution of their thermal state through the equation [57]

$$\rho_i C_{p,i} V_i \frac{dT_i}{dt} = P_i(\{T\}, t), \tag{2.1}$$

where the Left Hand Side (LHS) represents the thermal inertia defined by the specific heat capacity $C_{p,i}$, the volume V_i of the object and its density ρ_i. P_i is the net power received by the body i through N-body interactions. It can be expressed as

$$P_i(\{T\}, t) = \sum_{j \neq i} P_{i,j}(\{T\}, t) + P_{i,b}(\{T\}, T_b, t), \tag{2.2}$$

where $P_{i,j}$ is the power exchanged between objects i and j, while $P_{i,b}$ is the exchanged power between i and the background. Close to thermal equilibrium the system of equation can be linearized by means of the pairwise conductances $G_{i,j} \equiv \partial P_{i,j}/\partial T_i$ and $G_{i,b} \equiv \partial P_{i,b}/\partial T_i$ so that

$$P_i(\{T\}, t) \approx \sum_{j \neq i} G_{i,j}(\{T\}, t)(T_j - T_i) + G_{i,b}(\{T\}, T_b, t)(T_b - T_i). \tag{2.3}$$

The thermal steady state $\{T\}$ of Eq. (2.1) is obtained by solving the system of equation

$$P_i(\{T\}) = 0, \quad i = 1, \dots, N. \tag{2.4}$$

Each of these equations gives rise to a hypersurface in the N-dimensional temperature space, and it corresponds to the partial equilibrium of body i. The intersection of these hyperspaces represents the global steady-state for the system. When all P_i depend linearly on the temperatures (i.e. $G_{i,j}$ and $G_{i,b}$ are temperature-independent), the system (2.4) admits only one solution. On the other hand, when these conditions are

not met, the system of equations (2.4) can admit more than one solution, which can be either stable or unstable [81].

The demonstration of multistable thermal behaviors in many-body systems paved the way to the possibility of designing thermal analogs of electronic-based logic gate. In these system we are considering that the temperature-dependent properties of a phase-change material, as we will show, are a the origin of the multistability. These states can naturally be identified to the "0" and "1" of one bit of information and can be used as memory [45]. As long as these states are held constant, the system remains in a stable thermal state but, when a perturbation is added to the system, it is possible to switch from one thermal state to the other state.

In the following, we are going to show that the coupling between thermal and mechanical behavior of a bimaterial cantilever can be exploited to make thermal logical operations. To start, we will describe the modeling of the mechanical dynamics of a simple beam cantilever.

2.2 Euler-Bernoulli beam theory

For a beam of length L with its axis along the x-direction, we denote the deflection of the beam in the y-direction from its axis as $u(x,t)$. For sufficiently thin beams, we can assume these systems as unidimensional objects extended only along the x-axis, with mass per unit length μ, Young's modulus E and second moment of area I. The product EI, known as flexural rigidity, is supposed independent of x. In order to describe the dynamic evolution of beam, we introduce the action [82]

$$\int_{t_1}^{t_2}\int_0^L \left[\frac{1}{2}\mu\left(\frac{\partial u(x,t)}{\partial t}\right)^2 - \frac{1}{2}EI\left(\frac{\partial u^2}{\partial x^2}\right)^2 + q(x,t)u(x,t)\right]dxdt, \tag{2.5}$$

where the first term represents the kinetic energy, the second one is the potential energy due to internal forces while the third term indicates the potential energy due an the external load $q(x,t)$. The displacement $u(x,t)$ can be obtained by minimizing this action using the Euler-Lagrange equation. This leads to

$$EI\frac{\partial^4 u(x,t)}{\partial x^4} = -\mu\frac{\partial^2 u(x,t)}{\partial t^2} + q(x,t). \tag{2.6}$$

We usually refer to this equation as the Euler-Bernoulli equation.

Free oscillations of a cantilever

The free vibration of a beam attached to a wall at one of its ends, can be obtained by solving this equation in the case without external load $q(x,t)$. In this case, the Euler-

Bernoulli equation reduces to

$$EI\frac{\partial^4 u(x,t)}{\partial x^4} = -\mu\frac{\partial^2 u(x,t)}{\partial t^2}. \tag{2.7}$$

This equation can be solved by means of a Fourier decomposition of the displacement into the sum of harmonic vibrations of the form $u(x,t) = \mathrm{Re}[\hat{u}(x)e^{-i\omega t}]$, where ω is the oscillation frequency. Using this expression, we obtain the simplified differential equation

$$EI\frac{d^4\hat{u}(x)}{\partial x^4} = \mu\omega^2\hat{u}(x), \tag{2.8}$$

with the following general solution for $\hat{u}(x)$

$$\hat{u}_n(x) = A\cosh(\beta_n x) + B\sinh(\beta_n x) + C\cos(\beta_n x) + D\sin(\beta_n x), \tag{2.9}$$

where $\beta_n = \sqrt[4]{\mu\omega_n^2/EI}$. The ω_n are the natural frequencies of the beam and each displacement solution is a mode of the system. In the case of a beam attached to a wall at its left end $(x = 0)$ and free to oscillate at its right end $(x = L)$, the boundary conditions in the absence of external load, are

$$\begin{cases} \hat{u}_n(0) = 0, \\ \dfrac{\partial\hat{u}_n}{\partial x}(0) = 0, \\ \dfrac{\partial^2\hat{u}_n}{\partial x^2}(L) = 0, \\ \dfrac{\partial^3\hat{u}_n}{\partial x^3}(L) = 0. \end{cases} \tag{2.10}$$

The first two boundary conditions, i.e. zero displacement and zero derivative at the fixed left end $x = 0$, describe the wall support (vanishing displacement and speed), while the third and the forth impose a zero bending moment and shear force at $x = L$, respectively. Applying these conditions we get the following linear system

$$\begin{cases} A + C = 0, \\ B + D = 0, \\ A\cosh(\beta L) + B\sinh(\beta L) - C\cos(\beta L) + D\sin(\beta L) = 0, \\ A\sinh(\beta L) + B\cos(\beta L) + C\sin(\beta L) + D\cos(\beta L) = 0, \end{cases} \tag{2.11}$$

which admits non-trivial solutions only for

$$\cosh(\beta_n L)\cos(\beta_n L) + 1 = 0. \tag{2.12}$$

The first four roots of this transcendental equation are $\beta_1 L = 1.875$, $\beta_2 L = 4.694$, $\beta_3 L = 7.855$ and $\beta_4 L = 10.996$. The corresponding natural frequency can be obtained

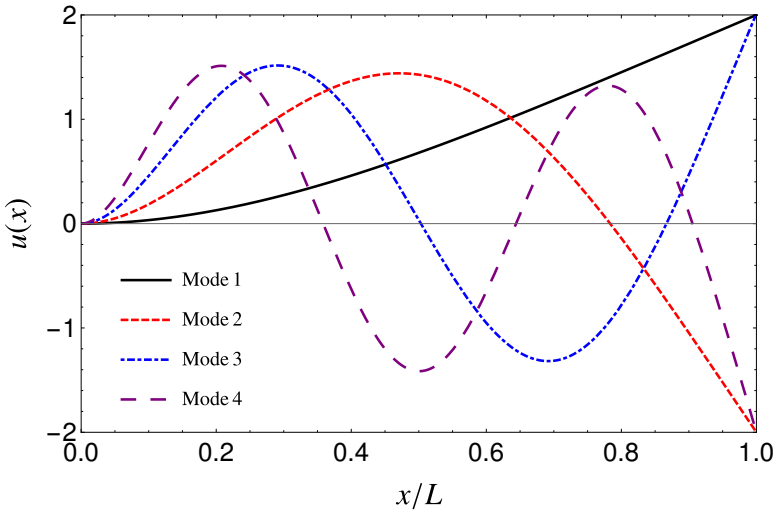

Figure 2.1: Representation of the mode shapes for the first four modes of an oscillating cantilever beam.

as $\omega_n = \beta_n^2\sqrt{EI/\mu}$. Solving now system in Eq. (2.11) for the coefficients A, B, C and D, we obtain the following displacement $\hat{u}_n(x)$

$$\hat{u}_n(x) = \cosh(\beta_n x) - \cos(\beta_n x) + \frac{\cos(\beta_n L) + \cosh(\beta_n L)}{\sin(\beta_n L) + \sinh(\beta_n L)}[\sin(\beta_n x) - \sinh(\beta_n x)], \tag{2.13}$$

where we have taken $A = 1$. The modes corresponding to the first four natural frequencies of the cantilever are represented in Fig. 2.1.

2.3 Bimaterial cantilever

In the following, we will focus on the specific case of a bimaterial cantilever, i.e. a beam composed of two layers of different materials. For this reason we first introduce the main features of such system. They are usually of micrometer size in order to be sensitive to the phase-change in one layer. This feature enables high responsivity, and consequentially a strong sensitivity to external actuations. For example, bimaterial microcantilevers have been used successfully for sensitive thermal measurements of near-field radiative heat transfer [7].

For bimaterial cantilevers, the mass density ρ, specific heat capacity C, thermal conductivity κ and flexural rigidity EI need to be replaced by effective quantities. Let us assume that the two materials composing the beam have Young's moduli E_1 and E_2, densities ρ_1 and ρ_2, specific heat capacities C_1 and C_2, and thermal conductivities κ_1 and κ_2. We can obtain the effective quantities ρ, κ and C as weighted averages. More

specifically, ρ and κ can be obtained using as weights the volumes of each layer V_1 and V_2, i.e.

$$a = \frac{a_1 V_1 + a_2 V_2}{V_1 + V_2}, \tag{2.14}$$

where $a \in \{\rho, \kappa\}$. For the specific heat capacity, instead, we use as weights the mass of each layer $m_1 = \rho_1 V_1$ and $m_2 = \rho_2 V_2$, obtaining

$$C = \frac{C_1 m_1 + C_2 m_2}{m_1 + m_2}. \tag{2.15}$$

Concerning the flexural rigidity EI, the effective one can be obtained as follows [83,84]

$$EI = \frac{\delta h_1 h_2}{12} \frac{E_1 h_1 E_2 h_2}{E_1 h_1 + E_2 h_2} K, \tag{2.16}$$

with

$$K = 6 + 4\left(\frac{h_1}{h_2} + \frac{h_2}{h_1}\right) + \left(\frac{E_1 h_1^2}{E_2 h_2^2} + \frac{E_2 h_2^2}{E_1 h_1^2}\right). \tag{2.17}$$

A bimaterial cantilever, because of the mismatch between the thermal expansion coefficients of the two layers, α_1 and α_2, remains straight only when the temperature all along the beam is equal to the building temperature T_0. The different expansion of the two parts causes a bending that can be expressed as a function of the beam construction temperature T_0, its temperature profile $T(x,t)$ and the thermal expansion coefficients α_1 and α_2 of the two materials, in the following way [85]

$$\frac{\partial^2 u(x,t)}{\partial x^2} = 6\frac{(\alpha_2 - \alpha_1)}{K}\left(\frac{1}{h_1} + \frac{1}{h_2}\right)[T(x,t) - T_0], \tag{2.18}$$

the bending thermal moment associated with it

$$M_T[T(x,t)] = EI\frac{\partial u^2(x,t)}{\partial x^2}. \tag{2.19}$$

The second derivative of this thermal moment plays the role of the external load $q(x,t)$ in the Euler-Bernoulli equation (2.6).

2.4 Thermomechanical bilayer cantilever system

We now study the thermomechanical behavior of a bimaterial microcantilever composed of SiO_2 and a MIT material, in particular VO_2. As explained in Sec. 1.2, VO_2 is a phase-change material which undergoes a first-order transition from an insulating to a metallic behavior when its temperature goes beyond $T_c = 340\,\mathrm{K}$ [67]. We chose this material as second component of the bimaterial cantilever in order to highlight a

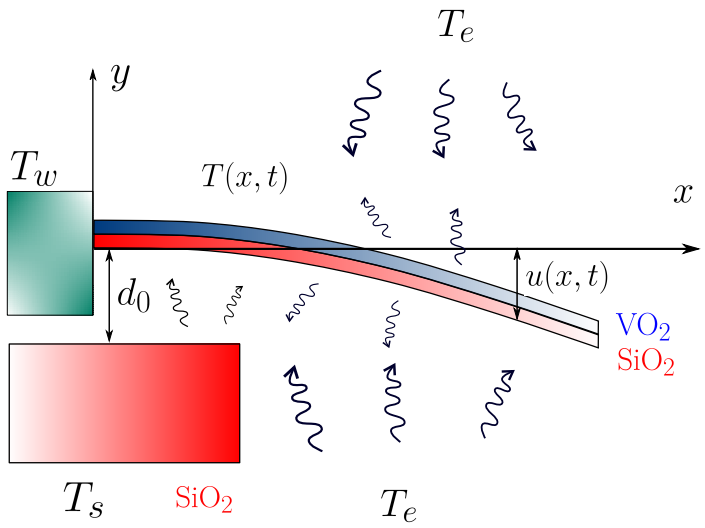

Figure 2.2: Sketch of thermomechanical oscillator. A bilayer cantilever is recessed at its left end by in a wall at temperature T_w and kept free at the other end. It interacts through radiative heat transfer with an environment at temperatures T_e and in near field with a substrate at temperature T_s. Its vertical displacement is described by $u(x,t)$, while $T(x,t)$ represents its temperature profile.

bistable behavior. The system is depicted in Fig. 2.2. The beam is recessed in a wall maintained at temperature T_w by an external power source, whereas its right end is left free to oscillate. This cantilever exchanges heat radiatively with an environment at temperature T_e and in near field with a substrate at temperature T_s. Moreover, the two different layers have thicknesses (y axis in Fig. 2.2) h_1 and h_2 ($h = h_1 + h_2$). Its length (x axis in Fig. 2.2) and width (z axis) are L and δ, respectively. The bottom layer of the cantilever is made of SiO_2 [61], while the upper one of VO_2. The substrate has length l and is made of SiO_2 in order to maximize the near-field heat transfer with the cantilever bottom layer.

The time evolution of the cantilever displacement $u(x,t)$ and temperature profile $T(x,t)$ is governed by the coupled system of nonlinear differential equations

$$\begin{cases} \rho\, C_p h \dfrac{\partial T(x,t)}{\partial t} = h\kappa \dfrac{\partial^2 T(x,t)}{\partial x^2} + \Phi\big[u(x,t), T(x,t)\big], \\ EI \dfrac{\partial^4 u(x,t)}{\partial x^2} = -\mu \dfrac{\partial^2 u(x,t)}{\partial t^2} - \gamma \dfrac{\partial u(x,t)}{\partial t} - \dfrac{\partial^2 M_T[T(x,t)]}{\partial x^2}, \end{cases} \tag{2.20}$$

where the first one is the energy-balance equation of the beam, while the second is the Euler-Bernoulli [83] or momentum-conservation equation discussed in Sec. 2.2. In the Right Hand Side (RHS) of the latter equation we added the damping term $\gamma \partial u(x,t)/\partial t$,

which allows an energy dissipation depending on the nature of the surrounding media through the damping factor γ, and a load term related to $M_T[T(x,t)]$, the thermal bending moment expressed in Eq. (2.19). Here ρ, C_p and κ are the effective-beam mass density, specific heat capacity and thermal conductivity, respectively, we have defined in the previous section. Here Φ denotes the heat flux per unit surface between two parallel planes, so that $\Phi\delta dx$ is the net energy received per unit time by the infinitesimal element of the beam between x and $x+dx$. The idea of calculating the interaction between curved surfaces as a sum of plane-plane contributions closely follows the Proximity Approximation (see e.g. Ref. [86]), typically used in the context of Casimir forces and near-field radiative heat exchanges, valid when the curvature radii are much larger than the distance, condition fully met for the cantilever displacements we obtain here.

In order to calculate the radiative term in Eq. (2.20), we use the radiative conductance $h^R(T,d)$ as introduced in Chap. 1 by assuming that the system works close to a thermal equilibrium state. More specifically, we express this conductance through a polynomial expansion with respect to the separation distance

$$h^R(T,d) = \sum_{n=0}^{\infty} A_n d^{-n}. \tag{2.21}$$

The calculation of radiative flux allowed us to show that

$$h^R(T,d) = A_0 + A_2 d^{-2}, \tag{2.22}$$

where $A_0 = 10.9\,\mathrm{W}\cdot\mathrm{m}^{-2}\cdot\mathrm{K}^{-1}$ and $A_2 = 3.61\times10^{-12}\,\mathrm{W}\cdot\mathrm{K}^{-1}$ are the fitting parameters calculated by simultaneously accounting for the far-field exchanges with the environment and the near-field exchanges with the substrate. We see that we recover the typical d^{-2} behavior of h^R between polar materials.

The initial and the boundary conditions we need to impose for the beam temperature profile are the following

$$\begin{cases} \dfrac{\partial T(L,t)}{\partial x} = 0, \\ T(0,t) = T_w, \\ T(x,0) = f(x). \end{cases} \tag{2.23}$$

The first corresponds to the adiabatic conditions on its free end. The second condition sets the beam temperature on its recessed end, while the third condition defines the temperature profile at the initial moment. Concerning the displacement, we impose the

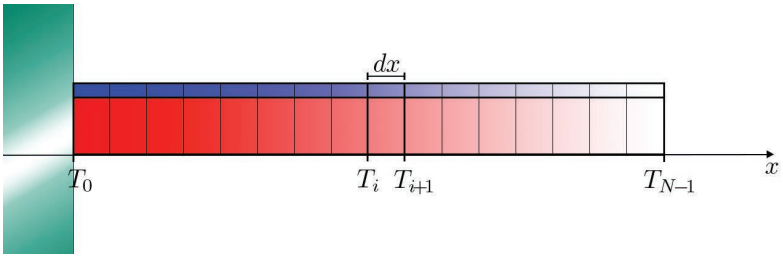

Figure 2.3: Graphical representation of the uniform spatial discretization of the cantilever. Each slice has thickness dx.

following conditions

$$\begin{cases} u(0,t) = 0, \\ \dfrac{\partial u(0,t)}{\partial x} = 0, \\ \dfrac{\partial^2 u(L,t)}{\partial x^2} = M_T[T(L,t)], \\ \dfrac{\partial^3 u(L,t)}{\partial x} = 0, \\ u(x,0) = g(x), \\ \dfrac{\partial u(x,0)}{\partial t} = 0. \end{cases} \tag{2.24}$$

As for the free-oscillations case discussed in Sec. 2.2, we impose here $u(0,t) = \partial u(0,t)/\partial x = \partial^3 u(0,t)/\partial x^3 = 0$ [87], while for a bimaterial cantilever the bending moment is not zero and is equal to the thermal moment of Eq. (2.19) [85]. With the last two conditions, we impose an initial displacement with shape $g(x)$, and an initial velocity of any element of the beam equal to zero.

Numerical method

The complexity of the coupled system (2.20) does not allow to solve it analytically. To solve this system of non-linear coupled differential equation we use a finite-difference method [88,89], discretizing the beam in $N-1$ intervals as shown in Fig. 2.3 and substituting each derivative with the centered-discretized (backward-discretized)

counterparts for the spatial (temporal) ones, rewriting Eq. (2.20) as follows

$$\begin{cases} \rho C_p h \dfrac{T_i^m - T_i^{m-1}}{dt} = h\kappa \dfrac{T_{i+1}^{m-1} - 2T_i^{m-1} + T_{i-1}^{m-1}}{dx^2} + \Phi(\{u_i^{m-1}\},\{T_i^{m-1}\}), \\ EI \dfrac{u_{i+2}^{m-1} - 4u_{i+1}^{m-1} + 6u_i^{m-1} - 4u_{i-1}^{m-1} + u_{i-2}^{m-1}}{dx^4} = -\mu \dfrac{u_i^m - 2u_i^{m-1} + u_i^{m-2}}{dt^2} \\ \qquad\qquad -\gamma \dfrac{u_i^m - u_i^{m-1}}{dt} - \dfrac{M_T(T_{i+1}^{m-1}) - 2M_T(T_i^{m-1}) + M_T(T_{i-1}^{m-1})}{dx^2}. \end{cases} \tag{2.25}$$

in which $\{u_i^{m-1}\}$ and $\{T_i^{m-1}\}$ indicate the entire displacement and temperature profiles at the instant $m-1$, respectively. Solving for T_i^{m+1} and u_i^{m+1}, we obtain

$$\begin{cases} T_i^m = T_i^{m-1} + \dfrac{dt}{\rho C_p h}\left[h\kappa \dfrac{T_{i+1}^{m-1} - 2T_i^{m-1} + T_{i-1}^{m-1}}{dx^2} + \Phi(\{u_i^{m-1}\},\{T_i^{m-1}\})\right], \\ u_i^m = \dfrac{(2\mu + \gamma dt)u_i^{m-1} - \mu u_i^{m-2}}{\mu + dt\gamma} - \dfrac{dt^2}{\mu + dt\gamma}\left[\dfrac{M_T(T_{i+1}^{m-1}) - 2M_T(T_i^{m-1}) + M_T(T_{i-1}^{m-1})}{dx^2}\right. \\ \qquad \left. + EI \dfrac{u_{i+2}^{m-1} - 4u_{i+1}^{m-1} + 6u_i^{m-1} - 4u_{i-1}^{m-1} + u_{i-2}^{m-1}}{dx^4}\right]. \end{cases} \tag{2.26}$$

In order to impose the boundary and the initial conditions for the temperature expressed in Eq. (2.23), as we have done discretizing the system, we use the finite differences at first order of accuracy for the temporal derivation and at the second order for the spatial one, obtaining

$$\begin{cases} T_{N-1}^m = \dfrac{4}{3}T_{N-2}^m - 3T_{N-3}^m, \\ T_0^m = T_w, \\ T_i^0 = f(x_i). \end{cases} \tag{2.27}$$

For the displacement $u(x,t)$ the conditions in Eq. (2.24) are discretized as follows

$$\begin{cases} u_0^m = 0, \\ u_1^m = 0, \\ u_{N-1}^m = \dfrac{48u_{N-3}^m - 52u_{N-4}^m + 15u_{N-5}^m + 18M_T(T_{N-1}^m)dx^2}{11}, \\ u_{N-2}^m = \dfrac{28u_{N-3}^m - 23u_{N-4}^m + 6u_{N-5}^m + 4M_T(T_{N-1}^m)dx^2}{11}, \\ u_i^0 = g(x_i), \\ u_i^1 = u_i^0, \end{cases} \tag{2.28}$$

in which we have used as well the temporal derivatives with accuracy $O(dt^2)$, and all the spatial derivatives except $\partial u(0,t)/\partial x$ with accuracy $O(dx^3)$. Indeed, while for the

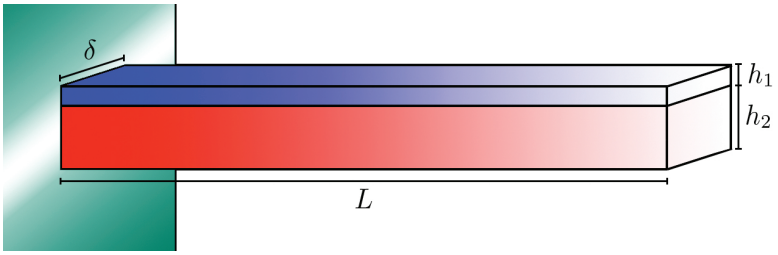

Figure 2.4: Geometry of the beam: we label with δ its depth, L its length, h_1 and h_2 the thickness of the first and second layer, respectively.

conditions on the right side of the slab ($i = N-1, N-2$) we were able to use a second-order development, coherent with the finite-difference description employed in Eq. (2.20), on the left side it was mandatory to use a first-order development of the condition $\partial u(0,t)/\partial x$ in order to have a starting point to determine the entire displacement profile at a given time.

2.5 Thermomechanical bistability

Now we can investigate the dynamical evolution of our system. In order to demonstrate the existence of two equilibrium solutions we investigate the spatio-temporal evolution of displacement and temperature profiles [50]. Since we are working with VO_2, it is clear that in order to get easily two equilibrium solutions for the beam, all the temperatures involved in the evolution must be close to the critical temperature T_c of the MIT material. Moreover to get a transition of MIT material, the temperatures of substrate T_s, wall T_w and thermal bath T_e must not be all above or below T_c.

Concerning the geometric parameters for the beam, they are chosen to reduce as much as possible the relaxation time of the system. In the following we use (see Fig. 2.4): depth $\delta = 1\,\mu$m, length $L = 360\,\mu$m, $h_1 = 90\,$nm for the VO_2 layer, $h_2 = 910\,$nm for the SiO_2 layer. The length of the SiO_2 substrate is $l = 30\,\mu$m, and it is placed at distance $d_0 = 250\,$nm from the x-axis to ensure a relative balance between the magnitude of heat flux exchanged in far and near field, as sketched in Fig. 2.2. The parameters we use for SiO_2 are $E_2 = 68\,$GPa, $C_2 = 730\,\mathrm{J}\cdot\mathrm{K}^{-1}\cdot\mathrm{kg}^{-1}$, $\rho_2 = 2650\,\mathrm{kg}\cdot\mathrm{m}^{-3}$, $\alpha_2 = 8\cdot10^{-6}\cdot\mathrm{K}^{-1}$, and the optical data given in Ref. [61]. For VO_2, we take $C_1 = 344\,\mathrm{J}\cdot\mathrm{K}^{-1}\cdot\mathrm{kg}^{-1}$, $\rho_1 = 4570\,\mathrm{kg}\cdot\mathrm{m}^{-3}$ and $E_1 = 85\,$GPa since they do not vary significantly with the phase [90]. In order to describe the temperature dependence of the physical properties of VO_2 around T_c we use the smoothing function

$$S(T, T_c, \beta) = \frac{1}{1 - e^{-2\beta(T-T_c)}}, \tag{2.29}$$

where β is a parameter allowing to adjust the smoothness in the transition region between the dielectric and the metallic phases. This smoothing function is consistent with the percolation mechanism observed experimentally in VO_2 [91]. In terms of this function, the physical quantity a_1 around the critical temperature Tc is given by

$$a_1(T) = a_{1d} + S(T, T_c, \beta)(a_{1m} - a_{1d}), \tag{2.30}$$

where a_{1d} and a_{1m} are the properties in the dielectric and metallic phase, respectively. We use this expression to model the thermal expansion coefficients α_1, the thermal conductivity κ_1 and the emissivity ϵ_1. For film thicknesses of few dozens of nm the transition between the dielectric and the metallic regime generally occurs over a temperature interval of few degrees. Indeed, we assume here a range of approximately 10 degrees which corresponds to the value $\beta = 0.5\,\mathrm{K}^{-1}$. Concerning the physical quantities associated with VO_2, we use the data from Refs. [67, 91]: $\alpha_{1_d} = 26.4 \times 10^{-6}\,\mathrm{K}^{-1}$, $\kappa_{1_d} = 3.6\,\mathrm{W\,m^{-1}\,K^{-1}}$, $\epsilon_{1_d} = 0.8$ in the dielectric phase and $\alpha_{1_m} = 17.1 \times 10^{-6}\,\mathrm{K}^{-1}$, $\kappa_{1_m} = 3.6\,\mathrm{W\,m^{-1}\,K^{-1}}$, $\epsilon_{1_m} = 0.1$ in the metallic phase.

Finally, the damping factor γ is defined in terms of the oscillator quality factor Q as [92]

$$\gamma = 3.52\, Q^{-1} L^{-2} \sqrt{EI\mu}. \tag{2.31}$$

It depends on the surrounding environment and on the first natural frequency of the cantilever. For a cantilever embedded in air and in vacuum the quality factors are $Q \approx 100$ and $Q \approx 50000$ [92], respectively.

In Fig. 2.5 we show the time evolution of $T(L,t)$ and $u(L,t)$ for the temperature set $\{T_e, T_w, T_s\} = \{300, 356, 353\}$ K, with the initial conditions

$$u(x,0) = g(x) = 135\,\mathrm{m}^{-1}x^2, \quad \text{and} \quad T(x,0) = f(x) = \lambda x^2 - 2\lambda L x + T_w, \tag{2.32}$$

where λ is an adjustable parameter. Since the expansion coefficient of VO_2 is always larger than the SiO_2 one, and all the temperatures we are considering are equal or larger than the cantilever bulding temperature T_0, the bending will be always toward the silica substrate. As a consequence, the choice of the initial cantilever displacement $u(x,0)$ is made to accelerate numerical convergence. Concerning the initial temperature profile, it is worth noticing that $f(x)$ satisfies the boundary conditions for any value of the parameter λ.

In Fig. 2.5 we show, by choosing two different values of λ, the temporal evolution in vacuum and air of displacement and temperature of the free end of the beam $T(t,L)$. Indeed, by choosing two different initial profiles with $\lambda = -0.1 \times 10^8\,\mathrm{K\cdot m^{-2}}$ (blue curves) and $\lambda = 3 \times 10^8\,\mathrm{K\cdot m^{-2}}$ (red curves), respectively, the system evolves to two distinct stable solutions both for displacement and temperature, thus demonstrating its thermomechanical bistability in vacuum and in air [50].

Concerning the temperature, since the surrounding medium only affects the oscillator damping and does not modify its asymptotic behavior, the steady-state solutions are

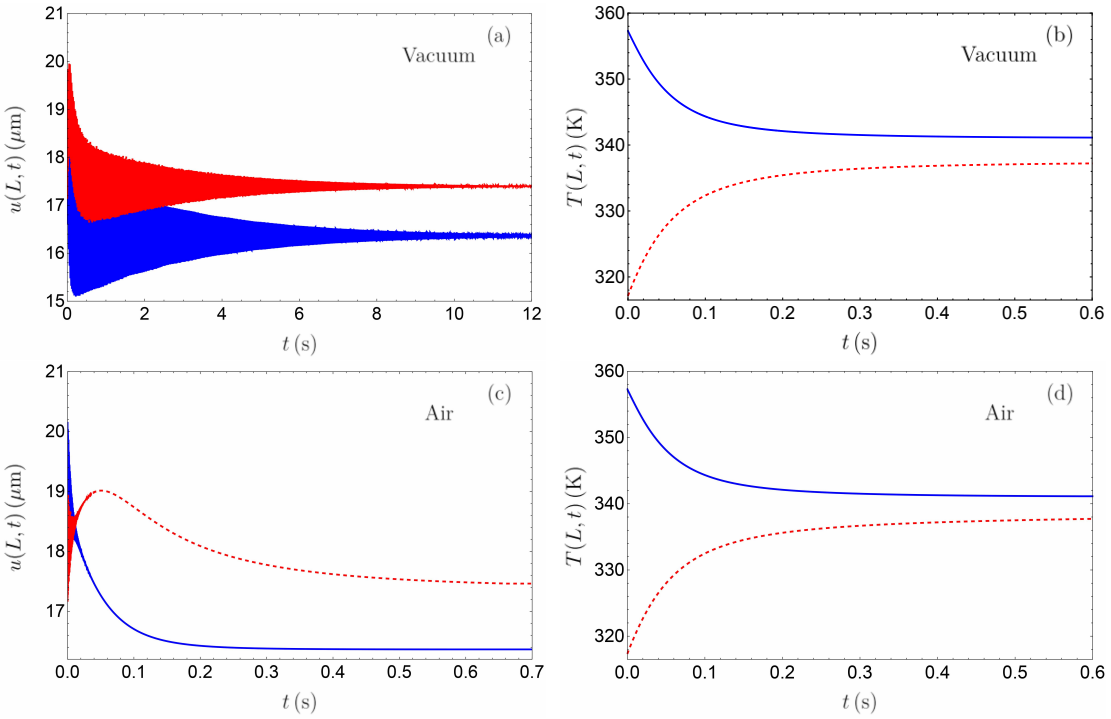

Figure 2.5: Time evolution of the **(a)**-**(c)** displacement and **(b)**-**(d)** temperature of the free end of the cantilever in the case of vacuum and air as surrounding medium. The red-dashed curves are the lower-temperature solutions obtained for $\lambda = -0.1 \cdot 10^8\,\mathrm{K\,m^{-2}}$, the blue-solid curves the upper-temperature solutions obtained for $\lambda = 3 \cdot 10^8\,\mathrm{K\,m^{-2}}$.

the same in vacuum and in air. Moreover, we observe that the steady state is reached after almost the same time interval ($\tau_\infty \approx 0.5\,\mathrm{s}$) in both cases. This time is in agreement with the decay timescale $\tau_c = \rho C L^2/\kappa \approx 0.14\,\mathrm{s}$ which can be extracted from a simple dimensional analysis of the energy-balance equation.

The behavior of the displacement $u(L,t)$ [Fig. 2.5(a)-(c)] is more peculiar and, contrarily to the temperature evolution, it clearly depends on the surrounding medium. Although the time needed both in air and in vacuum to reach the asymptotic regime is still τ_∞, the displacement oscillates differently in vacuum and in air. As shown in Fig. 2.6(a) where a zoom of the first $3 \cdot 10^{-4}\,\mathrm{s}$ of the displacement time evolution is shown, we clearly observe two distinct oscillation frequencies. We have numerically verified that these correspond to the first and third natural frequencies of the cantilever, $\omega_1 = 3.52\,L^{-2}\sqrt{EI/\mu}$ and $\omega_3 = 61.7\,L^{-2}\sqrt{EI/\mu}$. Since the decay time τ_{ω_i} of these oscillations is proportional to the quality factor ($\tau_{\omega_i} = 2Q/\omega_i$) the longest decay timescales in air and vacuum are, respectively, $\tau_{\omega_1}^{\mathrm{air}} = 5.1 \cdot 10^{-3}\,\mathrm{s}$, and $\tau_{\omega_1}^{\mathrm{vacuum}} = 2.5\,\mathrm{s}$. As expected, the damping of the oscillations is stronger in air than in vacuum.

We now investigate how the choice of the adjustable parameter λ influences the

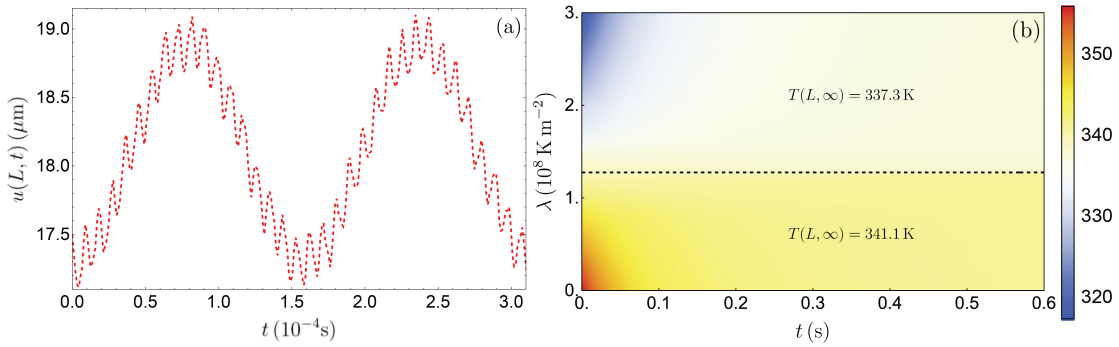

Figure 2.6: **(a)** Time evolution of $u(L,t)$ in air over a shorter timescale. **(b)** Time evolution of $T(L,t)$ as a function of the parameter λ associated with the initial temperature profile, the black dashed line corresponds to the threshold value $\lambda_{\text{thr}} = 1.275 \cdot 10^8$ K·m^{-2}.

equilibrium solution. To this aim, in Fig. 2.6(b) we explore a wide range for λ, obtaining two stationary solutions for $T(L,t)$ [then for $u(L,t)$] and deducing the threshold value to switch from one stable solution to another, i.e. $\lambda_{\text{thr}} = 1.275 \cdot 10^8$ K·m^{-2}. Concerning

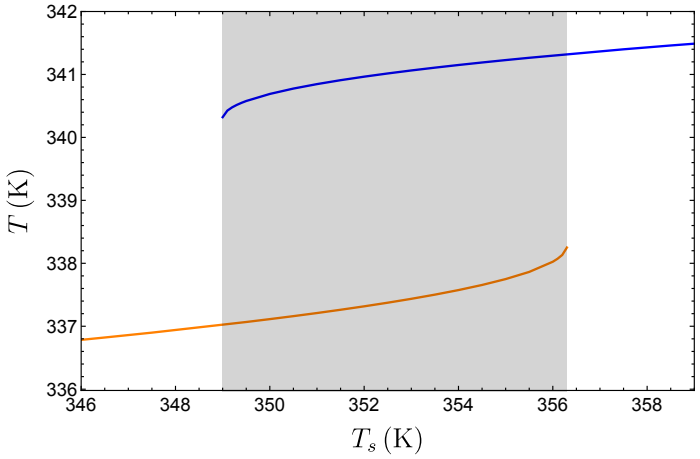

Figure 2.7: Equilibrium temperature as function of the substrate temperature T_s. The blue (orange) branch represents the upper (lower) solution. The gray zone highlights the range where $T_s \in [346; 356.3]$ for which two equilibrium solutions exist.

the region of existence of the bistability, we identify the range of substrate temperatures over which the bistability is present. To this aim, we perform numerical calculations keeping all the parameters, except T_s, unchanged. The steady solutions for $T(L)$ are represented by the blue and orange solid lines in Fig. 2.7. We clearly see that, when T_s lies in the range $[349, 356.3]$ K [gray zone in Fig. 2.7], we observe a bistable behavior, while for values of T_s outside this range we only get one stable solution.

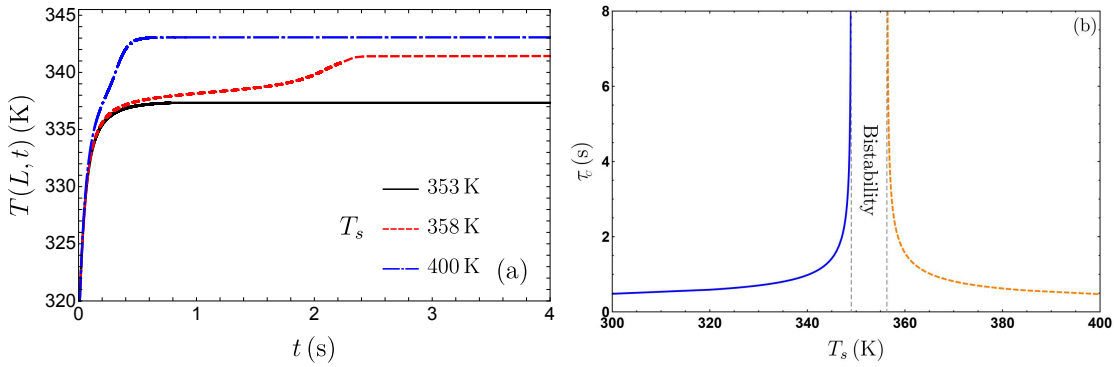

Figure 2.8: **(a)** Time evolution of $T(L)$ for constant T_s equal to 353 K (black solid), 358 K (red dashed) and 400 K (blue dot-dashed). **(b)** Decay timescale τ_c as a function of the substrate temperature T_s outside of the bistable region. The curve in blue (orange) represents the decay time of the upper (lower) solutions.

It is then interesting to study the behavior of $T(L,t)$ when we are within, slightly above and far beyond the bistability region. Indeed, in Fig. 2.8(a) we show the temporal evolution of the dielectric (lower) starting temperature profile [$\lambda = 3 \times 10^8\,\mathrm{K\,m^{-2}}$] for different substrate temperatures, i.e. $T_s = 353, 358, 400\,\mathrm{K}$. For $T_s = 353\,\mathrm{K}$ ($T_s = 400\,\mathrm{K}$) we observe the expected convergence to the lower (upper) solution on a timescale $\approx \tau_c$. On the contrary, we demonstrate the presence of an unstable solution for $T = 358\,\mathrm{K}$, slightly larger than $356.3\,\mathrm{K}$, the upper boundary of the bistability region. In this scenario, an initial plateau (up to 1.5 s) with a temperature lower than $340\,\mathrm{K}$ is followed by the convergence toward the final steady-state temperature above 340 K. This is a signature of the fact that T_s is still close to the region where two solutions exist, and is analogous to the saddle-point behavior already observed in Ref. [45].

To complete this analysis, it is useful to investigate how the decay time needed to converge to the steady-state solution changes when we approach the bistable zone, both from higher and lower temperatures. To this aim, in Fig. 2.8(b) we show the decay time as a function of the substrate temperature T_s. For $T_s > 356.3\,\mathrm{K}$ we plot only the time scale associated with the lower solution: as a matter of fact, this solution will behave as the red dashed curve in Fig. 2.8(a) (with an intermediate plateau and then a larger τ_c), while we are sure that the upper (metallic) solution will directly converge to a stable solution within the expected decay time of the order of $0.5\,\mathrm{s}$. By approaching $T_s = 356.3\,\mathrm{K}$ from above, we observe in Fig. 2.8(b) a dramatic amplification (a vertical asymptote) of τ_c, implying that, for these temperatures, the intermediate temperature profile can be seen (depending on the timescale of interest) as a metastable solution. The description is fully analogous for the region $T_s < 349\,\mathrm{K}$, with the same divergence behavior of τ_c.

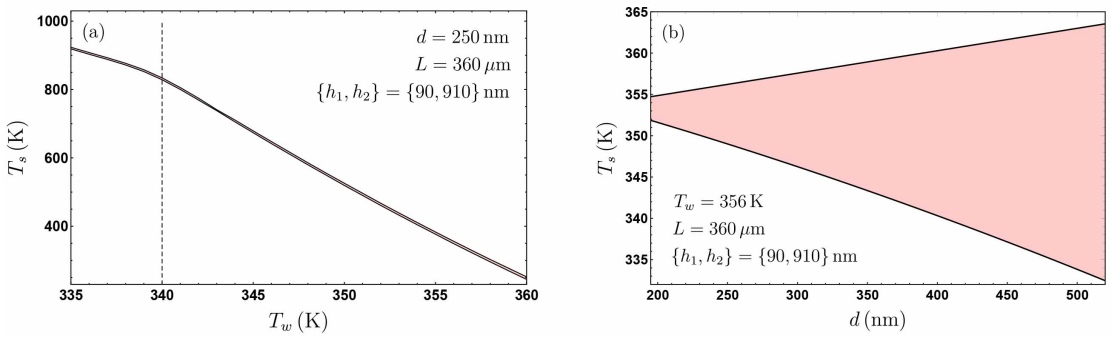

Figure 2.9: (a) Dependence of the bistability on the temperatures T_w and T_s, of the wall and substrate, respectively. The vertical dashed line corresponds to the transition temperature of VO_2. The red area denotes the region where bistability is present. **(b)** Dependence of the bistability on the substrate temperature T_s and on the distance d between cantilever and substrate. The red area denotes the region where bistability is present.

Bistability range as a function of the parameters

We now focus on the study of the existence of the thermomechanical bistability as a function of the substrate temperature and the several geometric parameters involved, namely the thicknesses h_1 and h_2 of the VO_2 and SiO_2 layers, respectively, the length L of the cantilever, and the distance d between cantilever and the silica substrate.

To this aim we start from the configuration studied in the previous section, having parameters $\{T_e, T_w, T_s\} = \{300, 356, 353\}$ K, $L = 360\,\mu$m, $h_1 = 90$ nm for the VO_2 layer, $h_2 = 910$ nm for the SiO_2 layer, and $l = 30\,\mu$m, placed at distance $d_0 = 250$ nm from the x axis, and let some of them vary from this reference configuration. In Fig. 2.9(a) we show the dependence of the bistability effect on the two temperatures T_s and T_w. The part of the plot highlighted in red represents the values of the parameters for which thermomechanical bistability exists. We immediately remark that the existence of bistability is indeed very sensitive to the wall temperature T_w. This is not surprising, since this temperature strongly influences, through conduction, the temperature profile along the beam. Nevertheless, we observe that by varying the substrate temperature T_s in the range studied here, we are always able to identify a range of T_w where bistability is present. We also clearly remark that the values of T_w for which the system is bistable have a dependence on T_s close to linear, with a slope which changes around 340 K, namely the transition temperature of VO_2.

In Fig. 2.9(b) we investigate the dependence of the bistability on the substrate temperature T_s and the distance d. We clearly see that the range of temperatures T_s over which bistability exists can be tailored by modifying the distance d, even in the near-field regime. As an example, we observe that, while the width of this interval of T_s is

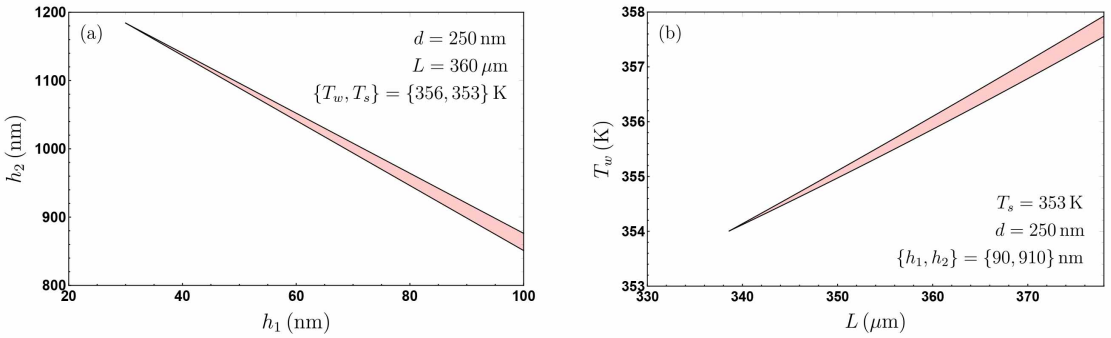

Figure 2.10: (a) Dependence of the bistability effect on the thicknesses h_1 and h_2, of the VO_2 and SiO_2 layers, respectively. The red area denotes the region where bistability is present, bounded by the black lines. **(b)** Dependence of the bistability effect on the length L of the cantilever and on the temperature T_w of the wall. The red area denotes the region where bistability is present.

close to 7 K for the distance $d = 250$ nm used in the main part of the chapter, it goes up to more than 30 K when $d = 500$ nm.

We now address the dependence of bistability on two relevant geometrical parameters, namely the thicknesses h_1 and h_2 of the VO_2 and SiO_2 layers, respectively. The results, presented in Fig. 2.10(a), show that bistability does not exist below a given value of h_1, around 30 nm. Moreover, as the thickness h_1 increases, the range of h_2 over which bistability is possible increases as well. These results are coherent with the fact that the phase-change behavior of VO_2 is crucial to obtain two stable solutions.

In Fig. 2.10(b) we finally show the dependence of bistability on the temperature of the wall T_w and on the length L of the cantilever. We observe that is not possible to find any value of T_w for which a bistability behavior exist below a value of L around 338 μm. Below this value, conduction works too well along the cantilever and then it does not allow the presence of two stable temperature profiles crossing the critical temperature $T_c = 340$ K of VO_2.

2.6 Hysteretic behavior in the time evolution of temperature profiles

We now explore the possibility to use bistability to produce a hysteretic behavior with respect to an external control parameter. The natural parameters to be exploited to this aim are the substrate temperature T_s or the wall temperature T_w, which can be tuned using for instance Peltier elements or external laser sources. Here we consider only T_s

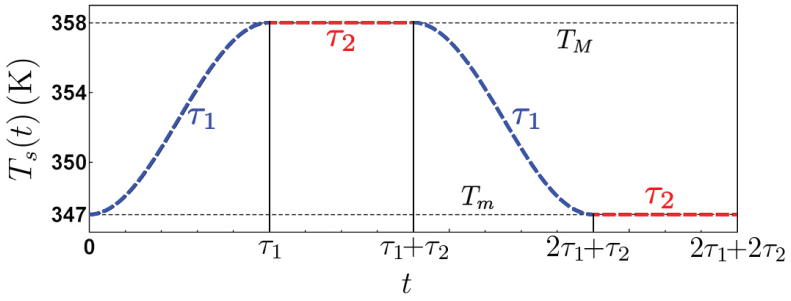

Figure 2.11: Temporal modulation of the substrate temperature T_s. In blue we highlight the time-scale τ_1 in which T_s rises up (goes down) to the maximum (minimum) value of $T_M = 358\,\mathrm{K}$ ($T_m = 347\,\mathrm{K}$), while in red the time-scale τ_2 in which T_s remains at the maximum (minimum) value of $T_M = 358\,\mathrm{K}$ ($T_m = 347\,\mathrm{K}$).

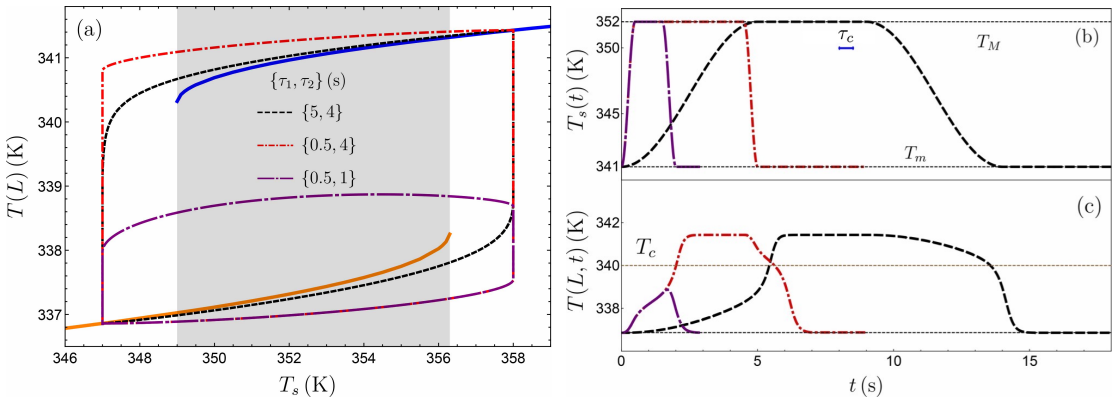

Figure 2.12: **(a)** Phase diagram of the time-dependent temperature $T(L,t)$ of the free end of the cantilever as a function of the substrate temperature $T_s(t)$. The three different curves correspond to different profiles of $T_s(t)$ (see legend). The blue and orange solid curves correspond the steady-state solutions for $T(L)$ associated with each value of T_s. **(b)** Imposed time dependence of the substrate temperature T_s (see text for functional dependence). The blue segment represents the decay timescale τ_c. **(c)** Time evolution of $T(L)$ as a function of time [same color scheme as in panel **(a)**]. The horizontal brown dashed line represents the critical temperature T_c.

as a control parameter.

As suggested by the curves plotted in Fig. 2.7, a time variation of T_s allows to switch from one stable solution to the other one through a hysteresis loop. Of course, this possibility strongly depends on the specific time dependence of T_s, and in particular on the comparison between the typical timescale over which T_s is tuned and the relaxation time τ_c of our system. To get a deeper insight into this aspect, we let T_s vary according to the time-dependent function represented in Fig. 2.11. We start from a minimum

temperature $T_m = 347\,\mathrm{K}$ and from $t = 0\,\mathrm{s}$ to $t = \tau_1$ we increase the value of T_s up to its maximum $T_M = 358\,\mathrm{K}$ through the growing branch of the function

$$F(t) = (T_M - T_m)\frac{1 - \cos(\pi\, t/\tau_1)}{2}. \tag{2.33}$$

We then keep $T_s = T_M$ during a time interval τ_2 to finally go down to T_m over a time interval τ_1 through the descending branch of the function

$$G(t) = (T_M - T_m)\frac{1 - \cos[\pi(t - \tau_2)/\tau_1]}{2}. \tag{2.34}$$

In Fig. 2.12(c) we describe the evolution of $T(L)$ as a function of T_s when this one is modulated at different timescales. We perform the simulations for three different couples of timescales, namely $\{\tau_1, \tau_2\} = \{0.5\,\mathrm{s}, 1\,\mathrm{s}\}, \{0.5\,\mathrm{s}, 4\,\mathrm{s}\}, \{5\,\mathrm{s}, 4\,\mathrm{s}\}$ [see Fig. 2.12(b)]. Let us start from the case with the smallest values for both the timescales, i.e. $\{\tau_1, \tau_2\} = \{0.5\,\mathrm{s}, 1\,\mathrm{s}\}$ [violet long-dot-dashed curves in Fig. 2.12]. Figure 2.12(a)-(c) clearly chows that these values do not allow to perform the transition from the lower to the upper branches of stable solutions. More specifically, τ_2 is much smaller than the relaxation time τ_c of the system, which means that when the period of modulation is smaller than the time of thermal relaxation of the cantilever, the latter is not sufficiently heated up to transit into its metallic phase. To confirm this interpretation, we observe that, following the evolution of the red curve [$\{\tau_1, \tau_2\} = \{0.5\,\mathrm{s}, 4\,\mathrm{s}\}$] which has the same τ_1 but larger τ_2 with respect to the previous, the system is able to switch from the dielectric to the metallic solutions and viceversa, creating a hysteresis between the stable solutions. Finally, we consider the last couple of timescales $\{\tau_1, \tau_2\} = \{5\,\mathrm{s}, 4\,\mathrm{s}\}$. Following the dashed black curves in Fig. 2.12(a) we can see that with a larger τ_1 the curve follows adiabatically the solution branches.

It is worth noticing that, as shown in Fig. 2.12(c), the temperature of the free end of the beam $T(L, t)$ goes beyond the VO_2 critical temperature only when the transition between the lower states is effectively performed [red and black curves]. The two stable solutions plotted in Fig. 2.12(a) correspond to a net heat flux which is locally convex in the $(T_s, T(L))$ plane.

Cantilever as a thermal memory and a logic gate

A direct application of this thermomechanical bistability is the design of a thermal memory or a logic gate. It is direct to see from a simple inspection of Fig. 2.11 that the thermal state of cantilever can be associated with a “0" and “1" state, after appropriate threshold temperatures have been defined. These states can be maintained as long as no external perturbations induce a switch from one state to the other one. It is also straightforward to see that such a system can be used to perform basic logic operations.

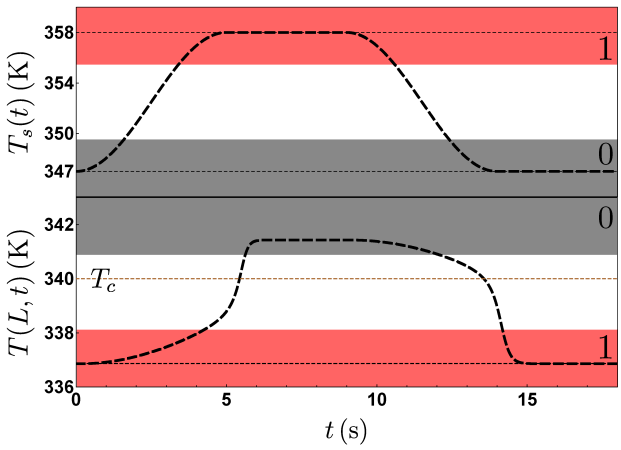

INPUT	OUTPUT
A	**NOT A**
T_s	$T(L)$
0	1
1	0

Figure 2.13: **(a)** Graphical representation of the NOT logic gate exploiting the time modulation of the substrate temperature T_s and the response of the free-end temperature of the cantilever $T(L,t)$. **(b)** Table of truth for a NOT logic gate for the bistable cantilever system.

More specifically, it can be exploited as a NOT gate identifying the control parameter T_s as the input of the gate and $T(L)$ as its boolean output. If we define the thermal states by defining appropriate threshold temperatures we can label as thermal state '0' the state where T_s is close to T_m and as thermal state '1' as the state where T_s is close to T_M, analogously two states '1' and '0' when $T(L) < T_c$ (larger bending) and $T(L) > T_c$ (smaller bending) can be defined [See Fig. 2.13(a)]. Comparing our system to the table of truth in Fig. 2.13(b) we can deduce that the cantilever behaves like a NOT gate. In fact, when T_s lies in its '0' state, $T(L)$ lies in its '1', and viceversa [50]. The coupling of such oscillators and their control with multiple input parameters could allow to define more complex logical operations and thus to exploit potential waste heat generated in macro or nano-size devices. With this respect, one should bear in mind that the main factor limiting the use of this system is represented by its thermal inertia, indeed the time needed to perform a logic operation by means of this cantilever is much larger that the standard electronic counterpart.

2.7 Conclusions

In this chapter we have investigated the dynamical behavior of micro-sized phase-transition cantilevers and demonstrated the possibility to perform information treatment with these devices. In such a thermomechanical oscillator, we have demonstrated that, out of thermal equilibrium, the temperature and the displacement associated with the

beam may admit two stable solutions. We have shown that their profiles can be driven by external heat flux and switched from one stable state to another. In the first section of this chapter we reminded the general case of a many-body thermal system and we discussed how such a system may admit more than one equilibrium (steady-state) temperature distribution. Moreover, we discussed how this feature can be exploited in order to process information. In Sec. 2.2 we introduced the Euler-Bernoulli momentum conservation equation, governing the dynamics of a beam. We first focused on the case of a cantilever and obtained its normal modes. In Sec. 2.3 we studied more in detail the physics of a bimaterial cantilever, introducing its effective quantities and the bending thermal moment due to the mismatch between the thermal expansion coefficients of its two layers. In Sec. 2.4 we described our system consisting of a phase-change bimaterial cantilever and we numerically solved the coupled differential system composed of the Euler-Bernoulli and energy-balance equations, highlighting a thermomechanical bistable behavior. In the last section, we finally discussed the potential of these systems to make a basic logical operator, exploiting the bimaterial phase-change cantilever as a thermal memory and a NOT logic gate.

Several questions remain open and will have to be explored at a fundamental level. One of them is the thermal preparation of oscillators which plays a crucial role in the dynamic evolution of the system. Another important perspective is the coupling of the system with other oscillators in order to perform more complex logical operations.

Chapter 3

Conduction-radiation coupling between two closely separated solids

Usually, the net radiative power exchanged in near field between two solids, separated by a gap and held at uniform temperatures, is calculated using the PvH theory. This theory neglects the coupling with other modes of transfer. Hence, it is assumed that phonon transport is perfectly efficient within the two bodies, implying that they uniformly thermalize at each time instant. In other words, no conduction-radiation coupling between the solids is taken into account. Nevertheless, in reality, thermal photons are absorbed within the volume of each body and they dissipate their energy unevenly through them. As a consequence, the temperature profiles within each body are generally not uniform and their spatio-temporal variation is driven by the conduction-radiation coupling mechanism. A first attempt to describe this coupling has been proposed in 2016 [49], but this phenomenological approach was limited to bodies of characteristic length much larger than the mean free path of heat carriers, so that no ballistic or partially ballistic transport could be taken into account. In this chapter we introduce a general theoretical framework to describe the heat transfer between two slabs of arbitrary size, by taking into account the interplay between conduction and radiation. We limit our study to systems in the thermodynamic limit where the temperature is uniquely defined even at local scale and where the local thermal equilibrium is reached. Moreover, we consider only slabs with thicknesses much larger than unit cell of the crystalline structure of materials, so that their dielectric permittivity [61] can be assumed to be size-independent. The essence of this approach is based on the combination of Boltzmann's equation to deal with the heat carriers inside the solids for any heat-transport regime, and fluctuational electrodynamics to calculate the radiative power that is locally dissipated within each body.

In the first section of this chapter we identify the different heat-transport regimes through the definition of an adimensional number, the Knudsen number, while in Sec. 2 we discuss the Boltzmann Transport equation and the fundamental relaxation time ap-

proximation. In Sec. 3 we describe the physical system we will study and write the equations which drive the steady-state temperature profile. Then we describe the numerical method used to solve these equations. In Sec. 4 we introduce and describe the conduction properties of 3C-SiC, in order to use this material as main component of our slabs and we also introduce the Callaway method used to obtain the relaxation time of this material. Finally, in Sec. 5 we analyze the equilibrium temperature profile obtained through our numerical simulation and we compare the heat flux calculated using our theoretical framework to the standard flux obtained using the PvH theory.

3.1 Description of phononic heat transport: ballistic and diffusive regimes

In order to characterize the regime of conductive heat transport mediated by phonons within a sample we introduce the Knudsen number, Kn, defined as follows

$$\mathrm{Kn} = \frac{\Lambda}{L} = \frac{v_g \tau}{L}, \tag{3.1}$$

where Λ denotes the mean free path of phonons, that is the average distance traveled by a phonon between two successive scattering events, L the characteristic length of the sample across which heat transport is considered, v_g the modulus of the group velocity of phonons and τ the relaxation time, also known as scattering time scale. When $\Lambda \gg L$ the scattering events are rare and the phonons can travel between the sample boundaries without scattering. This regime is the so-called "ballistic transport". In this case $\mathrm{Kn} \gg 1$. On the contrary, when $\Lambda \ll L$ and therefore $\mathrm{Kn} \ll 1$ the transport regime is "diffusive". Indeed, in this case, the mean free path Λ is much smaller than the characteristic length of the sample L and phonons scattering events are very frequent along their trajectory. In this regime, the Fourier's law describes the heat transport inside the sample. As a consequence of these two fundamentally different regimes, the corresponding equilibrium temperature profiles present radically different features. To illustrate this, we consider here the simple case of a single slab in perfect contact (i.e. without thermal resistance) at both edges with two thermostats at temperatures T_1 for the left boundary and T_2 for the right one. In the ballistic regime the temperature profile is constant through the slab but undergoes two discontinuities at the boundaries. Actually, since no collision events take place between the boundaries, the energy density remains roughly constant and the temperature as well. Its value can be derived from the continuity of flux. In the blackbody limit, this temperature, also called the Casimir temperature is $\sqrt[4]{(T_1^4 + T_2^4)/2}$ [93](see Fig. 3.1). In the diffusive regime the temperature profiles becomes a straight line, solution of the Fourier's law. Of course, between these two regimes, a transition one (see Fig. 3.2) exists. In this case, the equilibrium temperature profile is intermediate between the constant and the linear profile. It still presents

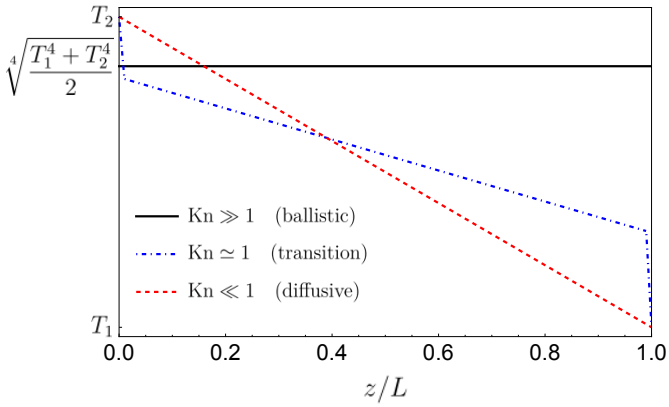

Figure 3.1: Equilibrium temperature profile for slabs of different thicknesses in perfect contact with two thermostats at temperature T_1 and T_2.

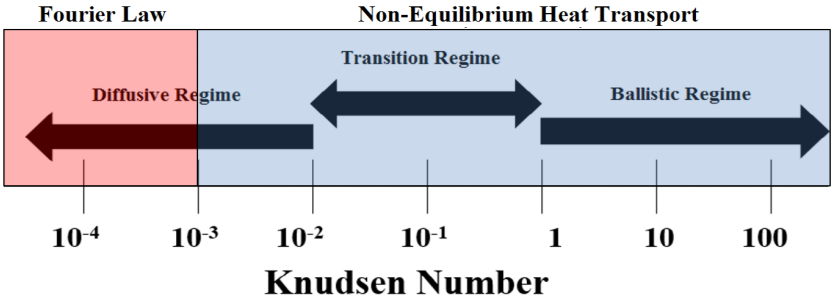

Figure 3.2: Regimes of heat transport as a function of Knudsen Number.

the discontinuities at the interfaces but the jumps become less and less pronounced as the size increases.

3.2 The Boltzmann Transport Equation

One of the methods to describe the non-equilibrium heat transport of heat carries is based on the semiclassical Boltzmann Transport Equation (BTE). This equation can be used to model conduction phenomenon by phonons in solids can be provided that the quantum wave effects (coherence) can be neglected. In order to solve the BTE associated with phonons we introduce the distribution function $f(t, \mathbf{r}, \mathbf{p})$, coming from classical kinetic theory, such that $f(t, \mathbf{r}, \mathbf{p}) d^3\mathbf{r} d^3\mathbf{p}$ is the number of phonons at time t having coordinate in a volume of the $(\mathbf{r}, \mathbf{p})$ phase space $d^3\mathbf{r} d^3\mathbf{p}$ around $\mathbf{r}$ and $\mathbf{p}$. The time evolution of this distribution function can be obtained by calculating its derivative

df/dt. Using the decomposition in partial derivatives, we get

$$\frac{df}{dt} \equiv \frac{\partial f}{\partial t} + \frac{d\mathbf{r}}{dt} \cdot \boldsymbol{\nabla}_{\mathbf{r}} f + \frac{d\mathbf{p}}{dt} \cdot \boldsymbol{\nabla}_{\mathbf{p}} f \tag{3.2}$$

where

$$\boldsymbol{\nabla}_{\mathbf{r}} f = \frac{\partial f}{\partial x}\hat{\mathbf{x}} + \frac{\partial f}{\partial y}\hat{\mathbf{y}} + \frac{\partial f}{\partial z}\hat{\mathbf{z}}, \tag{3.3}$$

$$\boldsymbol{\nabla}_{\mathbf{p}} f = \frac{\partial f}{\partial p_x}\hat{\mathbf{p}}_x + \frac{\partial f}{\partial p_y}\hat{\mathbf{p}}_y + \frac{\partial f}{\partial p_z}\hat{\mathbf{p}}_z. \tag{3.4}$$

These changes along the phonons trajectory are due to all collision events they undergo. Hence, we identify the time variation of the distribution function to changes due to these scattering events. Then

$$\frac{\partial f}{\partial t} + \frac{d\mathbf{r}}{dt} \cdot \boldsymbol{\nabla}_{\mathbf{r}} f + \frac{d\mathbf{p}}{dt} \cdot \boldsymbol{\nabla}_{\mathbf{p}} f = \left(\frac{\partial f}{\partial t}\right)_c \tag{3.5}$$

where $(\partial f/\partial t)_c$ denotes the time variation of f in the phase space due to these scattering events. Eq. (3.5) is known as Boltzmann Transport Equation. We can also rewrite the BTE as a function of the phonon group velocity $\mathbf{v}_g$ and in terms of wavevector $\mathbf{k}$, using the relations $\mathbf{v}_g = d\mathbf{r}/dt$ (for isotropic medium) and $\mathbf{p} = \hbar\mathbf{k}$, obtaining

$$\frac{\partial f}{\partial t} + \mathbf{v}_g \cdot \boldsymbol{\nabla}_{\mathbf{r}} f + \frac{\mathbf{F}}{\hbar} \cdot \boldsymbol{\nabla}_{\mathbf{k}} f = \left(\frac{\partial f}{\partial t}\right)_c, \tag{3.6}$$

where $\mathbf{F} = d\mathbf{p}/d\mathbf{r}$ is the external force acting on the particle. Since this equation is generally complicated to solve, mainly because of the complexity of the collision term, it has been shown [94] that to deal with conduction it is sufficient to limit to the well known relaxation-time approximation. In this case the colliding term reduces to

$$\left(\frac{\partial f}{\partial t}\right)_c = -\frac{f - f_0}{\tau(\mathbf{r}, \mathbf{k})}, \tag{3.7}$$

where $\tau(\mathbf{r}, \mathbf{k})$ is the relaxation time, while f_0 is the equilibrium distribution of the carriers (Bose-Einstein in the case of phonons). This approximation is valid only in the case of elastic scattering. Despite that, this approximation is widely used even in the case of inelastic scattering [94]. In order to illustrate the physical meaning of relaxation time we consider an example in which we neglect the spatial non-uniformity of the distribution function. In this case, Eq. (3.7) becomes

$$\frac{\partial f}{\partial t} = -\frac{f - f_0}{\tau}, \tag{3.8}$$

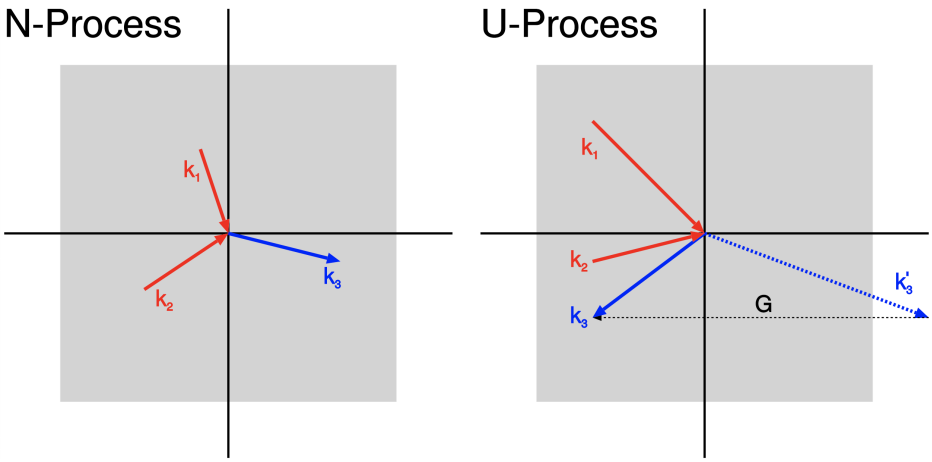

Figure 3.3: Normal process (N-process) and Umklapp process (U-process). While the N-process conserves the phonon momentum, the U-process changes phonon momentum.

whose solution is

$$f - f_0 = Ce^{-t/\tau}. \tag{3.9}$$

Hence, we see that the time τ is a measure of how long the phonon takes, from a non equilibrium system, to relax back to equilibrium, thanks to colliding events. This time τ can be calculated using the Matthiessen rule [94], i.e.

$$\tau^{-1} = \sum_j \tau_j^{-1}, \tag{3.10}$$

where τ_j is the time associated with a specific scattering mechanism and the sum is made over all of them. In order to use the Matthiessen's rule we have to assume that all these mechanisms are independent. In the relaxation time approximation, the BTE reads

$$\frac{\partial f}{\partial t} + \mathbf{v} \cdot \boldsymbol{\nabla}_{\mathbf{r}} f + \frac{\mathbf{F}}{\hbar} \cdot \boldsymbol{\nabla}_{\mathbf{k}} f = -\frac{f - f_0}{\tau}. \tag{3.11}$$

Scattering mechanisms of phonons

A main part of the phonon scattering is generally due to the scattering of phonons between themselves. Among the colliding events involving three phonons, these collisions often cause a merging of two phonons into a third, or a splitting of a single phonon into two phonons. The three phonons-scattering process can be either *normal* (N-process) or *Umklapp* (U-process) as shown in Fig. 3.3. For the N-process the third phonon generated by the collision conserves both the energy and the direction of the two original phonons, which means

$$\mathbf{k_1} + \mathbf{k_2} - \mathbf{k_3} = 0. \tag{3.12}$$

Hence, in the reciprocal lattice, the $\mathbf{k_3}$ wavevector lies in the first Brillouin zone. The relaxation time due to N-process can be modelized as follows [95, 96]

$$\tau_n^{-1} = C\omega T^4, \tag{3.13}$$

where C is a constant that depends on the material. In the umklapp process, thanks to the presence of an extra reciprocal lattice wavevector, the net direction of phonon propagation changes creating resistance to the heat flow, i.e.

$$\mathbf{k_1} + \mathbf{k_2} - \mathbf{k_3} = G, \text{ with } G \neq 0. \tag{3.14}$$

As a consequence, in this latter case, the wavevector $\mathbf{k}_3$ points outside the first Brillouin zone. Without the contribution of the umklapp process and anharmonics process, the thermal conductivity of a crystal would remain infinite. An approximate expression of the relaxation time, based on the umklapp process has been derived by Klemens [95] and depends on the frequency ω as

$$\tau_u^{-1} = Be^{-T_D/bT}T^3\omega^2. \tag{3.15}$$

Here B and b are constants which depend on the material, while T_D is the Debye temperature. In general, if resistive processes dominate, the normal relaxation time can be disregarded [96]. Since the umklapp scattering is proportional to ω^2 it thus dominates over the normal processes, which depend linearly on frequency.

Another scattering mechanism for phonons is due to the presence of defects inside crystal [95, 97]. The relaxation time related to this kind of scattering process obeys the Rayleigh law

$$\tau_I^{-1} = A\omega^4, \tag{3.16}$$

where A is a constant depending on the material. The last process is the scattering on the boundaries, which is sometimes included in the total relaxation time. This contribution takes the form [95, 96]

$$\tau_b^{-1} = \frac{b_s v_g}{L}. \tag{3.17}$$

where L is the characteristic length of the sample, while b_s is a shape factor.

Recovering the Fourier regime

Here we study the heat transport in the limit of diffusive regime and we show that we recover, starting from the BTE, the usual Fourier's law which drives the spatial evolution of the temperature inside a bulk material. We assume that that the system is close to equilibrium and we introduce a deviation function g with respect to equilibrium distribution f_0, i.e.

$$g = f - f_0. \tag{3.18}$$

Using this function g, in the case in which no external force $\mathbf{F}$ is present, the BTE reads

$$\frac{\partial g}{\partial t} + \frac{\partial f_0}{\partial t} + \mathbf{v}_g \cdot \boldsymbol{\nabla}_r f + \mathbf{v}_g \cdot \boldsymbol{\nabla}_r g = -\frac{g}{\tau}. \tag{3.19}$$

In steady-state regime the two first term vanish while close to equilibrium the gradient of the deviation function is negligible (g is a smooth function of the position). In this case, the distribution function reduces to

$$f = f_0 - \tau\, \mathbf{v}_g \cdot \boldsymbol{\nabla}_r f_0. \tag{3.20}$$

In order to deduce from the BTE the Fourier's law, we recast this expression in term of temperature gradient as follows

$$f(\mathbf{r}, \mathbf{k}) = f_0 - \tau \frac{df_0}{dT} \mathbf{v}_g \cdot \boldsymbol{\nabla}_{\mathbf{r}} T(t, \mathbf{r}). \tag{3.21}$$

Beside, we can calculate the net conductive heat flux at any point $\mathbf{r}$ as

$$\boldsymbol{\Phi}_{\text{cond}}(\mathbf{r}) = (2\pi)^3 \sum_{p=\{1,2\}} \left[\int_{-\infty}^{\infty} dk_x \int_{-\infty}^{\infty} dk_y \int_{-\infty}^{\infty} dk_z \mathbf{v}_g \hbar\omega f \right], \tag{3.22}$$

where the sum is over the polarizations. By transforming the integration over all wavevectors into an integration over all frequencies and all solid angle and by using $\mathbf{v}_g = \boldsymbol{\nabla}_{\mathbf{k}} \omega$, we can transform Eq. (3.22) using a spherical coordinate system, into

$$\boldsymbol{\Phi}_{\text{cond}}(\mathbf{r}) = \sum_{p=\{1,2\}} \int_0^{\omega_{\text{max}}} d\omega \int_0^{2\pi} d\varphi \int_0^1 d\mu \mathbf{v}_g \hbar\omega f(\mathbf{r}, \mathbf{k}) \frac{D(\omega)}{4\pi}, \tag{3.23}$$

where

$$D(\omega) = \frac{1}{2\pi^2} \left(\frac{\omega}{v_g}\right)^2 \left|\frac{dk}{d\omega}\right| = \frac{\omega^2}{2\pi^2 v_g^3} \tag{3.24}$$

is the density of states and ω_{max} is a cutoff frequency, and $\mu = cos\theta$. In the simple case of one dimensional problem along the z-direction, the conductive flux takes the form

$$\Phi_{\text{cond}}(z) = \sum_{p=\{1,2\}} \int_0^{\omega_{\text{max}}} d\omega \int_0^{2\pi} d\varphi \int_0^1 d\mu v_g \mu \hbar\omega f(\mathbf{r}, \mathbf{k}) \frac{D(\omega)}{4\pi}. \tag{3.25}$$

Substituting Eq. (3.21) in the last expression for the heat flux, we obtain (removing for the sake of simplicity the explicit dependence of f on $\mathbf{r}$ and $\mathbf{k}$)

$$\begin{aligned} &\Phi_{\text{cond}}(z) \\ &= \int_0^{\omega_{\text{max}}} d\omega \int_0^{2\pi} d\varphi \int_0^1 d\mu v_g \mu \hbar\omega \left[f_0 - \tau \frac{df_0}{dT} \mathbf{v}_g \cdot \boldsymbol{\nabla}_{\mathbf{r}} T(t, \mathbf{r}) \right] \frac{D(\omega)}{4\pi} \\ &= -\frac{1}{2} \frac{dT}{dz} \int_0^{\omega_{\text{max}}} d\omega \int_0^1 d\mu \tau v_g^2 \mu^2 \hbar\omega D(\omega) \frac{df_0}{dT}. \end{aligned} \tag{3.26}$$

This expression can be easily recast into a Fourier-like form

$$\Phi_{\text{cond}}(z) = -\kappa \frac{dT}{dz} \tag{3.27}$$

where the thermal conduction κ is given by

$$\kappa = \frac{1}{2} \int_0^{\omega_{\text{max}}} d\omega \int_0^{\pi} d\theta \tau v_g^2 C_\omega \sin\theta \cos^2\theta, \tag{3.28}$$

in which we have introduced the specific heat per unit frequency $C_\omega = \hbar\omega D(\omega) df_0/dT$. If we consider the case in which v_g and τ are isotropic, Eq. (3.28) reduced to

$$\kappa = \frac{1}{3} \int d\omega \tau v_g^2 C_\omega. \tag{3.29}$$

Specular and diffuse reflection

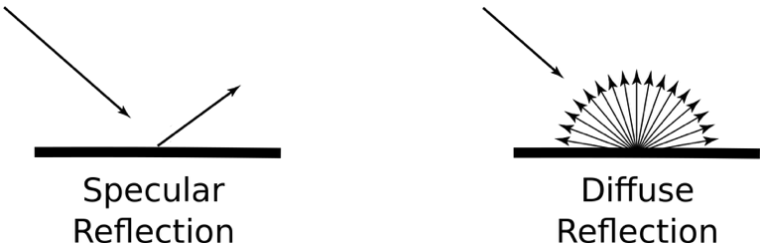

Figure 3.4: Graphical representation of the specular and the diffuse reflection.

In order to solve the BTE, we need to impose boundary conditions for each edge of our sample. In fact, when a phonon hits a boundary in contact with vacuum, it is reflected back into the sample. This reflection phenomenon can be classified into three types: specular or mirror-like, partially specular and diffuse reflections. For our scope, we focus only on the two limit cases (see Fig. 3.4). Specular reflection describes a mirror-like reflection (only the component orthogonal to the boundary is inverted), while the diffuse one allows us to describe the case in which phonons strike a surface and are equally scattered in all direction. In our study we consider the two following boundary situations:

- the sample is perfectly in contact with a thermostat;
- the edge of the sample is in front of a vacuum gap.

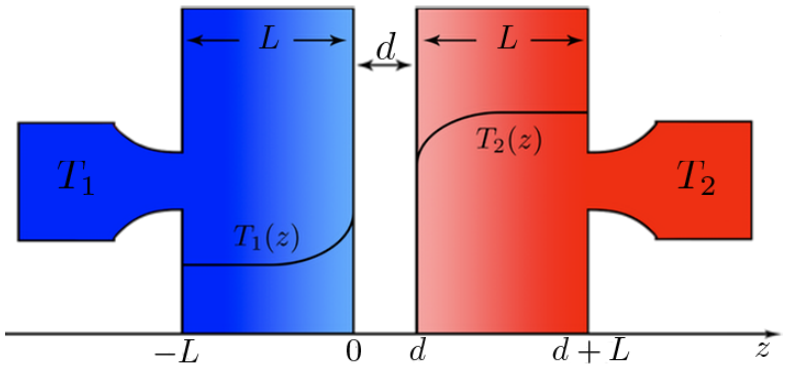

Figure 3.5: Geometry of the system. The left (right) slab lies in the interval $-L \leq z \leq 0$ ($d \leq z \leq L + d$) and its temperature profile is $T_1(z)$ [$T_2(z)$]. The left (right) slab is in contact at the left (right) boundary $z = -L$ ($z = L + d$) with a thermostat at temperature T_1 (T_2).

In the first case, in order to allow the thermalization of the sample, we need to impose the diffuse reflection. More specifically, since the presence of a thermostat fixes the temperature at the edge, this physically means that each time a phonon hits the boundary surface the presence of the thermostat imposes the Bose-Einstein distribution function corresponding to its temperature, i.e.

$$f(t, z_b, \mu) = f_0(T_b), \tag{3.30}$$

where z_b and T_b denote the position and the temperature of the boundary. Imposing this condition, after the collision the distribution is isotropic as expected by the diffuse reflection. In the second case, considering the surface as perfectly reflecting (no roughness), we can use the specular reflection in order to describe the mechanical action of the edge. Mathematically, the specular reflection can be expressed as

$$f(t, z_b, \mu) = f(t, z_b, -\mu). \tag{3.31}$$

3.3 Energy balance

The system we consider in this chapter is composed of two slabs of equal thickness L, as sketched in Fig. 3.5, assumed to be perfectly in contact with two thermostats at temperatures T_1 and T_2, respectively. These two slabs are separated by a subwavelength vacuum gap of size d. We assume the thickness of this gap larger than the tunneling distance of electrons and acoustic phonons [36, 37, 98–100], so that the slabs thermalize only by exchanging heat by radiation in near-field regime. In these conditions, the first

equation of the system concerns the internal energy density u within these bodies which must obey to the energy conservation equation as follows [51]

$$\frac{\partial u(z,t)}{\partial t} = \Phi_{\text{rad}}(z,t) + \Phi_{\text{cond}}(z,t), \tag{3.32}$$

where Φ_{rad} denotes the radiative power locally dissipated per unit volume within a given body and coming from the other one, while Φ_{cond} is the conductive power per unit volume around the point $\mathbf{r}$, respectively. The latter can be calculated as the divergence of conductive flux in Eq. (3.22). Concerning the calculation of the radiative power, we start by neglecting the energy exchanged between parts of the same slab, assuming that this contribution is negligible with respect to conduction. The power $\Phi_{\text{rad,1}}$ (resp. $\Phi_{\text{rad,2}}$) dissipated in the left (resp. right) body and associated with the sources in the other body can be calculated from the net radiative flux $\boldsymbol{\varphi}_{\text{rad,1}}$ (resp. $\boldsymbol{\varphi}_{\text{rad,2}}$) using the statistical average $\langle \mathbf{S}(\mathbf{r},\omega)\rangle = 2\,\text{Re}\langle \mathbf{E}(\mathbf{r},\omega)\times\mathbf{H}^*(\mathbf{r},\omega)\rangle$ of the Poynting vector spectrum at point $\mathbf{r}$ as

$$\boldsymbol{\Phi}_{\text{rad,k}}(\mathbf{r}) = -\int d\omega\, \boldsymbol{\nabla}\cdot\boldsymbol{\varphi}_{\text{rad,k}}(\mathbf{r},\omega). \tag{3.33}$$

According to the fluctuational-electrodynamics theory [2], the contribution to the Poynting vector coming from the sources located in the left or right body reads

$$\langle S^{1,2}_m(\mathbf{r},\omega)\rangle = i\frac{\omega^2}{c^2}\eta_{mjl}\int_{R,L} d\mathbf{r}'\epsilon''(\mathbf{r}',\omega)\Theta[T(\mathbf{r}'),\omega]\,[\mathbb{G}^{EE}_{j,l}\mathbb{G}^{EH*}_{m,l} - \mathbb{G}^{EH*}_{j,l}\mathbb{G}^{EE}_{m,l}], \tag{3.34}$$

where $\mathbf{r}$ is the point where the Poynting vector is calculated, while $\mathbf{r}'$ is evaluated in all points inside the source (2 or 1). In Eq. (3.34), η_{mjl} are the components of Levi-Civita tensor and m, j and l are referring to the three Cartesian coordinates, $\Theta(T,\omega)$ is the mean energy of a Planck oscillator at temperature T, ϵ'' the imaginary part of the permittivity in the emitting body while $\mathbb{G}^{EE} = \mathbb{G}^{EE}(\mathbf{r},\mathbf{r}')$ and $\mathbb{G}^{HE} = \mathbb{G}^{HE}(\mathbf{r},\mathbf{r}')$ are the full electric-electric and electric-magnetic dyadic Green tensors at frequency ω [101], taking into account all scattering events within the system between the emitter and the point where energy is dissipated. When calculating the monochromatic net radiative power (including both the power received by the other body and the one emitted by the body itself) appearing in Φ_{rad} dissipated at position $\mathbf{r}$, we use Eq. (3.33) [by taking the divergence of Eq. (3.34)] and finally replace $\Theta[T(\mathbf{r}'),\omega]$ by $\Theta[T(\mathbf{r}'),\omega] - \Theta[T(\mathbf{r}),\omega]$ in order to take into account the power emitted by the element located at $\mathbf{r}$ and ensure vanishing energy exchange at thermal equilibrium. By neglecting the contribution of propagative photons we obtain

$$\begin{aligned}\Phi_{\text{rad}}(z) = \frac{2}{\pi^2}\sum_p \int_0^{+\infty} d\omega \int_{\frac{\omega}{c}}^{+\infty} dk\, k\, e^{-2\text{Im}(k_z)d} G(z,\omega) \\ \times \int_0^{\delta} dz' \Big(f_0[\omega, T(z'+d)] - f_0[\omega, T(-z)]\Big) H(z',\omega).\end{aligned} \tag{3.35}$$

$G(z,\omega)$ and $H(z,\omega)$ are functions which depend on the optical properties of slabs which have the following expressions [49]

$$\begin{aligned} G(z,\omega,k) &= \mathrm{Im}[\rho(z+L)]|u^{(1,23)}u^{(3,2)}\tau(-z)|^2, \\ H(z',\omega,k) &= |\tau(z')u(z',L-z')|^2\Big[\mathrm{Re}\big[\rho(L-z')\big]\,\mathrm{Re}\Big(k_{zm}\frac{1+r^2}{1-r^2}\Big) \\ &\quad -\Big(1+|\rho(L-z')|^2\Big)\,\mathrm{Re}\Big(\frac{k_{zm}r}{1-r^2}\Big)\Big], \end{aligned} \tag{3.36}$$

where

$$\begin{aligned} &\rho(x) = r\frac{1-e^{2ik_{zm}x}}{1-r^2e^{2ik_{zm}x}}, \quad \tau(x) = \frac{(1-r^2)e^{ik_{zm}x}}{1-r^2e^{2ik_{zm}x}}, \quad u(x,y) = [1-\rho(x)\rho(y)]^{-1}, \\ &u^{(3,2)} = \big[1-\rho(-z)\rho(L)e^{2ik_zd}\big]^{-1}, \\ &u^{(1,23)} = \Big\{1-\rho(z+L)\Big[\rho(-z)+\tau^2(-z)\rho(L)e^{2ik_zd}u^{(3,2)}\Big]\Big\}^{-1}, \end{aligned} \tag{3.37}$$

r being the ordinary Fresnel coefficients for the two polarization, and k_{zm} the z-component of the wavevector inside the medium.

To deal with the phonons heat transport inside the slab, we must also solve the BTE for the distribution function f_p of phonons under the usual relaxation time approximation introduced in Sec. 3.2,

$$\frac{\partial f_p(\omega,\mu,z,t)}{\partial t} + \mathbf{v}_{g,p}\cdot\boldsymbol{\nabla} f_p(\omega,\mu,z,t) = -\frac{f_p(\omega,\mu,z,t)-f_0[\omega,T(z,t)]}{\tau_p[\omega,T(z,t)]}, \tag{3.38}$$

for each polarization state p. It is worth noticing that the Eqs. (3.32) and (3.38) are coupled because of the dependence of the conductive power Φ_{cond} on the non-equilibrium distribution function at each moment t and each point z, and also because the radiative power Φ_{rad} depends on the two temperature profiles $T_1(z,t)$ and $T_2(z,t)$.

Numerical method

In order to solve the system of Eqs. (3.32) and (3.38) and to obtain the equilibrium temperature profiles within each slab, we use an iterative process, and the control angle discrete ordinates method [102]. To this aim, we discretized all the variables of the system, namely the spatial coordinate z, the angular frequency ω and the angle θ that the group velocity creates with the $z-$axis (through the discretization of the variable μ). It is convenient to chose a non-uniform spatial discretization in order to take into account the almost surfacic dissipation of the radiative power in the case of polar materials, such

as SiC. Moreover, we transform all the continuous functions to discretized ones, using the following notation

$$\begin{aligned}
&f_p(\omega,\mu,z,t) \to f_p(\omega_i,\mu_j,z_l,t_m) \to f^m_{p,i,j,l},\\
&T_1(z,t), T_2(z,t) \to T^m_l,\\
&v_{g,p}(\omega) \to v_{g,p}(\omega_i) \to v_{p,i},\\
&\tau_p[\omega, T(z,l)] \to \tau_p(\omega_i, T^m_l) \to \tau^m_{p,i,l},\\
&f_0[\omega_i, T(z,t)] \to f^m_{0,i,l}.
\end{aligned} \tag{3.39}$$

First of all we distinguish the case in which $\cos\theta > 0$, i.e. $\mu > 0$, which means that the phonons are propagating in the positive direction along the z-axis, from the case in which, instead, $\mu < 0$. In the first situation, since phonons are propagating from the left to the right, we can only perform the spatial discretized derivations backward since we can know only the distribution function at the previous point of phonon path. The discretized system for $\mu > 0$ reads

$$\begin{cases}
f^{m+1}_{p,i,j,l} = \left[1 + dt\left(\dfrac{v_{p,i}\mu_j}{z_l - z_{l-1}} + \dfrac{1}{\tau^m_{p,i,l}}\right)\right]^{-1}\left[f^m_{p,i,j,l,m} + dt\left(v_{p,i}\mu_j \dfrac{f^{m+1}_{p,i,j,l-1}}{z_l - z_{l-1}} + \dfrac{f^m_{0,i,l}}{\tau^m_{p,i,l}}\right)\right],\\
u(T^{m+1}_l) = u(T^m_l) + dt[\Phi_{\text{rad},l}(\{T^m_l\}) + \Phi_{\text{cond},l}(\{f^m_{i,j,l}\})].
\end{cases} \tag{3.40}$$

Instead, for $\mu < 0$ we perform the discretized spatial derivation forward, obtaining

$$\begin{cases}
f^{m+1}_{p,i,j,l} = \left[1 + dt\left(-\dfrac{v_{p,i}\mu_j}{z_{l+1} - z_l} + \dfrac{1}{\tau^m_{p,i,l}}\right)\right]^{-1}\left[f^m_{p,i,j,l,m} + dt\left(-v_{p,i}\mu_j \dfrac{f^{m+1}_{p,i,j,l+1}}{z_{l+1} - z_l} + \dfrac{f^m_{0,i,l}}{\tau^m_{p,i,l}}\right)\right],\\
u(T^{m+1}_l) = u(T^m_l) + dt[\Phi_{\text{rad},l}(\{T^m_l\}) + \Phi_{\text{cond},l}(\{f^m_{i,j,l}\})].
\end{cases} \tag{3.41}$$

As initial condition for the temperature, we impose that the profiles within each slab are linear and equivalent to the average temperature at the edge of each slab facing the vacuum gap, i.e.

$$T_1(0,z) = \frac{T_2 - T_1}{2L} z + T_{\text{avg}} \quad \text{and} \quad T_2(0,z) = \frac{T_2 - T_1}{2L}(z - d) + T_{\text{avg}} \tag{3.42}$$

where we introduced the average temperature $T_{\text{avg}} = (T_1 + T_2)/2$. These profiles correspond to the temperature profiles driven by a purely diffusive process. We also impose that the initial distribution function is the Bose-Einstein distribution [$f(\omega,\mu,z,0) = f_0(\omega, T_k(0,z))$ with $k = 1, 2$] both for the left and the right slab. Finally, we impose the specular reflection in Eq. (3.31) for the edges in front of the vacuum gap and the diffuse one in Eq. (3.30) for the boundaries in contact with the thermostats. At each step of iterative process, we first update the distribution function $f^{m+1}_{p,i,j,l}$ and then, using the results, we calculate the radiative flux and the corresponding conductive power in order to

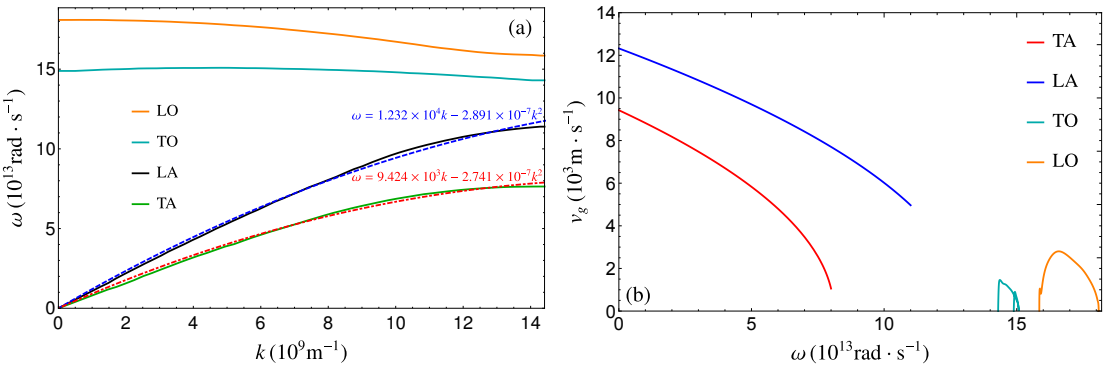

Figure 3.6: **(a)** Phonon dispersion relation of 3C-SiC [103]. The dashed blue (red dot-dashed) curve represents our fit for the longitudinal (transverse) acoustic branch. **(b)** Phonon group velocity in 3C-SiC as a function of the frequency. The blue (red) curve corresponds to the longitudinal (transverse) polarization of acoustic phonons.

use the internal energy conservation equation to obtain the new temperature profiles at the new time step. Since we are looking for the steady-state solutions, our convergence condition must be that the temporal derivative of the internal energy is almost zero, i.e. $\partial u[T(z)]/\partial t \approx 0$. For this reason, we continue the iterative process until the total flux $\Phi_{\text{rad}} + \Phi_{\text{cond}}$ is smaller than a prescribed value.

3.4 Phonon properties

To investigate the conduction-radiation coupling mechanism, we consider slabs made of silicon carbide with a zincblende crystal structure (3C-SiC), by neglecting the anisotropy of the crystal [104] and considering as phonon dispersion relation the one in the direction $[100]$, plotted in Fig. 3.6(a) [103]. Since the group velocity v_g of the optical modes is much smaller than the one of the acoustic modes [see Fig. 3.6(b)], we assume that their contribution to heat transport can be neglected. In order to model the acoustic modes, we perform two parabolic fits shown in Fig.3.6.

Callaway method for the relaxation time

In order to obtain the relaxation time for a material, we start from its bulk thermal conductivity κ. Generally speaking, in fact, κ has the expression in Eq. (3.28) which depends on the relaxation time τ. Performing a fit of the bulk experimental data of the thermal conductivity, we can then deduce the expression of τ. In literature, two different models to perform this fit for κ exist, the first one developed in 1959 is known as Callaway method [106], while the second one of 1963 is due to Holland [107]. The main

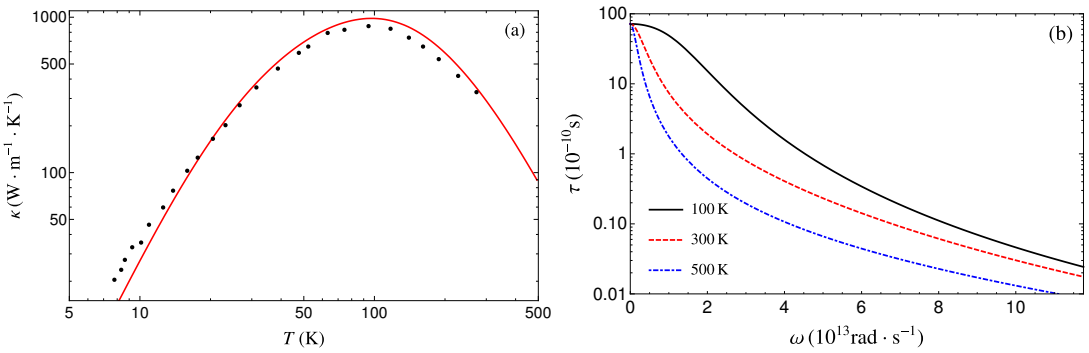

Figure 3.7: **(a)** Bulk thermal conductivity for 3C-SiC as a function of the temperature [105]. The black dots are the experimental points, the red curve is our fit. **(b)** Phonon relaxation time in 3C-SiC as a function of the frequency at three different temperatures.

different between the two is that in Callaway model the relaxation time τ is supposed independent on the polarization of the carriers, while this condition is removed in the Holland method. In this sense, the Holland method corresponds to an improvement of the first. For our purposes, we estimate that the simpler Callaway method is sufficient. The expression that we use to fit κ is then the following

$$\kappa = \sum_p \int_0^{\omega_p^{\max}} \frac{\hbar^2\omega^2}{6k_B\pi^2T^2} k_p(\omega)^2 v_{g,p}(\omega) \frac{e^{\frac{\hbar\omega}{k_BT}}(e^{\frac{\hbar\omega}{k_BT}}-1)^{-2}}{\tau^{-1}(\omega,T)}\, d\omega, \tag{3.43}$$

and the expression for τ is

$$\tau^{-1}(\omega,T) = A\omega^4 + B\omega^2T^3 + C. \tag{3.44}$$

where the term $A\omega^4$ represents the scattering by point impurities or isotopes, the term $B\omega^2T^3$ includes the umklapp processes, and C represents the boundary scattering, as introduced in the first section. The coefficients A, B and C are then identified to recover the correct dependence of κ with respect to the temperature, shown in Fig. 3.7(a) [105]. The optimal values obtained for these parameters are the following

$$\begin{aligned} A &= 2.1237 \cdot 10^{-6}\,\mathrm{s}^3, \\ B &= 4.3970 \cdot 10^{-12}\,\mathrm{s}\cdot\mathrm{K}^{-3}, \\ C &= 1.3949 \cdot 10^{-5}\,\mathrm{s}^{-1}. \end{aligned} \tag{3.45}$$

The relaxation time τ as a function of the frequency ω for different temperatures is plotted in Fig. 3.7(b), showing that the number of colliding events increases with the temperature. Once we obtained the group velocity v_g and the relaxation time τ, we easily deduced the phonon mean free path Λ as

$$\Lambda_p(\omega,T) = v_{g,p}(\omega)\tau(\omega,T). \tag{3.46}$$

In Fig. 3.8(a)-(b) we show the mean free path Λ of the longitudinal and transverse

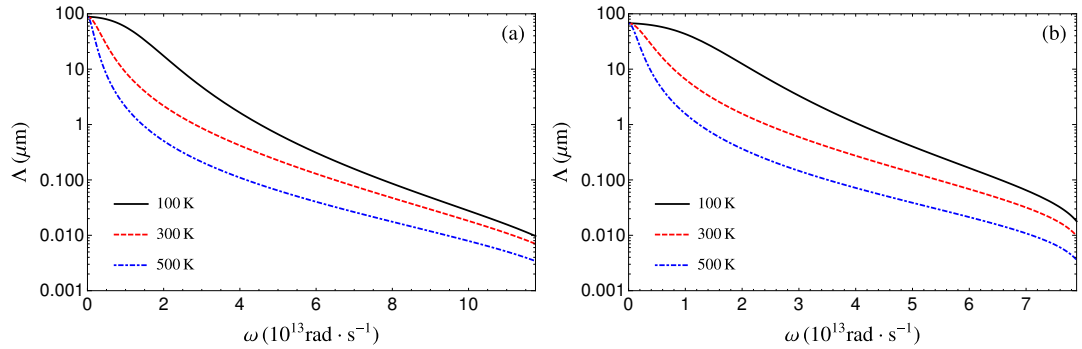

Figure 3.8: **(a)** Longitudinal phonon mean free path in SiC as a function of the frequency for different temperatures. **(b)** Transverse phonon mean free path in SiC as a function of the frequency for different temperatures.

phonons as a function of the frequency ω for different temperatures.

Using these functions to describe the 3C-SiC phononic properties, we can predict the value of thermal conductivity κ as a function of thickness L and temperature T. We first of all calculate the conductive heat flux φ_{cond} for the purely conductive case of a single slab with a difference of temperature $\Delta T \approx 1\,\text{K}$ between the two edges. Using the expression for the conductive heat flux in Eq. (3.25) and the Fourier's law we deduce the effective thermal conductivity κ. In Fig. 3.9(a) we plot κ as a function of T for different thicknesses L showing that we are able to recover the bulk experimental data shown with black point [105]. The strong dependence of the conductivity κ (and thus in turn the relevance of radiative transfer with respect to conduction within each slab) allows us to anticipate a strong dependence of coupling effects on this crucial geometrical parameter.

3.5 Equilibrium temperature profile

In the previous paragraph we discussed the phonon properties in 3C-SiC, in particular its relaxation time τ and its dispersion relation. We can now use these quantities to solve the discretized systems of coupled Eqs. (3.40)-(3.41). We first focus on the derivation of temperature profiles in steady-state regime, whereas the dynamic process (thermalization) will be discussed in the next chapter. In Fig. 3.10 we show the normalized temperature

$$\frac{T_1(z) - T_1}{T_1(0) - T_1}, \tag{3.47}$$

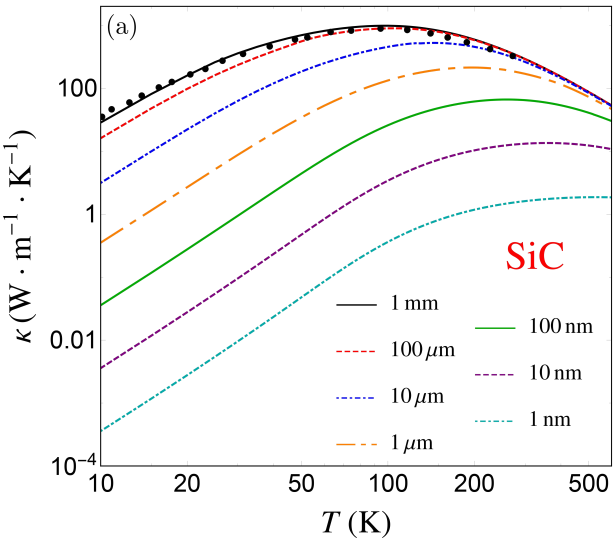

Figure 3.9: Thermal conductivity of SiC for different thicknesses as a function of temperature. The black dots are the experimental points for bulk conductivity.

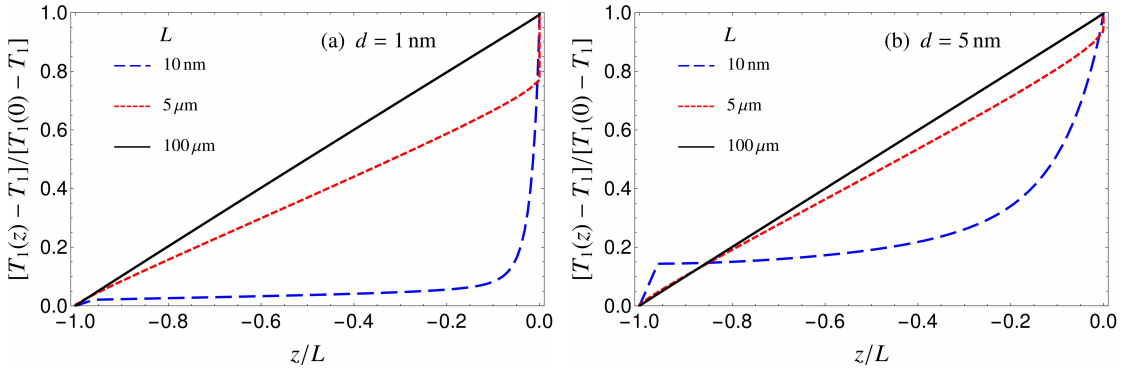

Figure 3.10: **(a)** Normalized temperature profile inside the left slab for different thicknesses and a separation distance $d = 1\,\text{nm}$. **(b)** Same as **(a)** for $d = 5\,\text{nm}$.

as a function of the normalized coordinate z/L, being the ones in the right slab qualitatively similar. We perform the numerical simulation for separation distances $d = 1\,\text{nm}$ and $d = 5\,\text{nm}$ and for different slab thicknesses L, in order to describe the thermal behavior for each conduction regime from the ballistic to the diffusive regime. From now on, if not differently indicated, we chose $T_1 = 400\,\text{K}$ and $T_2 = 300\,\text{K}$.

When the thickness is small ($L = 10\,\text{nm}$) compared to the mean free path of phonons (see Fig. 3.8) the regime of transport is ballistic. This is confirmed by the almost constant temperature profiles, shown in Fig. 3.10 both for $d = 1\,\text{nm}$ and $d = 5\,\text{nm}$. This corresponds to the so-called Casimir regime for which the phonon do not undergo scat-

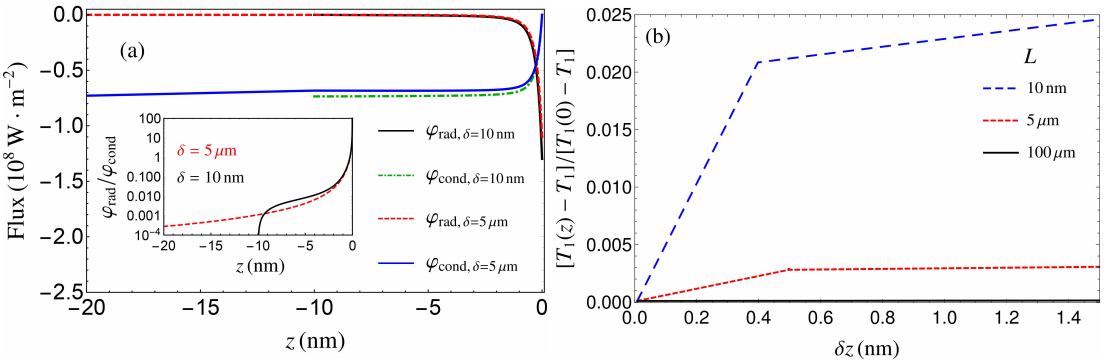

Figure 3.11: **(a)** Radiative flux φ_{rad} within the left slab in a system of two 3C-SiC slabs of thickness $L = 10\,\text{nm}$ and $L = 5\,\mu\text{m}$ separated by a vacuum gap of thickness $d = 1\,\text{nm}$ and thermostated on their back sides at $T_1 = 300\,\text{K}$ and $T_2 = 400\,\text{K}$. Inset: ratio between φ_{rad} and the conductive flux φ_{cond}. **(b)** Focus on the normalized temperature profile of the left slab in its first $1.5\,\text{nm}$ for $10\,\text{nm}$, $5\,\mu\text{m}$ and $100\,\mu\text{m}$ of thickness.

tering events inside the film. In this regime the continuity of heat flux at the interface leads to a discontinuity of the temperature close to the boundaries ($z = 0$ for the left slab, $z = L + d$ for the right slab) where the slabs are put in contact with a thermostat. The situation is different close to the internal interfaces facing the vacuum gap, where we note a sharp but continuous temperature variation. In these regimes, phonons interact with photons through the near field heat exchange. In this sense, we are not anymore in a ballistic regime. As shown in Fig. 3.11(a) where the radiative heat flux as a function of the coordinate z is represented, this sharp temperature variation corresponds to the region where almost all the radiative energy carried by evanescent photons is dissipated. This corresponds to the zone where the radiation-conduction coupling effectively takes place. Moreover, as shown in the inset of Fig. 3.11(a) we see that in this region the radiative flux surpasses the conductive flux by two orders of magnitude close to the interface. Therefore, the phonons cannot cool down efficiently this region through their coupling with the external reservoir. As a result, the slab is significantly heated up locally, close to the exchange surfaces. On the other hand, beyond this region, the conductive flux dominates the rapidly decaying radiative flux, so that the atomic lattice is thermalized at the reservoir temperature thanks to the ballistic phonons.

For thick films of the order of the phonons mean free path ($L > 5\,\mu\text{m}$), the regime of phonon transport is almost diffusive [see Fig. 3.14]. In this case, as in the ballistic regime the radiative flux still dominates over the conductive one within a few nm from the vacuum interface, as shown in the inset of Fig. 3.14(a). However, being this region very small compared to the size of the sample, the temperature profiles is mainly linear [see Fig. 3.14].

In Fig. 3.12 we show the absolute temperature profile in the left slab $[T_1(z) - T_1]$ as a

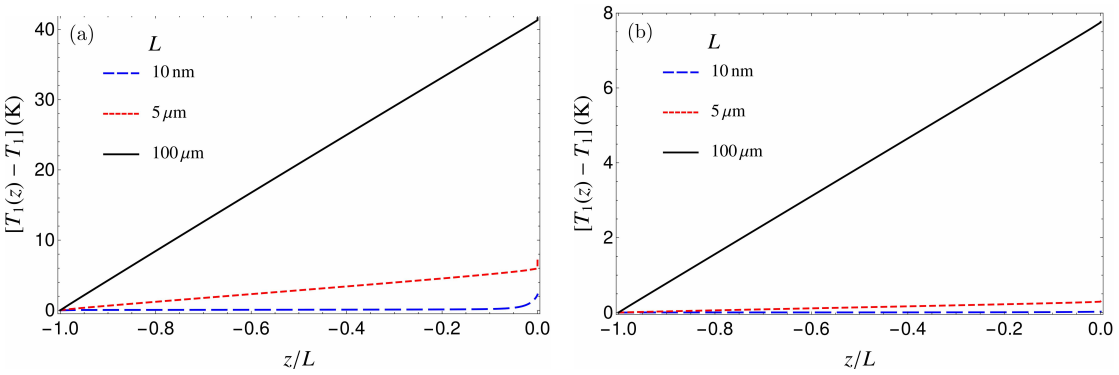

Figure 3.12: Steady-state temperature in the left slab for different thicknesses [10 nm (blue long-dashed line), 5 μm (red short-dashed line) and 100 μm (black solid line)] at separation distance $d = 1$ nm (a) and $d = 5$ nm (b), with $T_1 = 300$ K and $T_2 = 400$ K.

function of the normalized coordinate z/L. These figures allow first of all to understand that the temperature gradient strongly depends on the thicknesses of the slabs. Indeed, in the ballistic regime the maximum temperature gradient is much smaller with respect to the diffusive case ($L = 100\,\mu$m), both for $d = 1$ nm and $d = 5$ nm. As a matter of fact, in the diffusive case ($L = 100\,\mu$m) the maximum temperature gradient is around 40 K for $d = 1$ nm while its maximum value is around 8 K for $d = 5$ nm. While, in the ballistic case, i.e. 10 nm, we get only ~ 2 K for $d = 1$ nm and ~ 0.5 K for $d = 5$ nm. These results show that the the diffusive conduction regime allows a more efficient thermalization along the sample, creating a strong temperature profile. It is worth noting that, comparing the profiles for $d = 1$ nm and $d = 5$ nm, while the qualitatively shape of the profiles remains always similar, the overall temperature gradient decreases significantly when increasing d, in accordance with the strong $1/d^2$ scaling of the near-field radiative heat flux.

In order to distinguish more precisely the difference between two regimes, we focus in Fig. 3.11(b) on the behavior of $[T_1(z) - T_1]/[T_1(0) - T_1]$ really close to the left edge, plotting this quantity in the first 1.5 nm from the contact point with the thermostat of the first slab in the case of $d = 1$ nm. We see that the typical jump of the ballistic regime is clearly visible for $L = 10$ nm and $L = 5\,\mu$m, but it completely disappears in the diffusive regime ($L = 100\,\mu$m). Anyway, its amount becomes less and less relevant compared to $T_1(0) - T_1$ when the thickness increases.

It is interesting also to study the behavior of the temperature maximum gradient $T_1(0) - T_1$ as a function of the thicknesses L, which is shown in Fig. 3.13 for $d = 1, 5, 10$ nm. For $d = 1$ nm, at the beginning we have an increase of temperature at the vacuum gap boundary which is almost linear, but, for $L > 30\,\mu$m the behavior changes and the curve goes asymptotically to a saturation value close to 50 K coincid-

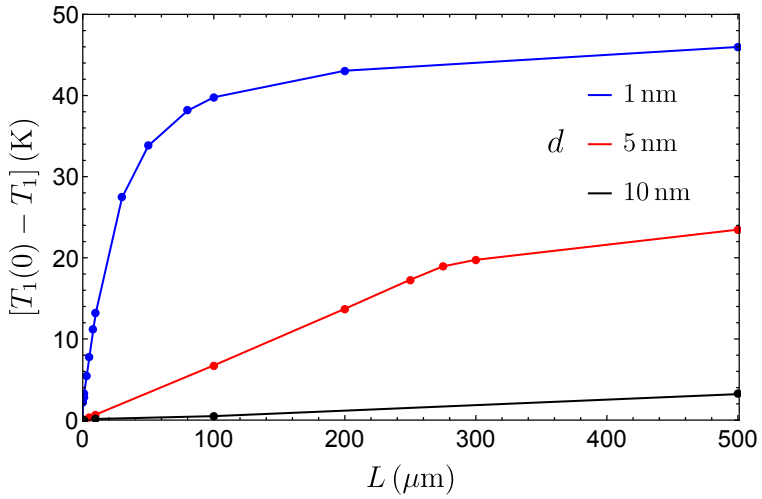

Figure 3.13: Temperature variation $T_1(0) - T_1$ between the left slab and the thermostat temperature of the left slab as a function of the slab thickness for several separation distances (blue for $d = 1$ nm, red for $d = 5$ nm and black for $d = 10$ nm).

ing with half of the total temperature difference $T_2 - T_1$ between the two thermostats. In simplified scenario of a purely surfacic radiative flux this saturation value corresponds to the situation in which the radiative heat flux is minimized. For $d = 5$ nm and $d = 10$ nm the increase in the temperature maximum gradient $T_1(0) - T_1$ is significantly less pronounced, and for $d = 10$ nm a gradient is barely visible even for thickness $L = 500\,\mu$m.

3.6 Limitations of the PvH's theory in extreme near-field regime

We now discuss how the main assumption of the PvH's theory (perfectly conductive solids) fails to describe the heat exchange between two solids in extreme near-field regime. To this aim, let us first discuss the impact of conduction/radiation coupling on the value of radiative flux. We first focus on the spatial distribution of radiative flux φ_{rad} within the left slab. The results predicted by the PvH theory for two slabs set at uniform temperatures $T_1 = 300$ K and $T_2 = 400$ K are shown in Fig. 3.14(a) inside the first 20 nm from the vacuum gap for $L = 10$ nm and $L = 5\,\mu$m for $d = 1$ nm. For the considered thicknesses the flux is rapidly decaying and its value is almost the same between the two thicknesses over the first 2 nm [108, 109]. In the inset we show the ratio between the exact value of the flux (taking into account the radiation/conduction coupling mechanism and then using the equilibrium temperature profile to perform the

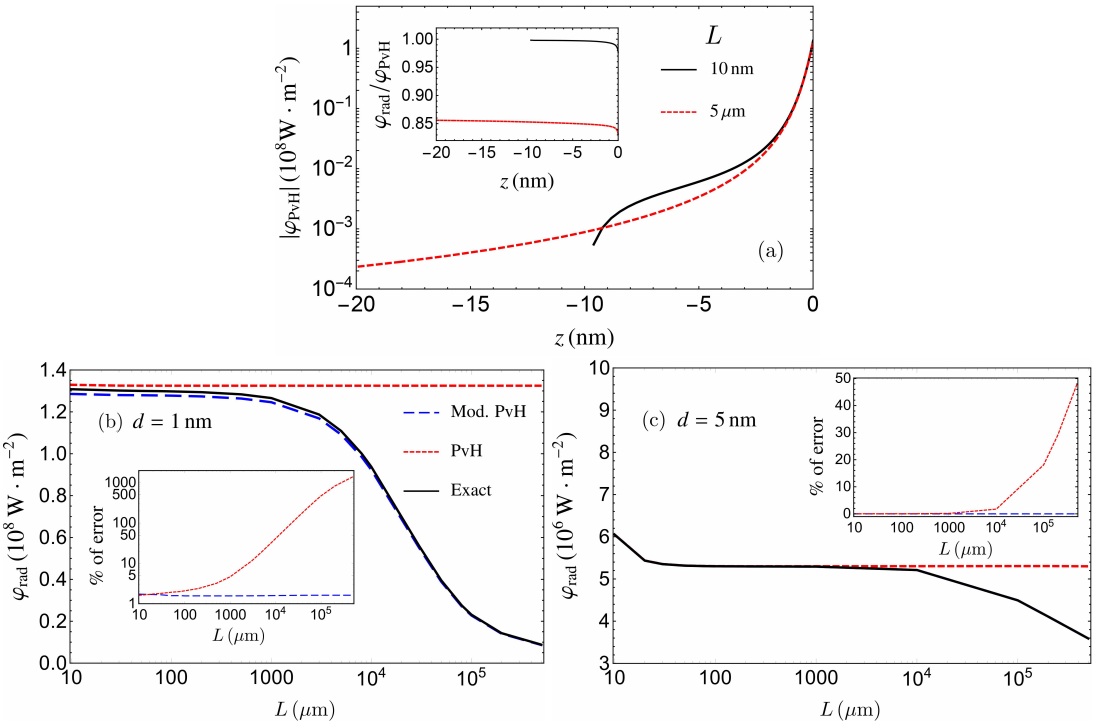

Figure 3.14: (a) Absolute value of the PvH flux within the left slab for $L = 10\,\mathrm{nm}$ and $L = 5\,\mu\mathrm{m}$ for a separation distance $d = 1\,\mathrm{nm}$. Inset: ratio between the exact radiative flux φ_{rad} and the PvH prediction. **(b - c)** Radiative heat flux exchanged between two 3C-SiC slabs with respect to their thickness for a separation distance of (a) $d = 1\,\mathrm{nm}$ and (b) $d = 5\,\mathrm{nm}$. We show the exact result (black line), the PvH one (red dashed line, uniform temperatures $T_L = 300\,\mathrm{K}$ and $T_R = 400\,\mathrm{K}$) and the modified PvH flux (blue long-dashed line, uniform temperatures equal to the temperatures at the boundaries with the vacuum gap in the steady states resulting from the coupling with conduction). Insets: absolute value of the error with respect to the PvH and modified PvH approaches calculated as $|\varphi_{\mathrm{Exact}} - \varphi|/\varphi_{\mathrm{Exact}}$ with $\varphi = \varphi_{\mathrm{PvH}}$ or $\varphi = \varphi_{\mathrm{Mod.\ PvH}}$.

calculation) and the PvH predictions. As expected from the study of the equilibrium profiles, for $L = 10\,\mathrm{nm}$ the PvH description is reliable (the increasing of temperature at the vacuum gap boundary is almost negligible). On the contrary, in the case of higher thicknesses, the radiative heat flux exchanged between the two solids is largely overestimated by using the PvH formalism, as a result of the conduction-induced temperature profile.

We finally focus on the net radiative flux exchanged between the two slabs and compare it to the flux predicted by the PvH theory when the two bodies are held at uniform temperature. More specifically, we compare the exact flux to the PvH one with $T_1 = 300\,\mathrm{K}$ and $T_2 = 400\,\mathrm{K}$, and to the PvH result using as slab temperatures the values of the temperatures at the boundaries with the vacuum gap in the steady states

derived from our approach [$T_1(0)$ for the left slab and $T_2(d)$ for the right one]. For the latter we use the label *modified PvH*, since we are exploiting the PvH framework but using the temperature obtained through our new approach. At $1\,\text{nm}$ separation distance [Fig.3.14(b)], we see that for slab thicknesses larger than about $1\,\mu\text{m}$ the discrepancy between the PvH prediction and our theory increases dramatically. The relative error is close to 5% when $L = 1\,\mu\text{m}$ and scales as L^2 beyond this thickness. In slabs of such thicknesses the regime of heat transport becomes almost diffusive and the difference with the PvH theory comes from the linear variation of temperature profile which significantly reduces the temperature difference between the slabs. With thinner slabs the difference between the exact and the PvH theory becomes less pronounced, despite the temperature drop close to the internal interfaces highlighted previously. This is due to the fact that the temperature within the slabs remains almost unchanged with respect to the thermostat one. Nevertheless in these cases a relative error of about 2% persists. Focusing on the modified PvH result, we note that it pretty well reproduces the exact results for any slab thickness. This demonstrates that the heat transfer between two solids in the extreme near field is indeed mainly a surface-interaction mechanism. Nevertheless, while this is interesting from a fundamental point of view, we stress that the modified PvH calculation cannot be obtained without a full solution of the problem including the coupling mechanism. In Fig. 3.14(c) the case $d = 5\,\text{nm}$ is shown: with the increasing of the vacuum gap, we see that for thin slabs (i.e. ballistic regime) the predictions of the PvH theory match perfectly well the exact calculation. As highlighted in the previous section, in this case the radiative coupling between the two slabs is significantly smaller than $d = 1\,\text{nm}$ so that the induced temperature gradient is much smaller [see Fig. 3.12(b)]. In this scenario, we only see a discrepancy with respect to the PvH results for large thicknesses, whereas the agreement with the modified PvH results is almost perfect. It is also interesting to note that from large thicknesses the percentage of error [Inset of Fig. 3.14(b)] for the PvH case has an asymptotic behavior due to the saturation of absolute temperature already shown in Fig. 3.13. Moreover the comparison of results plotted in Figs. 3.14(b) and (c) shows that for thins films the radiative flux fits perfectly well the usual $1/d^2$ scaling law as predicted by the PvH theory. On the other hand, for thicker films (i.e. when the deviation with the PvH becomes more significant) this flux increases slower when the separation distance is reduced. This “saturation or attenuation effect" induced by the radiation-conduction coupling is consistent with the previous calculations [49].

3.7 Conclusions

In this chapter we introduced a general theory to describe heat exchanges between two closely-spaced solids of arbitrary size taking into account the conduction-radiation coupling between the two bodies, which is not included in PvH theory. We started by

introducing in Sec. 1 and 2 the different heat-transport regimes through the definition of a dimensionless number, the Knudsen number, and we discussed the Boltzmann transport equation and the fundamental relaxation time approximation. We then wrote the equations governing the system of two parallel planar slabs made of 3C-SiC showing that the coupling produces an inhomogeneous temperature profile within each body, resulting in a radiative flux which can differ significantly from the one predicted by the PvH theory. Finally, we analyzed the equilibrium temperature profile obtained through the numerical simulations and we compared the heat flux calculated using the new theoretical framework to the standard flux obtained using the PvH theory.

As a matter of fact, it has been shown that, for the case of a polar material such as 3C-SiC, the deviation considering conduction-radiation coupling with respect to the PvH theory is significant in the diffusive regime. Instead, concerning the case of metals, the deviation with respect to the predictions coming from the PvH theory is much less significant. Indeed, in this case, the power exchanged by radiation in near-field regime between the two solids is orders of magnitude smaller than between polar materials. Therefore, the coupling mechanism between conduction and radiation becomes negligible and the temperature profile inside each solid is only driven by conduction.

This new theory can be relevant in order to model experiments exploring heat transfer in the extreme near-field regime. In fact, it allows a better temperature and heat-flux description at nanoscale and could find applications in the fields of nanoscale thermal management, heat-assisted data recording (local heating) and nanoscale energy conversion. On a theoretical level, the study of the conduction-radiation coupling in non-planar geometry is an interesting prospect because it should make it possible to evaluate the importance of this effect in experimental setups like microscope probes. The role played by non-local electromagnetic effects also remains to be explored. Finally, ab-initio calculations could be used to investigate the coupling mechanism in the crossover regime between conduction and radiation.

Chapter 4

Relaxation dynamics in the presence of conduction-radiation coupling

The scope of this chapter is to study the relaxation dynamics in the presence of conduction-radiation coupling and to compare this relaxation process to the reference evolution coupling to the Polder and van Hove approximation (i.e. purely radiative heat exchange). In fact, the cooling dynamics in the PvH case does not take into account the transport of heat due to conduction within each slab. In this purely radiative case, the slabs are assumed perfectly conducting so that at each instant the temperature profile in each body remains uniform. In the first section we describe the physical system and the boundary conditions, while in the second section we study the relaxation dynamics in the reference case of the PvH approximation. In Sec. 3 we study the relaxation process in the conduction-radiation coupling case. As a first approximation, we start by con-

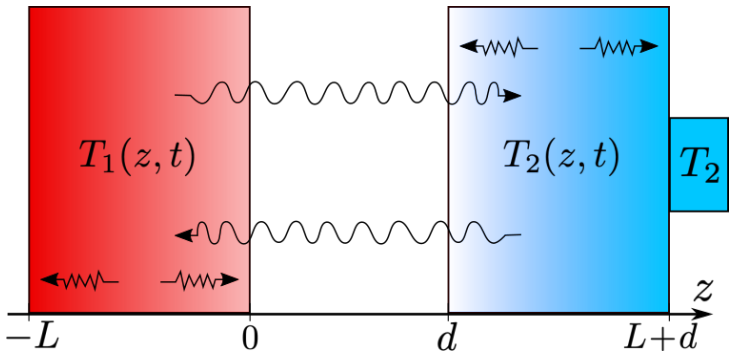

Figure 4.1: Geometry of the system. The left and right slab lie in the interval $-L \leq z \leq 0$ and $d \leq z \leq L + d$, respectively, and interact through radiative exchange. Inside each slab, heat spreads through conduction and the temperature profiles $T_1(z,t)$ and $T_2(z,t)$ are spatially dependent. The second slab is assumed to be in contact at the right boundary at $z = L + d$ with a thermostat at temperature T_2.

sidering the radiative heat flux as a purely surfacic term, focusing on the cases of two polar slabs made of SiC or SiO_2. We then study the relaxation process going beyond the approximation of surfacic radiative flux, in the same configurations, considering the establishment of a temperature profile within both slabs. Next we compare the numerical results obtained for this last case to the analytical and PvH relaxation processes. Finally, in the last part, we investigate the relaxation of two metallic slabs interacting in the extreme near-field regime at distances where heat is mainly carried by means of electron tunneling.

4.1 Physical system and boundary conditions

We study the relaxation dynamics of micron-sized objects separated by a vacuum gap in the nanometer range, interacting by radiation in the near-field regime. We restrict here, for the sake of clarity, to a system made of two slabs (Fig. 4.1) of the same material and of same thickness L, which are separated by a distance $d \ll \lambda_{\text{th}}$, λ_{th} being the thermal wavelength. At the beginning of the relaxation process both slabs have uniform temperature profiles, $T_1(z,0) = T_2 + \Delta T$ and $T_2(z,0) = T_2$, respectively. The temperature $T_2(L+d,t)$ at the right end of the second slab is held at value T_2 through a perfect contact with a thermostat while the left slab is free to interact in far field with an external bath. However, since the two slabs are kept at subwavelength distance, the heat exchanged with this bath can be neglected. From now on, if not differently specified, the parameters that we consider are the following: $T_2 = 300\,\text{K}$, $\Delta T = 100\,\text{K}$, $L = 100\,\mu\text{m}$ and $d = 1\,\text{nm}$ [52].

Since no other thermostat is present in this system, it is clear that each part of it will relax toward temperature T_2. In the following we show that the relaxation time τ needed to reach this equilibrium state can dramatically change when heat is carried by conduction inside the slab, in comparison with the situation where each slab is assumed to have an infinite thermal conductivity and heat exchange within the system is thus purely radiative. This situation corresponds to a system where the usual assumptions of the PvH theory are fulfilled. This situation actually does not allow the establishment of a temperature profile within the slabs. As a first step in this study, in the next section we will derive and describe the temporal evolution of temperatures in this reference configuration.

4.2 Relaxation in the Polder and van Hove case

When the conductive transport within each slab is assumed to be perfectly efficient (infinite conductivity), the temperature profile is uniform at any time t during the whole relaxation process and the temperature evolution is only driven by radiative exchanges.

Since the right slab is in contact with a thermostat, its temperature does not evolve. As far as the temperature of the left slab is concerned, its evolution is described by the following differential equation

$$\begin{cases} L\rho\, C_p \dfrac{dT_1}{dt} = -h^R\,[T_1(t) - T_2], \\ T_1(0) = T_2 + \Delta T, \end{cases} \tag{4.1}$$

in which ρ is the density of the material and C_p its specific heat capacity. Here we have assumed that the initial temperature bias ΔT is sufficiently small so that the slab stays close to thermal equilibrium during the entire relaxation process. Hence the radiative heat exchanges can be linearized around the equilibrium temperature and we can use a simple heat transfer coefficient h^R to describe the radiative flux. It follows that the solution of Eq. (4.1) reads

$$T_1(t) = T_2 + \Delta T \exp\left[-\frac{h^R}{L\rho\, C_p} t\right]. \tag{4.2}$$

Hence we see that the temperature decays exponentially with respect to time and the relaxation time is $\tau_{\text{PvH}} = L\rho\, C_p / h^R$.

4.3 Relaxation in the presence of coupling

We now release some assumptions from the PvH theory by assuming that each slab is not perfectly conducting anymore. As shown in Chap. 3, in this case we can limit our investigation to systems with slab thicknesses much larger than the mean free path of phonons (i.e. diffusive regime). Indeed, for thinner slabs the conduction regime becomes quasi ballistic and we recover the results predicted by the PvH theory. In the Fourier regime the temperature evolution inside each slab can be obtained by solving the conduction-radiation coupled system

$$\rho\, C_p \frac{\partial T_k(z,t)}{\partial t} = -\kappa \boldsymbol{\nabla}^2 T_k(z,t) + \Phi_{\text{rad},k}(z,t), \qquad k = 1, 2 \tag{4.3}$$

in which $\Phi_{\text{rad},k}$ is the radiative heat flux received by the elementary volume of slab k at point z and coming from the other slab. This flux has been defined in Eq. (3.35). The first term of RHS corresponds to the heat flux carried by conduction through the slab. We show in Fig. 4.2 the normal component of Poynting vector as a function of the penetration depth. We can clearly see that after $1\,$nm for SiC and after $10\,$nm for SiO_2 the value is already reduced by an order of magnitude, as discussed in Chap. 3, showing that the radiative transfer is manly surfacic. Thus a first approximation for the solution of system in Eq. (4.3) can be obtained by considering the radiative heat transfer as a surface term.

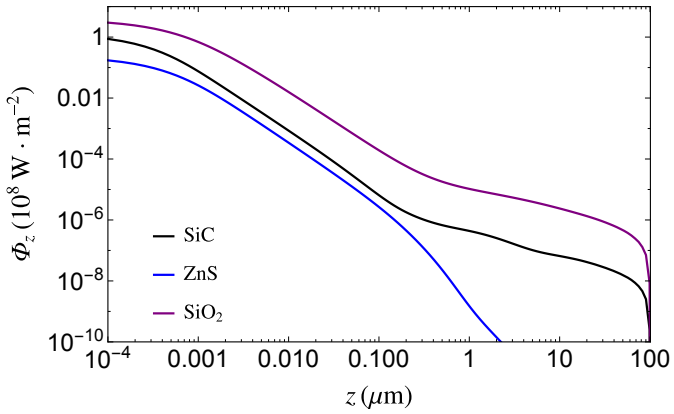

Figure 4.2: The z-component of the Poynting vector as a function of the penetration depth for the left slab, for SiO_2 (purple), ZnS (blue) and SiC (black) for the case of $T_2 = 300\,\mathrm{K}$, $\Delta T = 100\,\mathrm{K}$ and $d = 1\,\mathrm{nm}$.

Analytical method

In the approximation of surfacic radiative heat exchange the dynamical evolution of the temperature profile can be solved analytically. In agreement with previous studies [49], we will assume that conductive channel is the dominant mode inside the slab and thus neglect radiative heat exchange between portions of the same slab. Moreover, close to thermal equilibrium the flux exchanged between the two slabs can be linearized and described by a radiative conductance h^R, depending only on the right (left) boundary temperature of the first (second) slab. By introducing the auxiliary functions $F_i(z,t) = T_i(z,t) - T_2$, the differential equations governing the temperature profiles in both slabs read [52]

$$\begin{cases} \rho C_p \dfrac{\partial F_1(z,t)}{\partial t} = \kappa \dfrac{\partial^2 F_1(z,t)}{\partial z^2}, \\ \rho C_p \dfrac{\partial F_2(z,t)}{\partial t} = \kappa \dfrac{\partial^2 F_2(z,t)}{\partial z^2}, \\ F_1(z,0) = \Delta T, \quad -L < z < 0, \\ F_2(z,0) = 0, \quad d < z < L + d, \\ F_2(L+d,t) = 0, \\ \dfrac{\partial F_1(-L,t)}{\partial z} = 0, \\ \dfrac{\partial F_1(0,t)}{\partial z} = -\dfrac{h^R}{\kappa}[F_1(0,t) - F_2(d,t)], \\ \dfrac{\partial F_2(d,t)}{\partial z} = -\dfrac{h^R}{\kappa}[F_1(0,t) - F_2(d,t)]. \end{cases} \tag{4.4}$$

In Eq. (4.4) the two initial conditions $F_1(z,0) = \Delta T$ and $F_2(z,0) = 0$ correspond to the fact that the initial temperature profiles in the two slabs are uniform [$T_1(z,0) = T_2 + \Delta T$ and $T_2(z,0) = T_2$]. The boundary condition $F_2(L+d,t) = 0$ fixes the temperature at T_2 for the edge of the right slab in contact with the thermostat, while $\partial_z F_1(-L,t) = 0$ imposes a vanishing flux at each instant at the left end of the first slab (adiabatic boundary condition). Notice that this condition is based on the fact that the interactions in the far-field regime with the bath are negligible. The last two boundary conditions at the slab interfaces in $z = 0$ and $z = d$ ensure the flux continuity between the two slabs. Using the separation of variables $F_i(t,z) = A_i(z)B_i(t)$ we get

$$\frac{B_i'(t)}{\alpha B_i(t)} = \frac{A_i''(z)}{A_i(z)} = -\gamma_i, \tag{4.5}$$

where we have introduced the diffusivity $\alpha = \kappa/(\rho C_p)$, and γ_i is a constant. By solving these two ordinary differential equations, we get

$$B_i(t) = B_{0i} e^{-\gamma_i \alpha t}, \tag{4.6}$$

and

$$A_i(z) = A_{i1}\cos(\sqrt{\gamma_i} z) + A_{2i}\sin(\sqrt{\gamma_i} z). \tag{4.7}$$

The integration constants can be readily obtained by using the boundary conditions. Notice first that, since these conditions must be verified at any time t, we must have

$$\gamma_1 = \gamma_2 = \gamma. \tag{4.8}$$

From $\partial_z F_1(-L,t) = 0$ and $F_2(L+d,t) = 0$ we obtain, after renaming the constants

$$A_1(z) = A\cos[\sqrt{\gamma}(z+L)], \quad A_2(z) = B\sin[\sqrt{\gamma}(z-L-d)], \tag{4.9}$$

and

$$\begin{cases} -A\sqrt{\gamma}\sin(\sqrt{\gamma}L) = -\dfrac{h^R}{\kappa}[A\cos(\sqrt{\gamma}L) + B\sin(\sqrt{\gamma}L)], \\ B\sqrt{\gamma}\cos(\sqrt{\gamma}L) = -\dfrac{h^R}{\kappa}[A\cos(\sqrt{\gamma}L) + B\sin(\sqrt{\gamma}L)]. \end{cases} \tag{4.10}$$

Thus

$$\begin{cases} \left[\dfrac{h^R}{\kappa}\cos(\sqrt{\gamma}L) - \sqrt{\gamma}\sin(\sqrt{\gamma}L)\right]A + \dfrac{h^R}{\kappa}\sin(\sqrt{\gamma}L)B = 0,, \\ \dfrac{h^R}{\kappa}\cos(\sqrt{\gamma}L)A + \left[\dfrac{h^R}{\kappa}\sin(\sqrt{\gamma}L) + \sqrt{\gamma}\cos(\sqrt{\gamma}L)\right]B = 0. \end{cases} \tag{4.11}$$

Keeping the non-trivial solution of this system, we get

$$\sqrt{\gamma}L\tan(2\sqrt{\gamma}L) = 2\frac{h^R L}{\kappa}. \tag{4.12}$$

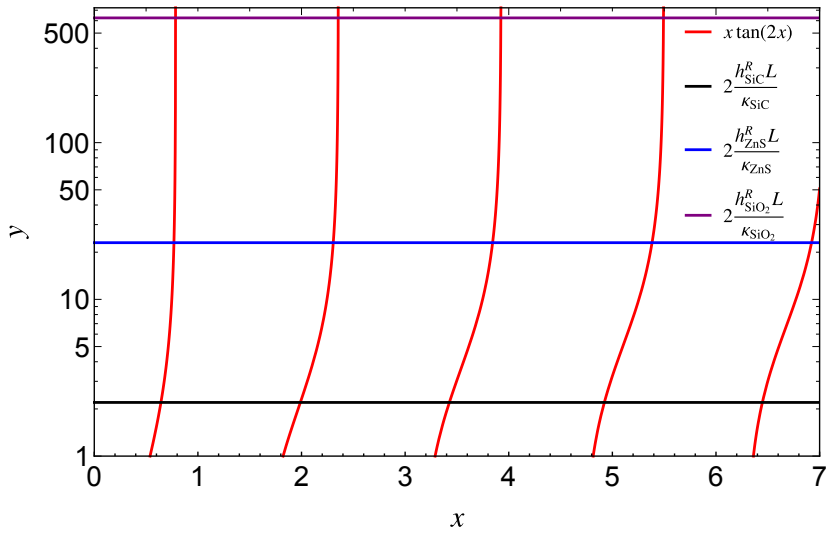

Figure 4.3: Graphical solution of Eq. (4.12) for different materials when $L = 100\,\mu$m, $d = 1$ nm and $\Delta T = 300$ K and $T_2 = 300$ K.

Material	$h^R\,(10^6\,\mathrm{W\cdot m^{-2}\cdot K^{-1}})$	$\kappa(\mathrm{W\cdot m^{-1}\cdot K^{-1}})$	$h^R L/\kappa$
SiC	1.32	120	1.1
ZnS	1.99	16.7	11.9
SiO_2	3.75	1.2	312.5

Table 4.1: Radiative conductance, thermal conductivity and the ratio $h^R L/\kappa$ for different materials. The parameters chosen are $L = 100\,\mu$m, $d = 1$ nm, and $T = 300$ K.

The resolution of this transcendental equation with respect to γ (graphically shown in Fig. 4.3) results in an infinite set of solutions $\{\gamma_n\}$ ($n = 1, 2, \dots$) and allows to get the temperature profiles in both slabs

$$\begin{aligned} T_1(z,t) &= T_2 + \sum_{n=1}^{\infty} D_n \cos\Big[\frac{x_n(z+L)}{L}\Big] \exp\Big[-\frac{x_n^2\alpha}{L^2}t\Big], \\ T_2(z,t) &= T_2 - \sum_{n=1}^{\infty} D_n \tan x_n \sin\Big(\frac{x_n z}{L}\Big) \exp\Big[-\frac{x_n^2\alpha}{L^2}t\Big], \end{aligned} \tag{4.13}$$

in which we introduced the quantity $x_n = \sqrt{\gamma_n}L$. In this equation appears the ratio $h^R L/\kappa$ [through the solution of transcendental Eq. (4.12)] which represents a relative measure of the efficiency of the radiative heat transfer with respect to the conduction. In Tab. 4.1 we give this ratio for various materials supporting surface phonon-polaritons in

the mid-infrared. These data indicate that SiO_2 is probably the best material to observe a deviation with respect to the PvH theory.

Finally, using the initial conditions, i.e. the third and the forth relations in the system in Eq. (4.4), we get the system

$$\begin{aligned} \sum_{n=1}^{\infty} D_n \cos\Big[\frac{x_n(z+L)}{L}\Big] &= \Delta T, \\ -\sum_{n=1}^{\infty} D_n \tan x_n \sin\Big[\frac{x_n(z-L-d)}{L}\Big] &= 0, \end{aligned} \tag{4.14}$$

along with the normalization relation

$$\begin{aligned} \frac{1}{L}\Big\{ \int_{-L}^{0} dz \cos\Big[\frac{x_n(z+L)}{L}\Big] \cos\Big[\frac{x_m(z+L)}{L}\Big] \\ + \int_{d}^{L+d} dz \tan(x_n)\tan(x_m) \sin\Big[\frac{x_n(z-L-d)}{L}\Big] \sin\Big[\frac{x_m(z-L-d)}{L}\Big]\Big\} \\ = \delta_{nm} \frac{4x_n + \sin(4x_n)}{8x_n \cos^2(x_n)}. \end{aligned} \tag{4.15}$$

Its resolution gives

$$D_n = \frac{8x_n \cos^2(x_n)}{4x_n + \sin(4x_n)} \frac{\Delta T}{L} \int_{-L}^{0} dz \cos\Big[\frac{x_n(z+L)}{L}\Big], \tag{4.16}$$

so that the temperature profiles read

$$\begin{aligned} T_1(z,t) &= T_2 + 8\Delta T \sum_{n=1}^{\infty} \frac{\sin x_n \cos^2 x_n}{4x_n + \sin(4x_n)} \cos\Big[\frac{x_n(z+L)}{L}\Big] \exp\Big[-\frac{x_n^2 \alpha}{L^2} t\Big], \\ T_2(z,t) &= T_2 - 8\Delta T \sum_{n=1}^{\infty} \frac{\sin^2 x_n \cos x_n}{4x_n + \sin(4x_n)} \sin\Big(\frac{x_n z}{L}\Big) \exp\Big[-\frac{x_n^2 \alpha}{L^2} t\Big]. \end{aligned} \tag{4.17}$$

To compare the relaxation dynamics in the presence of coupling to the predictions coming from the PvH theory, we also calculate the spacial averaging of the temperature profiles. From the analytical solutions (4.17) we straightforwardly obtain the average temperature profiles

$$\begin{aligned} \langle T_1 \rangle(t) &= T_2 + 8\Delta T \sum_{n=1}^{\infty} \frac{\sin^2 x_n \cos^2 x_n}{4x_n + \sin(4x_n)} \exp\Big[-\frac{x_n^2 \alpha}{L^2} t\Big], \\ \langle T_2 \rangle(t) &= T_2 + 8\Delta T \sum_{n=1}^{\infty} \frac{\sin^2 x_n \cos x_n (\cos x_n - 1)}{4x_n + \sin(4x_n)} \exp\Big[-\frac{x_n^2 \alpha}{L^2} t\Big]. \end{aligned} \tag{4.18}$$

The temperature profiles and their average values are given by the series expansions, where a partial relaxation time $\tau_n = L^2/(x_n^2\alpha)$ can be associated with each term. In order to compare the global relaxation time in the radiation-coupling and the PvH cases, we focus on the first term of the series: as a matter of fact, since $x_1 < x_n$ and thus $\tau_1 > \tau_n$ for all $n \geq 2$, it is the dominant term of the series. For $x < \pi/4$ the following relation is always satisfied

$$2x\tan(2x) < 4x^2. \tag{4.19}$$

Considering the following equations

$$2x\tan(2x) = \frac{4h^R L}{\kappa}, \tag{4.20}$$

and

$$4x'^2 = \frac{4h^R L}{\kappa}, \tag{4.21}$$

we can deduce, using the inequality in Eq. (4.19), that the solution x_1 of Eq. (4.20) is always smaller than the solution x' of Eq. (4.21), i.e.

$$x_1 < \sqrt{\frac{h^R L}{\kappa}}. \tag{4.22}$$

We can rewrite the relaxation time τ_n using the explicit form for the diffusivity α

$$\tau_n = \frac{L^2\rho C_p}{x_n^2\kappa}. \tag{4.23}$$

Using Eq. (4.22) we obtain

$$\tau_1 > \frac{L^2}{x'^2\alpha} = \frac{L\rho C_p}{h^R} = \tau_{\text{PvH}}, \tag{4.24}$$

which means that the relaxation due to the first term of the series in Eqs. (4.17) is slower than the relaxation for the PvH solution. Of course, this does not exclude that the relaxation times due to the other terms of the series could be smaller with respect to the PvH case and then that the conduction-radiation coupling could be faster than the PvH evolution at the very beginning. Nevertheless, since the first term in any case become dominant, the total conduction-coupling evolution is always slower that the PvH one.

Numerical method

In the analytical approach we have assumed that the radiative exchanges were surfacic. To verify the validity of this approximation we solve here the problem by releasing this constraint. To this aim we spatially discretize both slabs in N intervals, in

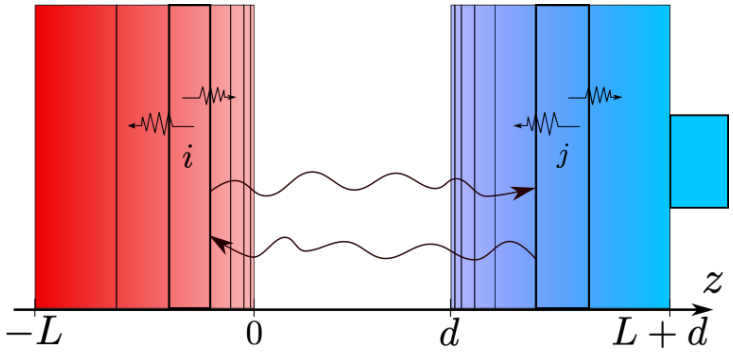

Figure 4.4: Example of discretization for two the slabs. We choose a denser discretization close to the boundaries with the vacuum gap in order to better describe the variation of the Poynting vector. Each elementary slab exchanges heat conductively with the elementary slabs around it, and radiatively with each elementary part of the other slab.

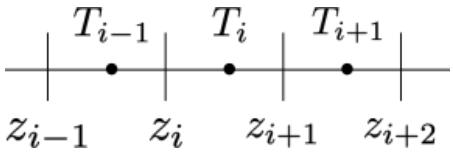

Figure 4.5: Discretization for temperatures in the first slab.

general not uniform (see Fig. 4.4). Each interval has thickness $\delta_i = z_{i+1} - z_i$, and the temperature associated with this interval is T_i as shown in Fig. 4.5. In order to have more points close to the boundaries, we decided to use a logarithmic point distribution. The discretized differential equation for the temperature T_i of the first slab read ($i \leq 1 \leq N$ and $j \leq 1 \leq N$)

$$\rho C_p \frac{dT_i}{dt}\delta_i = -\kappa \boldsymbol{\nabla}^2 T_i \delta_i + \sum_j^N \Phi_{i,j}, \tag{4.25}$$

where $\Phi_{i,j}$ is the radiative heat exchanged between the element i of the left slab and the element j of the right slab. An analogous equation is valid for the second slab.

In order to linearize the radiative heat flux, we work near to equilibrium, obtaining the following expression

$$\Phi_{i,j} \approx -h^R_{i,j}(T_i - T_j). \tag{4.26}$$

Once chosen the discretization shown in Fig. 4.5, we can use the approximation $\boldsymbol{\nabla}^2 T_i = \boldsymbol{\nabla}^2 T[(z_i + z_{i+1})/2]$ obtaining

$$\boldsymbol{\nabla}^2 T_i \approx \frac{1}{z_{i+1} - z_i}\left[\frac{dT(z_{i+1})}{dz} - \frac{dT(z_i)}{dz}\right], \tag{4.27}$$

where

$$\frac{dT(z_i)}{dz} \approx 2\frac{T_i - T_{i-1}}{z_{i+1} - z_{i-1}} \qquad \text{and} \qquad \frac{dT(z_{i+1})}{dz} \approx 2\frac{T_{i+1} - T_i}{z_{i+2} - z_i}, \tag{4.28}$$

which gives

$$\boldsymbol{\nabla}^2 T_i \approx 2\frac{T_{i+1}(z_{i+1} - z_{i-1}) - T_i(z_{i+2} + z_{i+1} - z_i - z_{i-1}) + T_{i-1}(z_{i+2} - z_i)}{(z_{i+1} - z_{i-1})(z_{i+2} - z_i)(z_{i+1} - z_i)}. \tag{4.29}$$

Using this scheme the energy balance equation can be recast in the discrete form for both slabs:

$$\frac{d}{dt}\mathbf{T} = \frac{1}{\rho C \delta_k}\mathbb{A}\mathbf{T}, \tag{4.30}$$

where $\mathbf{T}$ is the vector containing the $2N$ temperatures and $\mathbb{A}$ is the matrix which corresponds to the discrete form of transport operators. The thickness of each discretized interval has now the following form

$$\begin{aligned} &\delta_k = z_{k+1} - z_k, \qquad 1 \leq k \leq N, \\ &\delta_k = z_{k+2} - z_{k+1}, \qquad N+1 \leq k \leq 2N. \end{aligned} \tag{4.31}$$

Concerning the temperature vector $\mathbf{T}$, the elements T_k with $1 \leq k \leq N$ are the temperatures of the first slab while the remaining elements for $N+1 \leq k \leq 2N$ are the temperatures of the second slab. We now build the expression for the coefficients' matrix $\mathbb{A}$, which can be easily described as block matrix

$$\mathbb{A} = \left(\begin{array}{c|c} \mathbb{A}_{11} & \mathbb{A}_{12} \\ \hline \mathbb{A}_{21} & \mathbb{A}_{22} \end{array}\right). \tag{4.32}$$

The diagonal blocks are tridiagonal matrices, where the diagonal accounts for both radiative exchange with the other slab and conductive flux within each slab, whereas the remaining terms only describe the conductive exchange within each slab (each elementary portion of slab interacts by conduction with its closest neighbors). On the contrary, the non-diagonal blocks describe the radiative flux from each element of a slab to a given element of the other one. The explicit expression of the matrix coefficients can be directly deduced from Eqs. (4.26) and (4.29). They read

$$A_{1,1} = -\sum_j^N \frac{h^R_{1,j}}{\delta_1} + \frac{2\kappa}{z_3 - z_1}, \quad A_{N+1,N+1} = -\sum_i^N \frac{h^R_{i,1}}{\delta_{N+1}} + \frac{2\kappa}{z_{N+4} - z_{N+2}}, \tag{4.33}$$

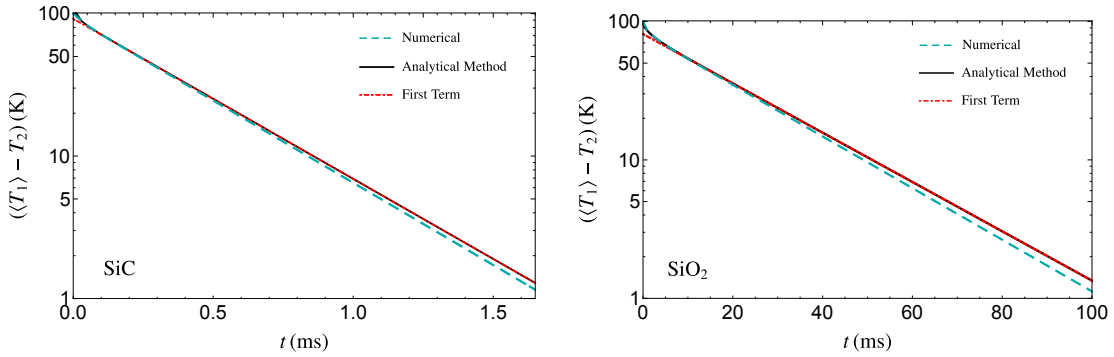

Figure 4.6: **(a)** Comparison of the numerical (cyan dashed) and the analytical (black) average temperature differences for two slabs of SiC, when $T_2 = 300\,\mathrm{K}$ and $\Delta T = 100\,\mathrm{K}$ for a separation distance $d = 1\,\mathrm{nm}$. The red dot-dashed line corresponds to the first term only of the analytical solution. The green curve shows the exact time evolution which has been calculated numerically. **(b)** Same representation for two SiO_2 slabs.

$$A_{1,2} = -\frac{2\kappa}{z_3 - z_1}, \qquad A_{N+1,N+2} = -\frac{2\kappa}{z_{N+4} - z_{N+2}}, \tag{4.34}$$

$$A_{N,N} = -\sum_j^N \frac{h^R_{N,j}}{\delta_1} - \frac{2\kappa}{z_{N+1} - z_{N-1}}, \qquad A_{2N,2N} = -\sum_i^N \frac{h^R_{i,N}}{\delta_{2N}} - \frac{2\kappa}{z_{2N+2} - z_{2N}}, \tag{4.35}$$

$$A_{N,N-1} = \frac{2\kappa}{z_{N+1} - z_{N-1}}, \qquad A_{2N,2N-1} = \frac{2\kappa}{z_{2N+2} - z_{2N}}, \tag{4.36}$$

$$A_{k,k} = -\sum_j^N \frac{h^R_{k,j}}{\delta_k} - 2\kappa \frac{z_{k+2} + z_{k+1} - z_k - z_{k-1}}{(z_{k+1} - z_{k-1})(z_{k+2} - z_k)(z_{k+1} - z_k)}, \quad \text{for } 2 \le k \le N-1, \tag{4.37}$$

$$A_{k,k} = -\sum_i^N \frac{h^R_{i,k-N}}{\delta_k} - 2\kappa \frac{z_{k+3} + z_{k+2} - z_{k+1} - z_k}{(z_{k+2} - z_k)(z_{k+3} - z_{k+1})(z_{k+2} - z_{k+1})}, \quad \text{for } N+2 \le k \le 2N-1, \tag{4.38}$$

$$A_{k,k+1} = \frac{2\kappa}{(z_{k+2} - z_k)(z_{k+1} - z_k)}, \quad \text{for } 2 \le k \le N-1, \tag{4.39}$$

$$A_{k,k+1} = \frac{2\kappa}{(z_{k+3} - z_{k+1})(z_{k+2} - z_{k+1})}, \quad \text{for } N+2 \le k \le 2N-1, \tag{4.40}$$

$$A_{k,k-1} = \frac{2\kappa}{(z_{k+1} - z_{k-1})(z_{k+1} - z_k)}, \quad \text{for } 2 \le k \le N-1, \tag{4.41}$$

$$A_{k,k-1} = \frac{2\kappa}{(z_{k+2} - z_k)(z_{k+2} - z_{k+1})}, \quad \text{for } N+2 \le k \le 2N-1, \tag{4.42}$$

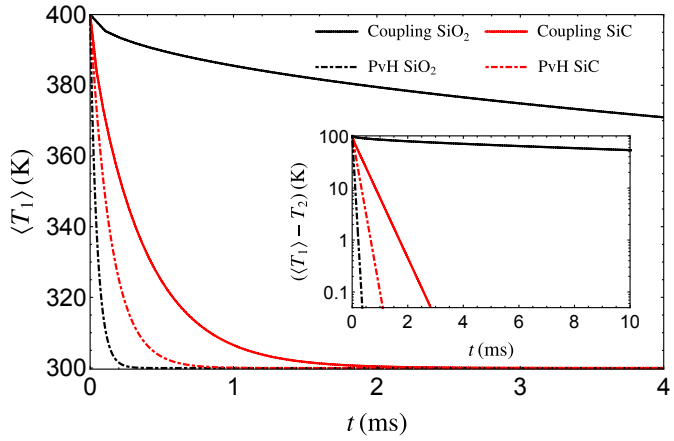

Figure 4.7: Comparison between the time evolution of the average temperature in the left slab and the time evolution of this temperature for a purely radiative (PvH) process. The black (red) solid curve represents the SiO_2 (SiC) coupled case, the black (red) dashed curve the PvH case. The parameters are $T_2 = 300\,\mathrm{K}$, $\Delta T = 100\,\mathrm{K}$ and $d = 1\,\mathrm{nm}$.

$$A_{k,k'} = \frac{h^R_{k,k'-N}}{\delta_k}, \qquad \text{for } 1 \leq k \leq N \text{ and } N+1 \leq k' \leq 2N, \tag{4.43}$$

$$A_{k,k'} = \frac{h^R_{k',k-N}}{\delta_k}, \qquad \text{for } N+1 \leq k \leq 2N \text{ and } 1 \leq k' \leq N. \tag{4.44}$$

With the aim of verifying the surface approximation, in Fig. 4.6 we show the comparison between the average temperature, obtained from the analytical method and using the exact numerical approach in the case of SiC and SiO_2, performing the numerical simulation and the analytical calculation with the following parameters: $\rho_{\mathrm{SiC}} = 3200\,\mathrm{kg{\cdot}m^{-3}}$, $C_{p,\mathrm{SiC}} = 600\,\mathrm{J{\cdot}kg^{-1}{\cdot}K^{-1}}$ while, for SiO_2, $\rho_{\mathrm{SiO_2}} = 2650\,\mathrm{kg{\cdot}m^{-3}}$, $C_{p,\mathrm{SiO_2}} = 680\,\mathrm{J{\cdot}kg^{-1}{\cdot}K^{-1}}$. For both materials, the approximation works pretty well confirming that the radiative heat exchange can be seen as a surfacic phenomenon for these choices materials. It is worth noticing also that after $\sim 2\,\mathrm{ms}$ the first term of the series of the analytical solution becomes dominant and describes alone quite well the temporal evolution. In the following we make a detailed comparison between the relaxation process in the framework of the PvH theory and and the case in which the conduction-radiation coupling is taken into account.

4.4 Relaxation dynamics in the presence of coupling: comparison with a purely radiative process

In Fig. 4.7 we compare the temporal evolution of the average temperature $\langle T_1 \rangle$ for the left slab obtained through the numerical method to the PvH evolution, both for SiC

and for SiO_2 samples [52]. It can be noticed that the difference between the temperatures in a relaxation mechanism driven by a purely radiative (PvH) process and the situation where conduction and radiation are coupled, is more pronounced for two interacting SiO_2 slabs compared to SiC slabs. As anticipated previously, this is due to the fact that the thermal conductivities of SiC and SiO_2 samples are strongly different. The relatively small conductivity of SiO_2 leads to a strong deviation from the PvH predictions. Moreover, as shown in the inset of Fig. 4.7, we notice that the time evolution of $\langle T_1 \rangle - T_2$ follows an exponential behavior. However, the characteristic relaxation time in the presence of coupling is significantly larger than for a purely radiative (PvH) relaxation. Unlike SiC, for SiO_2 samples the temperature evolution (black solid curve) does not follow an exponential decay at the beginning of relaxation process. Nevertheless, after $\sim 2\,\text{ms}$ the curve clearly becomes straight. the mathematical explanation for this behavior can be given considering the analytical model introduced in Sec. 4.3. Actually, after this preliminary time interval, the first term in the series (4.17) becomes dominant with respect to all the others and then the temporal evolution follows an exponential behavior. This is true of course also for the SiC case, but the first term becomes so quickly dominant that we are not able to see at the millisecond scale a deviation from the exponential decay. As shown in the inset of Fig. 4.7, the relaxation dynamics is more than one order of magnitude slower in the presence of coupling. In conclusion, it turns out that the coupling always acts as a thermal inertial mechanism.

Temperature profiles and $\Delta T_{\max}$

In Fig. 4.8 (a)-(b) we show the temperatures profiles for the left and the right slabs, respectively, for the case of SiC at different moments. As we can see, a non-negligible temperature profile appears through the slabs because of the diffusion process. In Fig. 4.8 (a) we also show for comparison the value of T_{PvH} in the left slab at the same moment (the temperature profiles in the right slab are not represented since they remain constant at T_2). In Fig. 4.8 (c)-(d) we show the same curves for the SiO_2 samples. It can be noticed that, also for this material a strong temperature profile is established within each slab. Unlike SiC, in this case we do not represent the temperature $T_{1,\text{PvH}}$ for the same instants since the decay of the temperature is dramatically faster in this case without coupling. Indeed, in the absence of coupling the characteristic decay time would be $\tau_{\text{PvH}} \simeq 0.05\,\text{ms}$. On the contrary, in the presence of coupling and taking $x_1 = \pi/4$ (see Fig. 4.3) as an approximation of the first solution of the transcendental Eq. (4.12), we obtain a decay time $\tau_1 \simeq 24\,\text{ms}$, 500 times larger than τ_{PvH}.

It is worth noticing that the temperature profiles of the second slab, both in the SiC and in the SiO_2 cases evolve in a non-monotonic way. Indeed, at the beginning of the relaxation process the second slab at temperature $T_2 = 300\,\text{K}$ receives heat from the first, which is hotter. Then, after some time, since the first slab loses energy and

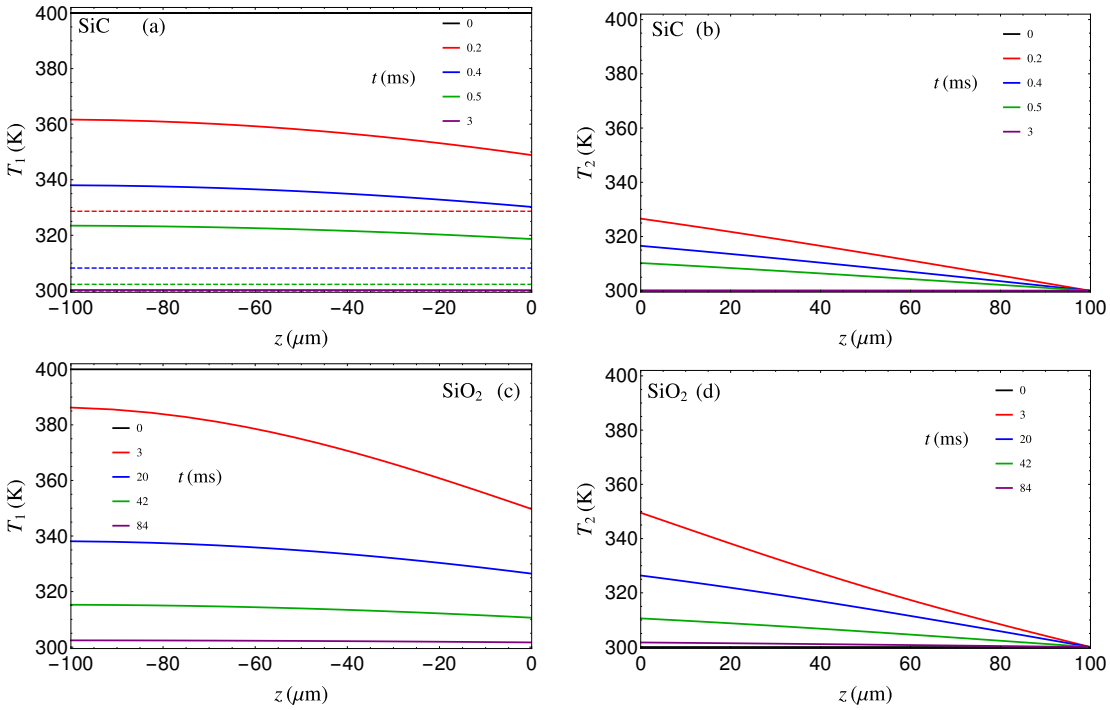

Figure 4.8: **(a)** Temperature profile of the first slab for the SiC case for several instants. The dashed lines correspond to the temperature in the PvH approximation. **(b)** Temperature profile of the second slab for the SiC case for several instants. **(c)** Temperature profile of the first slab for the SiO_2 case for several instants. **(d)** Temperature profile of the second slab for the SiO_2 case for several instants.

becomes colder, the second slab start to cool down toward the equilibrium temperature T_2.

In order to quantify the difference between the two relaxation processes, we introduce the quantity

$$\Delta T_{\text{max}} = \max[\langle T \rangle(t) - T_{\text{PvH}}(t)], \tag{4.45}$$

which allows to quantify the deviation of temperature profiles in the presence of coupling with the one we get in the case of a purely radiative thermalization process. Since at the initial time and at the end of relaxation process the temperature profiles are identical, $\Delta T_{\text{max}}(0) = \Delta T_{\text{max}}(t \to \infty) = 0$. In Fig. 4.9(a)-(b) we represent ΔT_{max} in the fist slab for both SiC and SiO_2 samples as a function of the distance d between the two slabs for several thicknesses L. As expected, the discrepancy between the coupling and the PvH case is less remarkable when the distance is larger, no matter the thickness. This is due to the d^{-2} dependence of the near-field radiative heat flux. It is worth noticing that for SiO_2 samples we explored a range of distances larger with respect to the SiC case: indeed, for the SiO_2 case, we are able to notice a significant discrepancy between the

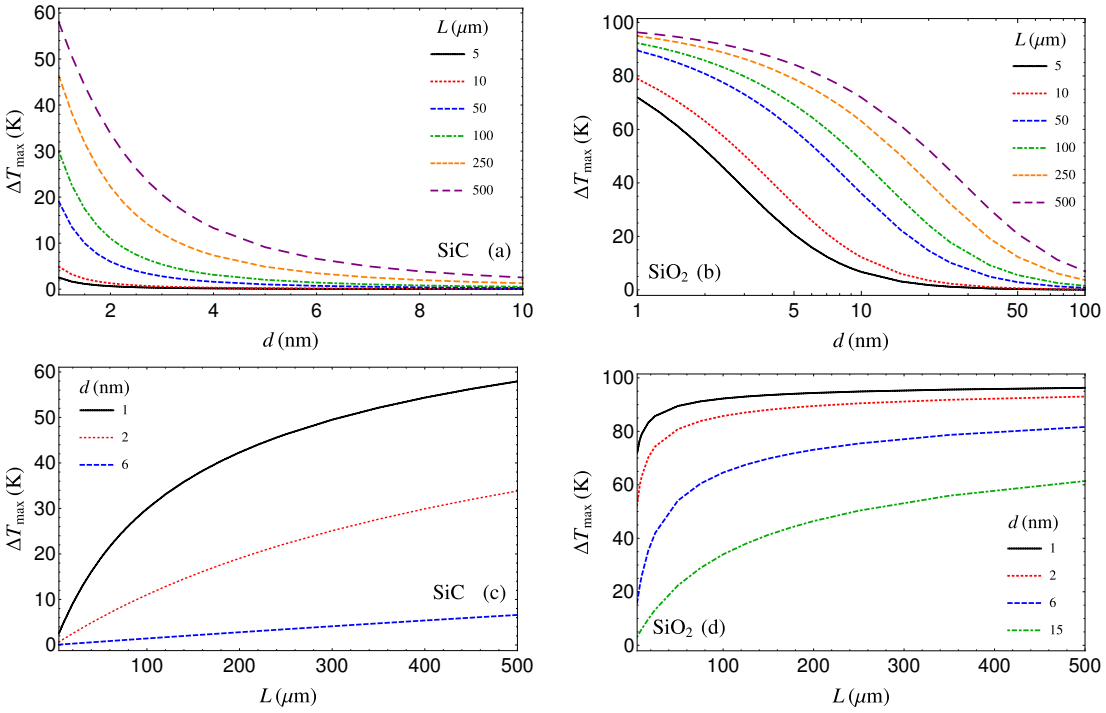

Figure 4.9: **(a)** Maximum temperature difference between the average temperature in the coupling case and the PvH case, as a function of the separation distance between the two SiC slabs for several thicknesses. **(b)** Same as (a) for two SiO_2 slabs. **(c)** Maximum temperature difference between the average temperature in the coupling case and the PvH case, as a function of the separation distance between the two SiC slabs. **(d)** Same as (c) for two SiO_2 slabs.

PvH and the coupling case for $L = 500\,\mu$m even for distances of the order of $100\,$nm whereas for SiC samples we have almost the same $\Delta T_{\rm max}$ for $d \simeq 10\,$nm. This is due not only to the fact that, for the same temperature gradient and distance, the radiative heat flux between the slabs is stronger for SiO_2 with respect to SiC, but above all to a lower efficiency of the conduction for glass compared to SiC ($\kappa_{\rm SiO_2} \approx 0.01\kappa_{\rm SiC}$).

We now investigate the variation of $\Delta T_{\rm max}$ as a function of the thicknesses. In Fig. 4.9(c)-(d) we show its behavior for several separation distances for SiC and SiO_2. Clearly, an increase of the thickness is related to an increase of $\Delta T_{\rm max}$ and then also of the relaxation time of the system. It is important to stress that $\Delta T_{\rm max}$ cannot diverge, and that its asymptotic value is ΔT, that in our specific configuration is $100\,$K. In order to obtain a $\Delta T_{\rm max} \simeq \Delta T$ for example for $d = 1\,$nm we would need a sample with $L \approx 1\,$mm and $L \approx 500\,\mu$m for SiC and SiO_2, respectively.

Material	$h^{\mathrm{el}}\,(10^6\,\mathrm{W}\cdot\mathrm{m}^{-2}\cdot\mathrm{K}^{-1})$	$\kappa(\mathrm{W}\cdot\mathrm{m}^{-1}\cdot\mathrm{K}^{-1})$	$h^{\mathrm{el}}L/\kappa$
Au ($d\sim$0.5 nm)	6.4	310	2.1
Au ($d\sim$0.2 nm)	$9.5{\cdot}10^2$	310	306.5
Au ($d\sim$0.1 nm)	$2.7{\cdot}10^3$	310	871

Table 4.2: Radiative conductance, thermal conductivity and their ratio $h^{\mathrm{el}}L/\kappa$ for Gold at different distances. The parameters chosen are $L = 100\,\mu$m and $T = 120\,$K.

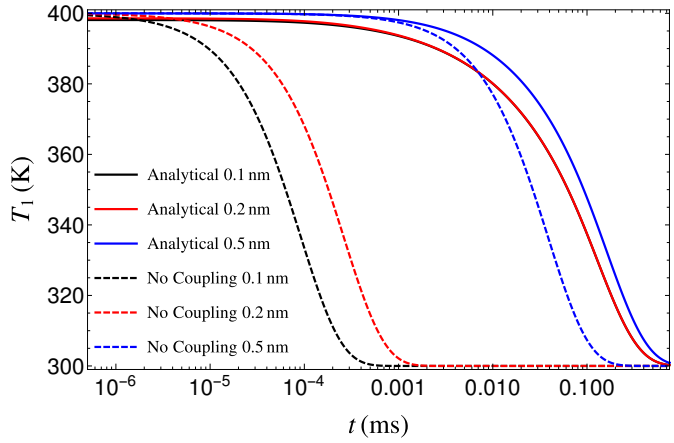

Figure 4.10: Comparison between the time evolution of the average temperature in the left slab in the presence of coupling between heat transport by electron tunneling and conduction inside the slab and the time evolution of this temperature for process without coupling for gold. The black (red, blue) solid curve represents the gold case for $d = 0.1\,$nm ($d = 0.2\,$nm, $d = 0.5\,$nm) coupled case, the black (red, blue) dashed curve the case without coupling. The parameters are $T_2 = 120\,$K and $\Delta T = 160\,$K.

4.5 Conduction-radiation coupling between metals in the extreme near field

Until now, we studied the relaxation process of polar materials interacting in near-field regime. In this section we discuss the case of metals interacting in the extreme near-field regime. Close to the contact (i.e. at subnanometric distance) heat is transmitted mainly by electron tunneling [110]. Although the near-field radiative heat transfer still exists at these separation distances, as shown in [110] this channel of heat transfer is negligible with respect to the electronic channel. The tunneling of electrons can be easily calculated using a simple approximation based on rectangular potential barrier. Following Ref. [111] the potential takes the form $V(d) = V_{\mathrm{ev}}(d) + E_F$, E_F being the Fermi energy level of the metal, and $V_{\mathrm{ev}}(d) = V_0 \ln(1 + d/1\text{Å})$ where V_0 depends on

the metal we consider [112]. It is worth noticing that the barrier becomes higher as the distance d increases, as expected since the larger is the gap the weaker is the electron tunneling. The transmission probability of $\mathcal{T}(E_z, d)$ through this bar reads [113]

$$\mathcal{T}(E_z, d) = \frac{4E_z(E_z - V)}{4E_z(E_z - V) + V^2 \sin^2[k_{2z}(E_z, V)d]} \tag{4.46}$$

where $E_z = \frac{1}{2}m_e v_z^2$ is the kinetic energy due to the motion of electrons along the direction perpendicular to the slabs, $k_{2z}(E_z, V) = \sqrt{2m_e(E_z - V)}/\hbar$ is the normal component of the wavevector inside the vacuum gap and m_e is the electron mass. We stress that the transmission coefficient depends on the size of the vacuum gap d and on the height of the potential barrier V. Summing over all energies E_z direction normal to the surface, the net electronic heat flux reads [111]

$$\Phi^{\text{el}}(T_1, T_2, d) = \int_0^\infty dE_z E_z [N_1(E_z, T_1) - N_2(E_z, T_2)]\mathcal{T}(E_z, d), \tag{4.47}$$

where

$$N_i(E_z, T_i) = \frac{m_e k_B T_i}{2\pi^2\hbar^3} \ln\left[1 + \exp\Big(-\frac{E_z - E_F}{k_B T_i}\Big)\right] \quad \text{with} \quad i = 1, 2, \tag{4.48}$$

indicates the number of electrons with energy between E_z and $E_z + dE_z$ across a unit area per unit time. By calculating the heat flux using this formalism and getting the correspondent thermal conductance h^{el} which reads

$$h^{\text{el}}(T, d) = \lim_{\Delta T \to 0} \left| \frac{\Phi^{\text{el}}(T + \Delta T, T, d)}{\Delta T} \right| = \int_0^\infty dE_z E_z \frac{\partial N(E_z, T)}{\partial T} \mathcal{T}(E_z, d), \tag{4.49}$$

we study as for the other materials the ratio $h^{\text{el}}L/\kappa$ for three subnanometric values of distances, $d = 0.1\,\text{nm}$, $d = 0.2\,\text{nm}$ and $d = 0.5\,\text{nm}$. We perform this simulation in the case of gold, choosing, in agreement with [110], the parameters $T_2 = 120\,\text{K}$ and $\Delta T = 160\,\text{K}$, and taking $E_F = 5.53\,\text{eV}$ and $V_0 = 1.25\,\text{eV}$. The results are summarized in Tab. 4.2. Comparing these values to the ones obtained for SiC, ZnS and SiO_2 in Tab. 4.1, it can be deduced that the comparison between the temporal evolution of the temperature using the analytical model and the scenario ignoring coupling (the analogous of PvH regime for electrons) should be equally or more interesting. In Fig. 4.10 we compare in the gold case the temperature evolution using the analytical method developed in Sec. 4.3 to the one obtained without coupling. The first thing to notice is that the time-scale is much smaller with respect to the polar materials cases (at least a difference of one order of magnitude): this is due above all to a larger thermal conductance and density for gold ($\rho_{\text{Au}} = 19300\,\text{kg}\cdot\text{m}^{-3}$, $C_{p,\text{Au}} = 128\,\text{J}\cdot\text{kg}^{-1}\cdot\text{K}^{-1}$). Concerning the comparison between the cases with or without coupling, as expected, the difference in

relaxation time is modest for $d = 0.5\,\text{nm}$ while it is strongly remarkable for $d = 0.1\,\text{nm}$ and $d = 0.2\,\text{nm}$ ($\tau_1/\tau_{\text{nc}} \sim 1415.7$ in both cases), τ_1 being larger than τ_{nc} of around three orders of magnitude. Indeed, the analytical curves for these distances and then the temporal evolution in the coupling case are almost indistinguishable since the solutions for x_n of Eq. (4.12) are really close to asymptotic values as in the case of SiO_2.

4.6 Conclusions

In this chapter we studied the relaxation dynamics of a system of two micron-sized slabs in the presence of conduction-radiation coupling, and we compared our results to the case without coupling, in which the establishment of a non-uniform temperature profile within each slab is prevented (perfect heat-conductor approximation). First we considered the radiative heat transfer as a purely surface phenomenon and we have performed an analytical description of heat transfer between two slabs of polar material. This preliminary study has revealed that the conduction-radiation coupling slows down the thermal relaxation of slabs. Then we considered the general case where the radiative energy emitted by each slab is dissipated in the heart of the other slab so that a non-uniform temperature profile can be established in both slabs. The numerical resolution of relaxation process in this case showed a good agreement with the analytical model, above all at the first instants of relaxation process, demonstrating in this time interval the surfacic nature of radiative heat exchanges. Moreover, it confirmed that the conduction-radiation coupling slows down the thermalization of slabs in near-field regime. The relaxation time can be more than one order of magnitude larger than the relaxation time predicted by the PvH theory.

These results show that it is necessary to take into account the role of conduction, since it strongly impacts the evolution process. This is true both in scenarios including very common polar materials for near-field heat transfer studies, such as SiC and SiO_2, and for metals for subnanometric distances where electrons are mainly at the origin of heat flux. A further step in the study of conductive-radiation coupling could be to extend this analysis to the case of materials in which the approximation of surfacic radiative flux is no longer satisfied, in order to understand if also in this situation the cooling process can be affected by taking into account the conduction process.

Conclusions

In this thesis we faced the problem of the coupling of radiative heat transfer in near-field regime with other heat-transfer mechanisms, such as conduction, and we studied the dynamics of mechanical oscillators driven by radiative heat transfer in the near-fled regime. We showed that these couplings are at the origin of non-trivial physical effects, such as a strong reduction of flux exchanged between two solids in the crossover regime between conduction and radiation, or a thermomechanical bistable behavior in oscillators based on phase-change materials.

In Chap. 1 we reminded the main results predicted by fluctuational-electrodynamics theory to describe the radiative heat exchange between two bodies. Next, we gave the existence conditions of surface waves for planar surfaces. Finally, we described the main features of radiative heat transfer between polar materials, metals and phase-change materials, such as Vanadium Dioxide (VO_2), a material which undergoes a first-order transition, having dielectric properties for temperatures lower than its critical temperature and metallic ones beyond this critical value.

In Chap. 2 we studied the dynamics of a thermomechanical oscillator made of a phase-change bimaterial cantilever, in order to exploit its features to perform thermal information treatment. To this aim, we considered a micrometric beam, with an upper layer of VO_2 and a bottom layer of SiO_2, exchanging heat radiatively in near field with a silica substrate and in far field with an external bath. We addressed the problem of the coupling between the conduction within the beam, the near-field radiative heat exchange between the substrate and the cantilever, and finally its mechanical oscillations due to the mismatch between the thermal expansion coefficients of the two layers. We highlighted the presence of two equilibrium profiles both for the displacement and the temperature of the beam, demonstrating so the bistability of thermomechanical oscillators. Investigating the existence conditions of this bistability as a function of the different geometrical parameters, we identified the optimal parameters to observe significantly different equilibrium solutions. We finally exploited this peculiar behavior to design either a thermal memory or a thermal NOT logic gate. Although preliminary, this study should pave the way to more general investigations of coupled oscillators driven by near-field interactions. Many problems remain to be explored. First the thermal preparation of oscillators, playing a fundamental role in the dynamical evolution of

the system should be investigated in more details. Moreover, the potential of multiple coupled oscillators in order to perform more complex logical operations would be an important further step for the thermal information treatment.

In Chap. 3 we considered the fundamental problem of the validity of the standard Polder and Van Hove (PvH) theory to describe radiative heat exchanges in extreme near-field regime where the transition to heat conduction should take place. We investigated the transfer between two planar materials by taking into account the heat transfer mediated by conduction inside the interacting samples. In the standard PvH theory, these two bodies are assumed to be perfectly conductive, implying that the temperature within each sample is uniform and equal to the one of the possible thermostats they are in contact with. In the theory we introduced in this work, the heat transport within each solid is studied with the Boltzmann transport equation for phonons, so that all regimes of transport from the ballistic regime (solids smaller than the mean free path of phonons) to the diffusive regime (thick solids with respect to phonon mean free path) can be considered in the conduction-radiation coupling mechanism. Studying the temperature profiles within each slab and the corresponding radiative heat flux between the two in the extreme-near field regime, we showed that a non-negligible temperature variation exists only in the quasi-diffusive or diffusive heat-transport regime cases. This implies a strong deviation with respect to the PvH theory predictions. We showed a relative error between the heat flux calculated by means of the PvH theory and the exact flux which can reach values of the order of 1000% for the configuration of two slabs of 500 μm at 1 nm of distance. We also demonstrated that the near-field heat transfer between two solids is essentially a surfacic phenomenon. This allowed us to anticipate a simplified approach to deal with heat exchanges at subwavelength scale. From an experimental point of view the study of the conduction-radiation coupling in the case of non-planar geometries would be an interesting prospect since it should allow to evaluate the importance of this effect in experimental setups like microscope probes. Finally, a reinterpretation of some experimental results could be made to take into account the conduction-radiation coupling.

In Chap. 4 we addressed the problem of the dynamical evolution of a system of two slabs, one of which is in contact with a thermostat, separated by a vacuum gap in the extreme near-field regime. First, we studied the case in which the slabs are made of SiC or SiO_2 separated by a vacuum gap in the nanometer range and finally considered the relaxation of metallic (Au) samples mediated by electron tunneling at subnanometric distances. Once again, we compared our results to the ones obtained through the simplified theoretical framework ignoring conduction, both through an approximate analytical approach considering the heat exchange through the vacuum gap as a purely surfacic phenomenon and by means of numerical simulations. We demonstrated that, counterintuitively, the presence of conduction within the samples always causes a strong slowdown in the temporal evolution of the temperature profile. The associated relax-

ation time reaches values up to three orders of magnitude larger with respect to its no-coupling counterpart. A further step in the study of conduction-radiation coupling could be to extend this analysis to the case of materials in which the local optical response is no longer satisfied, and investigate how non-local effects affect the cooling process. Finally, a full ab-initio treatment of heat exchanges could be employed to encompass all coupling mechanisms at nanometric and subnanometric scale.

Bibliography

[1] D. Polder and M. Van Hove, *Theory of Radiative Heat Transfer between Closely Spaced Bodies*, Phys. Rev. B **4**, 3303 (1971).

[2] S. M. Rytov, Y. A. Kravtsov, and V. I. Tatarskii, *Principles of Statistical Radiophysics 3: Elements of Random Fields* (Springer-Verlag, Berlin, 1989).

[3] K. Joulain, J.-P. Mulet, F. Marquier, R. Carminati, and J.-J. Greffet, *Surface electromagnetic waves thermally excited: Radiative heat transfer, coherence properties and Casimir forces revisited in the near field*, Surf. Sci. Rep. **57**, 59 (2005).

[4] S.-A. Biehs, M. Tschikin, and P. Ben-Abdallah, *Hyperbolic Metamaterials as an Analog of a Blackbody in the Near Field*, Phys. Rev. Lett. **109**, 104301 (2012).

[5] A. Kittel, W. Müller-Hirsch, J. Parisi, S.-A. Biehs, D. Reddig, and M. Holthaus, *Near-Field Heat Transfer in a Scanning Thermal Microscope*, Phys. Rev. Lett. **95**, 224301 (2005).

[6] L. Hu, A. Narayanaswamy, X. Chen, and G. Chen, *Near-field thermal radiation between two closely spaced glass plates exceeding Planck's blackbody radiation law*, Appl. Phys. Lett. **92**, 133106 (2008).

[7] A. Narayanaswamy, S. Shen, and G. Chen, *Near-field radiative heat transfer between a sphere and a substrate*, Phys. Rev. B **78**, 115303 (2008).

[8] E. Rousseau, A. Siria, G. Jourdan, S. Volz, F. Comin, J. Chevrier, and J.-J. Greffet, *Radiative heat transfer at the nanoscale*, Nat. Photonics **3**, 514 (2009).

[9] S. Shen, A. Narayanaswamy, and G. Chen, *Surface Phonon Polaritons Mediated Energy Transfer between Nanoscale Gaps*, Nano Lett. **9**, 2909 (2009).

[10] R. S. Ottens, V. Quetschke, S. Wise, A. A. Alemi, R. Lundock, G. Mueller, D. H. Reitze, D. B. Tanner, and B. F. Whiting, *Near-Field Radiative Heat Transfer between Macroscopic Planar Surfaces*, Phys. Rev. Lett. **107**, 014301 (2011).

[11] T. Kralik, P. Hanzelka, M. Zobac, V. Musilova, T. Fort, and M. Horak, *Strong Near-Field Enhancement of Radiative Heat Transfer between Metallic Surfaces*, Phys. Rev. Lett. **109**, 224302 (2012).

[12] B. Guha, C. Otey, C. B. Poitras, S. Fan, and M. Lipson, *Near-Field Radiative Cooling of Nanostructures*, Nano Lett. **12**, 4546 (2012).

[13] S. Shen, A. Mavrokefalos, P. Sambegoro, and G. Chen, *Nanoscale thermal radiation between two gold surfaces*, Appl. Phys. Lett. **100**, 233114 (2012).

[14] P. J. van Zwol, L. Ranno, and J. Chevrier, *Tuning Near Field Radiative Heat Flux through Surface Excitations with a Metal Insulator Transition*, Phys. Rev. Lett. **108**, 234301 (2012).

[15] P. J. van Zwol, S. Thiele, C. Berger, W. A. de Heer, and J. Chevrier, *Nanoscale Radiative Heat Flow due to Surface Plasmons in Graphene and Doped Silicon*, Phys. Rev. Lett. **109**, 264301 (2012).

[16] J. Shi, P. Li, B. Liu, and S. Shen, *Tuning near field radiation by doped silicon*, Appl. Phys. Lett. **102**, 183114 (2013).

[17] L. Worbes, D. Hellmann, and A. Kittel, *Enhanced Near-Field Heat Flow of a Monolayer Dielectric Island*, Phys. Rev. Lett. **110**, 134302 (2013).

[18] R. St-Gelais, B. Guha, L. Zhu, S. Fan, and M. Lipson, *Demonstration of Strong Near-Field Radiative Heat Transfer between Integrated Nanostructures*, Nano Lett. **14**, 6971 (2014).

[19] M. P. Bernardi, O. Dupré, E. Blandre, P.-O. Chapuis, R. Vaillon, and M. Francoeur, *Impacts of propagating, frustrated and surface modes on radiative, electrical and thermal losses in nanoscale-gap thermophotovoltaic power generators*, Sci. Rep. **5**, 11626 (2015).

[20] B. Song, Y. Ganjeh, S. Sadat, D. Thompson, A. Fiorino, V. Fernández-Hurtado, J. Feist, F. J. Garcia-Vidal, J. C. Cuevas, P. Reddy, and E. Meyhofer, *Enhancement of near-field radiative heat transfer using polar dielectric thin films*, Nat. Nanotechnol. **10**, 253 (2015).

[21] K. Ito, A. Miura, H. Iizuka, and H. Toshiyoshi, *Parallel-plate submicron gap formed by micromachined low-density pillars for near-field radiative heat transfer*, Appl. Phys. Lett. **106**, 083504 (2015).

[22] M. Lim, S. S. Lee, and B. J. Lee, *Near-field thermal radiation between doped silicon plates at nanoscale gaps*, Phys. Rev. B **91**, 195136 (2015).

[23] K. Kim, B. Song, V. Fernández-Hurtado, W. Lee, W. Jeong, L. Cui, D. Thompson, J. Feist, M. T. H. Reid, F. J. García-Vidal, J. C. Cuevas, E. Meyhofer, and P. Reddy, *Radiative heat transfer in the extreme near field*, Nature **528**, 387 (2015).

[24] B. Song, D. Thompson, A. Fiorino, Y. Ganjeh, P. Reddy, and E. Meyhofer, *Radiative heat conductances between dielectric and metallic parallel plates with nanoscale gaps*, Nat. Nanotechnol. **11**, 509 (2016).

[25] R. St-Gelais, L. Zhu, S. Fan, and M. Lipson, *Near-field radiative heat transfer between parallel structures in the deep subwavelength regime*, Nat. Nanotechnol. **11**, 515 (2016).

[26] S. Lang, G. Sharma, S. Molesky, P. U. Kränzien, T. Jalas, Z. Jacob, A. Y. Petrov, and M. Eich, *Dynamic measurement of near-field radiative heat transfer*, Sci. Rep. **7**, 13916 (2017).

[27] T. Králík, V. Musilová, T. Fořt, and A. Srnka, *Effect of superconductivity on near-field radiative heat transfer*, Phys. Rev. B **95**, 060503(R) (2017).

[28] K. Ito, K. Nishikawa, A. Miura, H. Toshiyoshi, and H. Iizuka, *Dynamic Modulation of Radiative Heat Transfer beyond the Blackbody Limit*, Nano Lett. **17**, 4347 (2017).

[29] A. Fiorino, D. Thompson, L. Zhu, B. Song, P. Reddy, and E. Meyhofer, *Giant Enhancement in Radiative Heat Transfer in Sub-30 nm Gaps of Plane Parallel Surfaces*, Nano Lett. **18**, 3711 (2018).

[30] A. Fiorino, L. Zhu, D. Thompson, R. Mittapally, P. Reddy, and E. Meyhofer, *Nanogap near-field thermophotovoltaics*, Nature Nanotech. **13**, 806 (2018).

[31] A. Fiorino, D. Thompson, L. Zhu, R. Mittapally, S.-A. Biehs, O. Bezencenet, N. El-Bondry, S. Bansropun, P. Ben-Abdallah, E. Meyhofer, and P. Reddy, *A Thermal Diode Based on Nanoscale Thermal Radiation*, ACS Nano **12**, 5774 (2018).

[32] M. Ghashami, H. Geng, T. Kim, N. Iacopino, S. K. Cho, and K. Park, *Precision Measurement of Phonon-Polaritonic Near-Field Energy Transfer between Macroscale Planar Structures Under Large Thermal Gradients*, Phys. Rev. Lett. **120**, 175901 (2018).

[33] V. Musilová, T. Králík, T. Fořt, and M. Macek, *Strong suppression of near-field radiative heat transfer by superconductivity in NbN*, Phys. Rev. B **99**, 024511 (2019).

[34] J. DeSutter, L. Tang, and M. Francoeur, *A near-field radiative heat transfer device*, Nat. Nanotechnol. **14**, 751 (2019).

[35] H. Salihoglu, W. Nam, L. Traverso, M. Segovia, P. K. Venuthurumilli, W. Liu, Y. Wei, W. Li, and X. Xu, *Near-Field Thermal Radiation between Two Plates with Sub-10 nm Vacuum Separation*, Nano Lett. **20**, 6091 (2020).

[36] K. Kloppstech, N. Könne, S.-A. Biehs, A. W. Rodriguez, L. Worbes, D. Hellmann, and A. Kittel, *Giant heat transfer in the crossover regime between conduction and radiation*, Nat. Commun. **8**, 14465 (2017).

[37] L. Cui, W. Jeong, V. Fernández-Hurtado, J. Feist, F. J. García-Vidal, J. C. Cuevas, E. Meyhofer, and P. Reddy, *Study of radiative heat transfer in Ångström- and nanometre-sized gaps*, Nat. Commun. **8**, 14479 (2017).

[38] B. Song, A. Fiorino, E. Meyhofer, and P. Reddy, *Near-field radiative thermal transport: From theory to experiment*, AIP Adv. **5**, 053503 (2015).

[39] C. R. Otey, W. T. Lau, and S. Fan, *Thermal Rectification through Vacuum*, Phys. Rev. Lett. **104**, 154301 (2010).

[40] E. Moncada-Villa, V. Fernández-Hurtado, F. J. García-Vidal, A. García-Martín, and J. C. Cuevas, *Magnetic field control of near-field radiative heat transfer and the realization of highly tunable hyperbolic thermal emitters*, Phys. Rev. B **92**, 125418 (2015).

[41] K. Chen, P. Santhanam, S. Sandhu, L. Zhu, and S. Fan, *Heat-flux control and solid-state cooling by regulating chemical potential of photons in near-field electromagnetic heat transfer*, Phys. Rev. B **91**, 134301 (2015).

[42] P. Ben-Abdallah and S.-A. Biehs, *Contactless heat flux control with photonic devices*, AIP Adv. **5**, 053502 (2015).

[43] K. Chen, P. Santhanam, and S. Fan, *Near-Field Enhanced Negative Luminescent Refrigeration*, Phys. Rev. Appl. **6**, 024014 (2016).

[44] J. Ordonez-Miranda, K. Joulain, D. De Sousa Meneses, Y. Ezzahri, and J. Drevillon, *Photonic thermal diode based on superconductors*, J. Appl. Phys. **122**, 093105 (2017).

[45] V. Kubytskyi, S.-A. Biehs, and P. Ben-Abdallah, *Radiative Bistability and Thermal Memory*, Phys. Rev. Lett. **113**, 074301 (2014).

[46] P. Ben-Abdallah and S.-A. Biehs, *Towards Boolean operations with thermal photons*, Phys. Rev. B **94**, 241401 (2016).

[47] P. Ben-Abdallah and S.-A. Biehs, *Phase-change radiative thermal diode*, Appl. Phys. Lett. **103**, 191907 (2013).

[48] K. Joulain, Y. Ezzahri, J. Drevillon, B. Rousseau, and D. De Sousa Meneses, *Radiative thermal rectification between SiC and SiO_2*, Opt. Express **23**, A1388 (2015).

[49] R. Messina, W. Jin, and A. W. Rodriguez, *Strongly coupled near-field radiative and conductive heat transfer between planar objects*, Phys. Rev. B **94**, 121410 (2016).

[50] M. Reina, R. Messina, S.-A. Biehs, and P. Ben-Abdallah, *Thermomechanical bistability of phase-transition oscillators driven by near-field heat exchange*, Phys. Rev. B **101**, 041409(R) (2020).

[51] M. Reina, R. Messina, and P. Ben-Abdallah, *Conduction-Radiation Coupling between Two Closely Separated Solids*, Phys. Rev. Lett. **125**, 224302 (2020).

[52] M. Reina, R. Messina, and P. Ben-Abdallah, *Strong slowing down of the thermalization process of solids interacting in extreme near-field regime*, arXiv preprint:2106.15471 (2021).

[53] J.-P. Mulet, K. Joulain, R. Carminati, and J.-J. Greffet, *Enhanced radiative heat transfer at nanometric distances*, Microscale Thermophysical Engineering **6**, 209 (2002).

[54] C.-T. Tai, *Dyadic green functions in electromagnetic theory*, IEEE Press series on electromagnetic waves (IEEE Press, Piscataway, NJ, 1994).

[55] S.-A. Biehs, E. Rousseau, and J.-J. Greffet, *Mesoscopic Description of Radiative Heat Transfer at the Nanoscale*, Phys. Rev. Lett. **105**, 234301 (2010).

[56] P. Ben-Abdallah and K. Joulain, *Fundamental limits for noncontact transfers between two bodies*, Phys. Rev. B **82**, 121419 (2010).

[57] S.-A. Biehs, R. Messina, P. S. Venkataram, A. W. Rodriguez, J. C. Cuevas, and P. Ben-Abdallah, *Near-field Radiative Heat Transfer in Many-Body Systems*, Rev. Mod. Phys. **93**, 025009 (2021).

[58] T. V. Shahbazyan and M. I. Stockman (Editors), *Plasmonics: Theory and Applications*, vol. 15 of *Challenges and Advances in Computational Chemistry and Physics* (Springer Netherlands, Dordrecht, 2013).

[59] W. Eckhardt, *Radiation laws in the vicinity of metallic boundaries*, Zeitschrift für Physik B Condensed Matter **46** (1), 85 (1982).

[60] J. B. Pendry, *Quantum limits to the flow of information and entropy*, J. Phys. A: Math. Gen. **16**, 2161 (1983).

[61] E. D. Palik, *Handbook of optical constants of solids* (Academic Press, Orlando, 1985).

[62] N. Elyes, E. Younès, D. Jérémie, and J. Karl, *Maximal near-field radiative heat transfer between two plates*, Eur. Phys. J. Appl. Phys. **63**, 30902 (2013).

[63] P. J. van Zwol, K. Joulain, P. Ben-Abdallah, and J. Chevrier, *Phonon polaritons enhance near-field thermal transfer across the phase transition of VO_2*, Phys. Rev. B **84**, 161413 (2011).

[64] Y. Yang, S. Basu, and L. Wang, *Radiation-based near-field thermal rectification with phase transition materials*, Appl. Phys. Lett. **103**, 163101 (2013).

[65] P. Ben-Abdallah and S.-A. Biehs, *Near-Field Thermal Transistor*, Phys. Rev. Lett. **112**, 044301 (2014).

[66] F. Menges, M. Dittberner, L. Novotny, D. Passarello, S. S. P. Parkin, M. Spieser, H. Riel, and B. Gotsmann, *Thermal radiative near field transport between vanadium dioxide and silicon oxide across the metal insulator transition*, Appl. Phys. Lett. **108**, 171904 (2016).

[67] A. S. Barker, H. W. Verleur, and H. J. Guggenheim, *Infrared Optical Properties of Vanadium Dioxide Above and Below the Transition Temperature*, Phys. Rev. Lett. **17**, 1286 (1966).

[68] B. Li, L. Wang, and G. Casati, *Negative differential thermal resistance and thermal transistor*, Appl. Phys. Lett. **88**, 143501 (2006).

[69] B. Li, L. Wang, and G. Casati, *Thermal Diode: Rectification of Heat Flux*, Phys. Rev. Lett. **93**, 184301 (2004).

[70] C. W. Chang, D. Okawa, A. Majumdar, and A. Zettl, *Solid-State Thermal Rectifier*, Science **314**, 1121 (2006).

[71] N. Li, R. Jie, L. Wang, G. Zhang, P. Hänggi, and B. Li, *Colloquium: Phononics: Manipulating heat flow with electronic analogs and beyond*, Rev. Mod. Phys. **84**, 1045 (2012).

[72] P. Ben-Abdallah, S.-A. Biehs, and K. Joulain, *Many-Body Radiative Heat Transfer Theory*, Phys. Rev. Lett. **107**, 114301 (2011).

[73] P. Ben-Abdallah and S.-A. Biehs, *Thermotronics: Towards Nanocircuits to Manage Radiative Heat Flux*, Z. Naturforsch. A **72**, 151 (2017).

[74] V. Balachandran, G. Benenti, E. Pereira, G. Casati, and D. Poletti, *Perfect Diode in Quantum Spin Chains*, Phys. Rev. Lett. **120**, 200603 (2018).

[75] B. Viswanath and S. Ramanathan, *Direct in situ observation of structural transition driven actuation in VO_2 utilizing electron transparent cantilevers*, Nanoscale **5**, 7484 (2013).

[76] B. Rajeswaran, L. R. Viannie, K. Rajanna, G. R. Jayanth, and A. M. Umarji, *Phase transition induced micromechanical actuation in VO_2 coated cantilever*, J. Appl. Phys. **124**, 074502 (2018).

[77] R. Cabrera, E. Merced, N. Sepúlveda, and F. E. Fernández, *Dynamics of photothermally driven VO_2-coated microcantilevers*, J. Appl. Phys. **110**, 094510 (2011).

[78] R. Cabrera, E. Merced, and N. Sepulveda, *A micro-electro-mechanical memory based on the structural phase transition of VO_2*, Phys. Status Solidi A **210**, 1704 (2013).

[79] K. Wang, C. Cheng, E. Cardona, J. Guan, K. Liu, and J. Wu, *Performance limits of microactuation with vanadium dioxide as a solid engine*, ACS Nano **7**, 2266 (2013).

[80] P. Ben-Abdallah, H. Benisty, and M. Besbes, *Microsecond switchable thermal antenna*, J. Appl. Phys. **116**, 034306 (2014).

[81] S. A. Dyakov, J. Dai, M. Yan, and M. Qiu, *Near field thermal memory based on radiative phase bistability of VO_2*, J. Phys. D: Appl. Phys. **48**, 305104 (2015).

[82] S. Timoshenko, *Strength of Materials: Advanced Theory and Problems* (CBS Publishers & Distributors, New Delhi, 2002).

[83] W. C. Young, R. G. Budynas, and R. J. Roark, *Roark's formulas for stress and strain* (McGraw-Hill, New York, NY, 2007).

[84] C. Canetta, *Bi–material microcantilever–based thermal sensing techniques*, PhD Thesis, Columbia University (2014).

[85] J. Zhang, Z. Xiang, Y. Liu, and M. Xue, *Stability of Thermally Induced Vibration of a Beam Subjected to Solar Heating*, AIAA Journal **52**, 660 (2014).

[86] B. Derjaguin, *Untersuchungen über die Reibung und Adhäsion, IV*, Kolloid-Zeitschrift **69**, 155 (1934).

[87] J. Kidawa-Kukla, *Thermally induced vibration of a cantilever beam with periodically varying intensity of a heat source*, J. Appl. Comput. Mech. **12**, 59 (2013).

[88] B. R. Dewey and R. Jacquot, *Solution Of Static And Dynamic Beam Bending And Static Buckling Problems Using Finite Differences And Matlab*, in *2001 Annual Conference Proceedings*, p. 6.882.1 (ASEE Conferences, Albuquerque, New Mexico, 2001).

[89] C. M. Pearre and W. R. Hudson, *A Discrete-Element Solution of Plates and Pavement Slabs Using a Variable-Increment-Length Model*, Research Report No. 56-11, University of Texas (1969).

[90] N. Sepúlveda, A. Rúa, R. Cabrera, and F. Fernández, *Young's modulus of VO_2 thin films as a function of temperature including insulator-to-metal transition regime*, Appl. Phys. Lett. **92**, 191913 (2008).

[91] M. M. Qazilbash, M. Brehm, B.-G. Chae, P.-C. Ho, G. O. Andreev, B.-J. Kim, S. J. Yun, A. V. Balatsky, M. B. Maple, F. Keilmann, H.-T. Kim, and D. N. Basov, *Mott transition in VO_2 revealed by infrared spectroscopy and nano-imaging*, Science **318**, 1750 (2007).

[92] W. N. Sharpe, Jr. (Editor), *Springer Handbook of Experimental Solid Mechanics* (Springer, New York, 2008).

[93] E. T. Swartz, *Thermal boundary resistance*, Rev. Mod. Phys. **61**, 605 (1989).

[94] G. Chen, *Nanoscale Energy Transport and Conversion : A Parallel Treatment of Electrons, Molecules, Phonons, and Photons* (Oxford University Press, Oxford, 2005).

[95] Y.-J. Han and P. G. Klemens, *Anharmonic thermal resistivity of dielectric crystals at low temperatures*, Phys. Rev. B **48**, 6033 (1993).

[96] N. Mingo, *Calculation of Si nanowire thermal conductivity using complete phonon dispersion relations*, Phys. Rev. B **68**, 113308 (2003).

[97] J. M. Ziman, *Electrons and Phonons: The Theory of Transport Phenomena in Solids* (Oxford University Press, Oxford, 2001).

[98] M. Prunnila and J. Meltaus, *Acoustic Phonon Tunneling and Heat Transport due to Evanescent Electric Fields*, Phys. Rev. Lett. **105**, 125501 (2010).

[99] J. B. Pendry, K. Sasihithlu, and R. V. Craster, *Phonon-assisted heat transfer between vacuum-separated surfaces*, Phys. Rev. B **94**, 075414 (2016).

[100] A. Alkurdi, C. Adessi, F. Tabatabaei, S. Li, K. Termentzidis, and S. Merabia, *Thermal transport across nanometre gaps: Phonon transmission vs. air conduction*, Int. J. Heat Mass Tran. **158**, 119963 (2020).

[101] M. S. Tomaš, *Green function for multilayers: Light scattering in planar cavities*, Phys. Rev. A **51**, 2545 (1995).

[102] S. A. Ali, *Presented in Partial Fulfillment of the Requirements for the Degree Doctor of Philosophy in the Graduate Schoolof The Ohio State University*, PhD Thesis, The Ohio State University (2017).

[103] M. S. Kushwaha, *The Bond-Bending Force Model (BBFM) for Phonons in beta-SiC*, Phys. Status Solidi B **111**, 337 (1982).

[104] D. Lacroix, K. Joulain, and D. Lemonnier, *Monte Carlo transient phonon transport in silicon and germanium at nanoscales*, Phys. Rev. B **72**, 064305 (2005).

[105] D. Morelli, J. Heremans, C. Beetz, W. S. Woo, G. Harris, and C. Taylor, *Carrier concentration dependence of the thermal conductivity of silicon carbide*, Inst. Phys. Conf. Ser. **137**, 313 (1994).

[106] J. Callaway, *Model for Lattice Thermal Conductivity at Low Temperatures*, Phys. Rev. **113**, 1046 (1959).

[107] M. G. Holland, *Analysis of Lattice Thermal Conductivity*, Phys. Rev. **132**, 2461 (1963).

[108] S. Basu and Z. M. Zhang, *Ultrasmall penetration depth in nanoscale thermal radiation*, Appl. Phys. Lett. **95**, 133104 (2009).

[109] M. Tschikin, S.-A. Biehs, P. Ben-Abdallah, S. Lang, A. Y. Petrov, and M. Eich, *Radiative heat flux predictions in hyperbolic metamaterials*, J. Quant. Spectrosc. Radiat. Transf. **158**, 17 (2015).

[110] R. Messina, S.-A. Biehs, T. Ziehm, A. Kittel, and P. Ben-Abdallah, *Heat transfer between two metals through subnanometric vacuum gaps*, arXiv:1810.02628 (2018).

[111] J. G. Simmons, *Generalized Formula for the Electric Tunnel Effect between Similar Electrodes Separated by a Thin Insulating Film*, J. Appl. Phys. **34**, 1793 (1963).

[112] A. Kiejna, *Potential barrier for the metal-vacuum-metal tunneling electrons*, Ultramicroscopy **42-44**, 231 (1992).

[113] C. Cohen-Tannoudji, J. Dunpont-Roc, and G. Grynberg, *Atom-Photon Interactions: Basic Process and Applications: Basic Processes and Applications* (Wiley-VCH, Weinheim, 1998).

université PARIS-SACLAY
ÉCOLE DOCTORALE
Physique et ingénierie : électrons, photons, sciences du vivant (EOBE)

Titre: Couplage conduction-rayonnement à nano-échelle

Mots clés: équation de Boltzmann, champ proche, électrodynamique fluctuationnelle

Résumé: Deux corps à températures différentes échangent toujours un flux de chaleur grâce aux photons même lorsqu'ils sont séparés par du vide. Ce flux radiatif qui est borné par la loi de Stefan-Boltzmann en champ lointain, peut dépasser cette limite de plusieurs ordres de grandeur en champ proche. De manière surprenante, très peu de travaux ont été consacrés jusqu'à présent à l'étude du couplage du transfert radiatif en champ proche et de la conduction dans un solide. C'est l'objet principal de cette thèse. Dans un premier temps nous étudions l'évolution temporelle d'un oscillateur mécanique à base de matériaux à transition de phase couplé en champ proche avec un substrat et nous démontrons son comportement bistable autour de la température critique des matériaux. Le potentiel de ces systèmes pour le traitement thermique de l'information à échelle microscopique est ensuite discuté. Nous développons ensuite une théorie pour décrire le couplage conducto-radiatif entre des solides de taille arbitraire en régime de champ proche extrême. Nous montrons que le couplage entre la conduction et le rayonnement peut induire une variation spatiale importante de la température dans les solides à des distances de séparation de l'ordre du nanomètre. Enfin nous étudions la relaxation thermique de solides séparés par un gap d'épaisseur nano et sub-nanométrique et montrons qu'à ces distances de séparation le temps de relaxation thermique du système est significativement rallongé.

Title: Conduction-radiation coupling at the nanoscale

Keywords: Boltzmann equation, near field, fluctuational electrodynamics

Abstract: Two bodies at different temperatures experience a photon-mediated heat exchange, even when separated by vacuum. This radiative heat flux, limited by Stefan-Boltzmann's law in the far-field regime can exceed this limit even by orders of magnitude for shorter distances, in the near-field regime. Surprisingly, few works have been devoted so far to the study of coupling mechanism between the near-field radiative heat transfer and the conduction inside a solid. This is the main goal of this thesis. First, we study the time evolution of a mechanical oscillator based on phase-transition materials coupled in the near-field regime with a substrate and we demonstrate its bistable behavior around the critical temperature of materials. The potential of these systems for thermal information processing at microscopic scale is then discussed. Next we develop a theory to describe the conducto-radiative coupling between solids of arbitrary size in extreme near-field regime. We show that the coupling between conduction and radiation can induce a large spatial variation in the temperature profile within the solids at nanometric separation distances. Finally, we study the thermal relaxation of solids separated by a gap of nano and sub-nanometric thickness and show that at these separation distances the thermal relaxation time of the system is significantly lengthened.

Université Paris-Saclay
Espace Technologique / Immeuble Discovery
Route de l'Orme aux Merisiers RD 128 / 91190 Saint-Aubin, France

université PARIS-SACLAY